



Universiteit Gent
Faculteit Ingenieurswetenschappen en Architectuur
Vakgroep Informatietechnologie

Dual Polarization Ring Resonator for Conformational Analysis of Molecular-sized Layers

Ringresonator met tweevoudige polarisatie voor
conformationele analyse van lagen met moleculaire
afmetingen

Jan-Willem Hoste



Proefschrift tot het bekomen van de graad van
Doctor in de Ingenieurswetenschappen:
Fotonica
Academiejaar 2014-2015



Universiteit Gent
Faculteit Ingenieurswetenschappen en Architectuur
Vakgroep Informatietechnologie

Promotoren:

Prof. Dr. Ir. Peter Bienstman

Examencommissie:

Prof. Dr. Ir. L. Taerwe (voorzitter)	Universiteit Gent, Magnel laboratory
Prof. Dr. Ir. P. Bienstman (promotor)	Universiteit Gent, INTEC
Prof. Dr. Ir. B. De Geest	Universiteit Gent, Department of Pharmaceutics
Dr. Ir. K. B. Gylfason	KTH
Prof. Dr. Ir. N. Le Thomas	Universiteit Gent, INTEC
Dr. Ir. F. Strubbe	Universiteit Gent, ELIS

Universiteit Gent
Faculteit Ingenieurswetenschappen en Architectuur

Vakgroep Informatietechnologie
Sint-Pietersnieuwstraat 41, B-9000 Gent, België

Tel.: +32-9-264.33.41

Fax.: +32-9-264.35.93

Dankwoord

BAM! Dat was het dan. Zo rap je erin rolt, spurt je er weer uit.

Het verbaast me telkens hoe ogenschijnlijk kleine beslissingen een kracht hebben die een half decenium later nog voelbaar is. Er zijn van die momenten waarop je snel je gevoel volgt die uiteindelijk even belangrijk blijken te zijn als diegene waar je 6 jaar voor moet studeren. Na mijn diploma ingenieurswetenschappen: fotonica behaald te hebben kon ik beginnen bij Alcatel. Ik twijfelde wat en besloot even bij Roel Baets binnen te springen om te zien of hij me niet naar een buitenlandse universiteit kon sturen om mee te draaien in een onderzoeksgroep voor een jaar. Veel hoop had ik niet, want er waren geen officiële programma's waar ik me voor kon inschrijven. Roels daadkracht was indrukwekkend: voor mijn neus stuurde hij even twee e-mails naar een Duitse en Spaanse collega en hoppa ik mocht beschikken. "Je hoort nog van me!". Een dag later had hij antwoord gekregen van een zekere Thomas Pertsch en ik mocht een jaar naar Jena. Geen Alcatel of Barcelona dus, wel Jena. Jena?

Hiervoor mijn onmeetbare dankbaarheid aan Roel en Thomas om dat zo à l'improviste klaar te spelen. Een schitterende ervaring heb ik daar opgedaan in Jena. Ik ben er volledig geïnteresseerd geraakt in fysica en fotonica. Nu is science echt mijn ding, dat ben ik zeker, en dat ging ik nooit zeker geweten hebben had ik daar mezelf niet gevonden. Ook op sociaal vlak heb ik mezelf leren kennen, en nog een hele hoop anderen ook. Goede vrienden die ik nog jaarlijks zie. Rossa, Mateo, Greg, Kemal, Martin, Ludwig, Nico, Robert, John, ik heb het tegen jullie. Bedankt voor de heerlijke tijden daar en om nog regelmatig naar Gent te komen. Ik ben Oost-Duitsland ook betrekkelijk geïntrigeerd geraakt door elektronische muziek, ondertussen een passie van me.

Het mooiste dat ik aan die tijd heb overgehouden is echter mijn vriendin Nadya. Ze is mijn steun (die me af) en toeverlaat. Goeie bal om naar Delft te komen doctoreren, Nadya. Weldra woon je in België, en spreek je vloeiend West-Vlaams. Dat is toch al een stuk dichterbij Russisch dan het Haagse Hollands, nietwaar?

Als je hier even bij stil staat heb ik zowel mijn lief, mijn job en mijn passie voor

wetenschap en muziek te danken aan dat ommetje via Jena. Dat is toch waanzin? Ik overabstraheer de zaken wel een beetje, maar toch. Als jullie naast ringresonatoren met tweevoudige polarisaties nog iets overhouden aan deze thesis, laat het dan dit zijn. Als je de kans hebt om eens voor langere tijd naar het buitenland te gaan, laat ze niet liggen, bitte. Je gaat een pak rijker terugkomen.

Misschien is een doctoraat wel iets voor mij, besepte ik daar in Thuringia. Ik was een paar weken ver bij INTEC en ik wist het zeker: goed gekozen. Bedankt om mij een kans te geven om die microringen te exciteren met twee orthogonale polarisaties, Peter! Ze zitten daar goed, die polarisaties. Voor de geïnteresseerde lezer, je bent goed op weg, nog een goeie 150 paginas en niemand zal je ooit meer iets wijsmaken over het opmeten van conformationele veranderingen met een microringresonator. Peter, ik ben vaak verrast geweest door je capaciteiten om de zaken het juiste gewicht te geven, dat apprecieer ik. Ik hoop dat we in de toekomst even goed kunnen blijven samenwerken!

Wat een onderzoeksgroep is dit zeg. Intellectueel drijvend. De members van de biomeetings wil ik toch speciaal vermelden, Daan, Sam, Rodica, Christina, Tom, Anabelle en Elewout. Speciale vermelding ook voor Alfonso, altijd klaar om in te vallen voor de biogroep. Die twee uur overleggen over experimenten, theoriën en wie er nog wat tubing overheeft waren de moeite. Also a special thank you to the boys from the big office! We're having big fun and doing good science. And your work ethics kept me going into the late hours as well. Danaë, bedankt om op het juiste moment te vragen wat ik na mijn doctoraat wil doen. Ik wil jou en Bart extra bedanken voor het voorbereidende werk voor ons IWT-IM. Ik ben erg trots dat we die samen binnengehaald hebben. Het zullen spannende tijden zijn de volgende 2 (hopelijk meer) jaar, maar we hebben een goed team. Ik sta alvast te popelen!

De ongelofelijke bende maten wil ik uiteraard ook bedanken. En dan heel specifiek om me twee weken voor indiendatum te helpen verhuizen. In twee uur was het gepiept, ik moest niet van mn bureau opstaan! Jullie zijn helden, jongens! Stuk voor stuk 48-karaats heldenmateriaal, met oog voor het betere leven. Daar kun je wel een crisis of twee mee door.

Ten slotte wil ik ook mijn ouders en familie bedanken voor alle steun! Jullie horen op de eerste regel te staan, maar dat wrong nogal. Tja, het is eigenlijk absurd je ouders en familie te bedanken. Ze hebben alles voor je gedaan en er zou werkelijk niets van je huidige werkelijkheid overblijven zonder je ouders en dan moet je dat proberen weer te geven in een paar zinnen in een dankwoord, zonder teniet te doen aan hun allesomvattendheid? Daar bedank ik voor.

*Gent, september 2015
Jan-Willem Hoste*

Table of Contents

Dankwoord	i
Nederlandstalige samenvatting	xxiii
English summary	xxxiii
1 Introduction	1-1
1.1 Inertia in pharma	1-1
1.2 Proteins' hidden dance	1-2
1.3 Current landscape of conformational tools	1-4
1.3.1 Labelfree sensing	1-5
1.4 Integrated Silicon Photonics	1-9
1.5 Dual Polarization Microring	1-12
1.6 Publications	1-13
1.6.1 Patent applications	1-13
1.6.2 Publications in international journals	1-13
1.6.3 Publications in international conferences	1-13
References	1-15
2 Components of a conformational biosensor	2-1
2.1 Introduction	2-1
2.2 Waveguides and their separation in modes	2-2
2.3 Microring resonator	2-11
2.3.1 Add-drop resonator	2-13
2.3.2 Sensing with a microring resonator	2-16
2.4 Designing a dual polarization microring resonator	2-17
2.4.1 Simultaneous coupling	2-18
2.5 From a microring resonator to a sensing experiment	2-24
2.5.1 Microfluidics	2-26
2.5.2 Measurement setup	2-27
2.5.3 Detection of PSA antigens	2-29
2.6 Obtaining physical characteristics	2-30
References	2-32

3	Analysis framework	3-1
3.1	Introduction	3-1
3.2	Different approaches to extract t and n	3-2
3.3	Solving framework overview	3-5
3.4	Mathematical model	3-7
3.5	Calibration protocol	3-12
3.5.1	Off-line imaging techniques	3-12
3.5.2	In-line self-calibration	3-14
3.6	System performance	3-17
3.6.1	Detection limit	3-17
3.6.1.1	Detection limit of a single polarization microring system	3-18
3.6.1.2	Detection limit of a system with two unknowns	3-19
3.6.2	Thinnest detectable layer	3-22
3.6.3	Paths to improvement	3-23
	References	3-27
4	Dual Polarization Vernier Cascade	4-1
4.1	Introduction	4-1
4.2	Vernier principle	4-2
4.3	Single polarization microring Vernier cascade	4-3
4.4	Exploiting the Vernier cascade in a dual polarization setting	4-6
4.4.1	Thread 1: Leveraging a differential amplification?	4-6
4.4.2	Thread 2: Single ring equivalent noise reduction	4-7
4.5	Dual polarization vernier cascade	4-9
4.5.1	Photonic integrated design	4-9
4.5.2	Experimental and theoretical spectra	4-11
4.5.3	Including an AWG to improve the limit of detection	4-15
4.6	Measurement framework	4-18
4.7	Sensor Performance	4-20
4.7.1	Detection limit of a Vernier cascade	4-20
4.8	Conclusion	4-21
	References	4-23
5	Measuring the conformation of biological molecules	5-1
5.1	Introduction	5-1
5.2	Conformational analysis of BSA molecules	5-2
5.2.1	Capturing the TE and TM shifts	5-2
5.2.2	Retrieving thickness, refractive index and bound mass	5-3
5.2.3	Structural response of the BSA molecules to the pH change	5-5
5.3	DNA experiment	5-8
5.3.1	Hybridization protocol	5-9
5.3.2	Single polarization analysis	5-11
5.3.3	Analysis with a dual polarization microring	5-14
5.4	Conclusion	5-17

References	5-19
6 Analysis of the interface layers of a bilayer system	6-1
6.1 Introduction	6-1
6.2 One layer after another	6-2
6.3 Experimental section	6-4
6.3.1 Properties of the polymer solutions	6-4
6.3.2 Outline of the experiment	6-4
6.4 Results & Discussion	6-6
6.5 Conclusion	6-12
References	6-13
7 Conclusion	7-1
7.1 Perspectives	7-3

List of Figures

- 1 (a) Afbeelding van de SOI-chip met een microfluidische cel uit PDMS, die bovenop de SOI-chip bevestigd werd. (b) Rasterelektronenmicroscopbeeld van een microringresonator met twee toegangsgolfgeleiders. (c) Illustratie van de doorsnede van de microringresonator met de receptormoleculen bovenop het ringoppervlak. (d) Spectrum van de uitgang van de toegangsgolfgeleider die de resonantiedip toont en de verschuiving hiervan onder invloed van een bindingsevent. xxiv
- 2 Sensorgram van een microringresonator waarover een sequentie van biochemische moleculen gestroomd werden. Door PSA-antilichamen aan het oppervlak te binden, kon vervolgens een PSA antigeen met concentratie van 30 ng/ml gedetecteerd worden. xxvi
- 3 Schematisch overzicht van de verschillende aspecten van het oplossingsraamwerk. Het spectrum wordt opgemeten en de golflengteverschuivingen van de TE en de TM mode worden hieruit berekend. Een deel van deze metingen gebruiken we om de golfgeleider in de simulaties te calibreren. Deze simulaties worden vervolgens gebruikt om een theoretisch model op te stellen. Uiteindelijk worden de golflengteverschuivingen aan de hand van dit model omgezet naar de dikte en de brekingsindex van de moleculaire laag. xxvii
- 4 (a) Dikte- en brekingsindexprofiel van een laag bestaande uit geadsorbeerde BSA-moleculen. (b) Evolutie van de conformatie van de BSA-moleculen, terwijl ze adsorberen op het silicium oppervlak onder invloed van een veranderende pH-waarde van de PBS-buffer waarin ze opgelost zijn. xxviii
- 5 (a) Hybridisatie-efficiëntie van een complementaire DNA-streng in functie van de HEG-concentratie. Een verhoging van de efficiëntie met een factor 3 tot 4 is verkregen met voldoende HEG-concentratie. Data opgemeten door Anabelle van Eeghem. (b) Dikteprofiel opgemeten tijdens de binding van een DNA-streng op het oppervlak, gevolgd door de adsorptie van 1 mg/ml HEG-polymeer. xxix

-
- 6 (a) Illustratie van een mogelijke constructie van een microcapsule door middel van de tweelagentechnologie die zich rond een poreus materiaal wikkelt waarin een geneesmiddel bevat zit. De positief en negatief geladen polyelektrische lagen adsorberen beurtelings rond het poreus materiaal om zo de capsule te vormen. (b) Golfengteverschuiving van TE en TM modes gedurende de adsorptie van 5 cycli op het oppervlak van de microring. (c) Gedeponeerde massa en (d) dikte- en brekingsindexprofiel. (e) De toegevoegde massa per cyclus van twee verschillende experiment. xxx
- 7 (a) Elektronenmicroscopiebeeld van een tweevoudigepolarisatie-Verniercascadeontwerp bestaande uit drie microringen. (b) Opgetuuten en gesimuleerd spectrum van poort 3. xxxi
- 8 (a) Picture of the SOI chip with bonded PDMS microfluidic cell on top, connected with tubings. (b) SEM image of a microring resonator with two access waveguides. (c) Illustration of the ring cross section that shows the receptor molecules on top of the ring. (d) Spectrum of the output of the access waveguide, showing the resonance dip and the shift in wavelength due to a binding event. xxxiv
- 9 Sensorgram of a microring resonator where a series of molecular agents were bound to the ring surface. By attaching an antibody to protein specific antigen (PSA), we could detect PSA with a concentration of 30 ng/ml xxxv
- 10 Schematic overview of the different aspects of the solving framework. The spectrum is measured and the peaks of the TE and TM modes are tracked. This feeds into the simulations to calibrate the waveguide profile. These simulations are fit to a theoretical model, derived from waveguide theory. Finally, the measured shifts are solved with this model to obtain the thickness and refractive index profile. xxxvi
- 11 (a) Thickness and refractive index profile of the layer consisting of adsorbed BSA molecules. (b) Evolution of the conformation of the BSA molecules as they adsorb to the silicon surface under influence of a change in pH value of the PBS buffer in which they are suspended. xxxvii
- 12 (a) Hybridization efficiency of the complementary DNA-strand in function of the concentration of the adsorbed HEG polymer. Adsorption of HEG at sufficient concentration shows a 3-4 fold increase in hybridization efficiency. Data obtained by Anabelle van Eeghem. (b) Thickness profile during coupling of the DNA probe to the surface and subsequent adsorption of 1 mg/ml HEG, explaining the increased hybridization efficiency due to a reorientation of the DNA probes. xxxviii

13	(a) Schematic representation of the assembly with LbL technology of a microcapsule loaded with a drug component, by using a porous template. The drug is first inserted into a porous template, after which a bilayer polymer system is wrapped around this template by the alternating coating with a positive polyelectrolyte and a negative polyelectrolyte. (b) Wavelength shifts of TE and TM mode recorded during the adsorption of 5 cycles of the bilayer system. (c) Deposited mass and (d) thickness and refractive index profile. (e) Mass increment per cycle of two different experiments showing an interface and a bulk regime.	xxxix
14	(a) SEM picture of a dual polarization Vernier design consisting of three SOI microrings. (b) Measured spectrum at port 3, and simulated spectrum at port 3	xi
1.1	Illustration of orthosteric and allosteric binding, and the response of a sensor that can track mass as well as thickness. The protein has a primary binding site, indicated by P and an allosteric binding site, indicated by A. When ATP binds in the primary binding site, the protein is activated. In orthosteric binding, the drug ligand inhibits this primary binding site, while in allosteric binding, the drug ligand binds at a secondary binding spot, to render the primary binding spot inaccessible by conformational change. ATP is indicated in blue, while the drugs is indicated in red.	1-3
1.2	SEM image of a microring resonator in the SOI platform.	1-10
1.3	(a) Illustration of the microring with fluidic channel on top as an angled perspective view and (b) as a cross section that shows the receptor molecules on top of the ring. (c) Spectrum of the output of the access waveguide, showing the resonance dip and the shift in wavelength due to a binding event.	1-11
2.1	Illustration of a slab waveguide with a silicon layer as guiding layer. The refractive indices of the cladding layers above and below the guiding layer must be smaller than the refractive index of silicon. The structure is uniform in the y- and z-direction.	2-6
2.2	Illustration of a wire waveguide with rectangular cross section in silicon as guiding layer. The photonic wire rests on a substrate. In this thesis, this wire is in direct contact with the environment, such that the top and side cladding (n_2) is usually air or an aqueous fluid transporting analytes.	2-7
2.3	Caution must be made when transforming $\mathbf{H}(\mathbf{r})$. It transforms as a pseudovector, which means it acquires an extra minus under mirror reflection. The electric field $\mathbf{E}(\mathbf{r})$ is a vector and reflects as expected.	2-9
2.4	(a) Symmetry planes of a rectangular waveguide with equal cladding around the waveguide. (b) The TE and TM modes and their relation to these two symmetries.	2-11

2.5	Plot of the (a) E_x component of the fundamental TM mode and b) the E_y component of the fundamental TE mode in an SOI waveguide with water as top and side cladding. With x and y defined as in Figure 2.4.	2-12
2.6	An add-drop resonator and its parameters.	2-14
2.7	(a) Spectrum at the drop port and the pass port of an add-drop ring resonator with a radius of $20 \mu\text{m}$ showing the repeating filtering behavior. (b) Close-up of a resonance indicating the specific quantities.	2-15
2.8	Sensitivity of the microring resonator to binding of a thin bilayer in water for fundamental quasi-TE mode and fundamental quasi-TM mode, obtained with Fimmwave. The height of the waveguide is fixed at 220 nm and the excitation wavelength is 1550 nm. . . .	2-17
2.9	Effective index of the first six guided modes for a rectangular waveguide with a height of 220 nm and a watery cladding.	2-18
2.10	Effective index of the first three guided modes for a rectangular waveguide with a height of 220 nm and water cladding. The black lines show the slight phase mismatch for a 550 nm ring waveguide and a 290 nm access waveguide.	2-20
2.11	Example of a spectrum exhibiting dual polarization functionality, measured when the SOI chip was submerged in water.	2-22
2.12	Scatter plot of the resonances in the microrings with dimensions as given in Table 2.1 of (a) the TE modes and (b) the TM modes. The only gap which exhibits dual polarization functionality are the ones which are 120 nm wide, independently of the phase matching.	2-23
2.13	(a) SEM image of the microring with two access waveguide. (b) After an ion bombardment, a FIB-SEM image of the cross section of the coupling section is taken, which shows the waveguide dimensions.	2-24
2.14	(a) Bright field microscopic image of a section of the sensing matrix. The microring resonators are organized in four columns such that the microfluidic channel can meander easily from column to column. (b) Close-up of the red square in (a), showing three microring resonators.	2-25
2.15	Picture of the SOI sensing chip with 5 mm high PDMS fluidic cell bonded on top. Tubings are inserted which connect the fluidic channels with the analytes.	2-26

-
- 2.16 (a) Photograph of measurement setup 1 that excites the SOI chip with a fiber. (b) Zoom of the SOI chip stage of this setup that shows the PDMS cell bonded to the SOI chip. The input of the SOI chip is to the right, where the fiber couples light in. On the left-hand side of the SOI chip, the light couples back out vertically according to the red arrow, where it is collected by optics (not on the photograph). (c) This setup can be adjusted to setup 2 by replacing the fiber by a collimator. The alignment camera is in that case no longer necessary 2-28
- 2.17 Spectrum of the sensing ring with a water cladding of as measured by the measurement setup for biochemical experiments. (a) The SOI microring has a rectangular cross section with a width of 520 nm and a height of 220 nm. The optical input section of the sensing ring is excited by means of an optical fiber. (b) The SOI microring has a rectangular cross section with a width of 550 nm and a height of 220 nm and the optical input coupler of the sensor is illuminated by a collimated laser beam. 2-29
- 2.18 Detection experiment of PSA-antigen on an SOI chip on which the PSA-antibodies are immobilized on the microrings. This is done by using an APTES+glutaraldehyde strategy. 2-30
- 3.1 Different techniques on how to obtain the unknown thickness and refractive index out of the measured shifts. The techniques are ordered on a scale based on the relative importance of a theoretical model. 3-2
- 3.2 Schematic overview of the different aspects of the solving framework. The spectrum is measured and the peaks of the TE and TM modes are tracked. This feeds into the simulations to calibrate the waveguide profile. These simulations are fit to a theoretical model, derived from waveguide theory. Finally the measured shifts are solved with this model to obtain the thickness and density profile. 3-5
- 3.3 2D cross section of an SOI wire waveguide as it is solved by Fimmwave. For a given set of parameters W , H and n_b , the waveguide profile is solved and n_{eff} and n_g are obtained for a number of modes. This is repeated for a wide range of possible layers with characteristics (t, n) , which cover the waveguide profile. 3-6
- 3.4 Example of the group index as simulated by Fimmwave for a thickness of the biolayer of 5 nm and various refractive indices. The different curves represent simulations done with an increasing amount of internal modes. This can be considered the resolution of the simulation. It is clear that by increasing the number of modes, the numerical error of the $n=1.5$ point gets damped, but it does not completely disappear. 3-7

-
- 3.5 Waveguide cross section used in the adapted method of Marcatili, presented here to obtain the field profiles in the zones indicated. The zones 2 and 4 indicate the protein layer. 3-8
- 3.6 Simulations of the wavelength shifts for both modes in function of the thickness of the protein layer for various refractive indices of this layer. The fitting of this data to the model results in an R^2 value of 0.9998. 3-10
- 3.7 Visualization of the solving protocol by plotting $f(t, n) = \Delta\lambda_{TE}$ and $f(t, n) = \Delta\lambda_{TM}$, with the shifts corresponding to the shifts obtained for a layer with thickness 10 nm and refractive index 1.45. 3-11
- 3.8 Various techniques to retrieve the width and height of the waveguide profile. All images are taken from the same SOI chip. (a) Focussed ion beam image, tilted perspective after the ions have bombarded the coupling section of microring resonator and (b) zoom on the indicated region. (c) Atomic force microscopy image indicating the height profile of a 2D section of the chip where a waveguide runs with (d) height profile of the two indicated lines. (e) Stylus profilometer profile of a series of adjacent waveguides and (f) zoom on the indicated region. 3-13
- 3.9 Simulated group indices of a rectangular waveguide, showing a high dependency on one of the spatial coordinates for both modes. 3-14
- 3.10 By measuring the FSR of both modes during a water phase prior to the following BSA experiment, the (a) width of the ring waveguide was determined with a mean value of 491.7 nm. (b) The height was calculated to be 210.7 nm. 3-16
- 3.11 (a) Simulation of the wavelength shift of the TE mode in function of the refractive index of a cladding layer with waveguide dimensions of $W = 491$ nm and $H = 210$ nm. The wavelength shift is simulated with respect to a buffer with $n_{buff} = 1.32$. (b) Shift of the TE resonance when switching from water to buffer (PBS in this case), as measured in the BSA experiment. 3-17
- 3.12 Schematic diagram of the calibration and the actual experiment. The calibration measurements are done before the measurements for the actual experiment start. They are used to obtain the simulation parameters. These simulations finally determine the model to solve the experimental measurements to the characteristics of the protein layer. 3-18
- 3.13 Visualization of the limit of detection in thickness and refractive index. The solid red and blue lines represent the curves that intersect in the solution (t, n) . The dotted curves represent these curves as measured under the influence of noise such that the purple area delineates possible solutions in a noisy measurement. The maximum error on t and n obtained from this collection of solutions is defined as the limit of detection on t and n . Mind that the slope of the f and g curves is changed for illustrative purposes. 3-20

-
- 3.14 Simulated spread on solved thickness and refractive index, due to noise on TE and TM wavelength positions. A certain (t,n)-couple is fed into the calibrated model, which gives a $(\Delta\lambda_{TE}, \Delta\lambda_{TM})$ -couple. The (t,n)-couples are indicated by the intersections of the solid vertical and horizontal lines. n_b is the refractive index of water, 1.316. After adding noise on both shifts, sampled from an equidistant 2D space of $[-220 \text{ fm}, 220 \text{ fm}] \times [-220 \text{ fm}, 220 \text{ fm}]$, the noisy shifts are calculated back to (t,n) couples which are all plotted, rendering the spreads. The limits of this sampling space (220 fm) represent the experimentally determined standard deviation on the resonance wavelengths. Different colors and markers represent different clusters. 3-21
- 3.15 Experimentally determined noise as the standard deviation on thickness and density during the last 5 minutes of the polymer experiment in chapter 6. At this point, 5 bilayers were adsorbed to the silicon surface, which had a total thickness of 7.5 nm and a refractive index of 1.45 3-22
- 3.16 (a) Experimentally determined noise as the standard deviation on deposited mass during the last 5 minutes (red dots) of the polymer experiment of chapter 6 while water was streaming over the sensor. At this point, 5 bilayers were adsorbed to the silicon surface, which had a total thickness of 7.5 nm and a refractive index of 1.45. (b) Experimentally determined noise from the same experiment but when only the first layer (PEI layer) had adsorbed to the stack, with a thickness of 1.84 nm and a refractive index of 1.465. The standard deviation is determined on 8 measurement points, during 2 minutes. 3-23
- 3.17 Contour plot in log scale of the relative maximum error on thickness. It can be seen that the “-1”-contour intersects with the $\Delta n = 0.1$ -line for $t = 0.75$. This means that a layer thinner than 0.75 nm can no longer be determined with a relative error smaller than 10 % 3-24
- 3.18 Plot of Equation 3.33 for a planarized waveguide with rectangular cross section with a height of 220 nm 3-25
- 3.19 Limit of detection on determination of t and n for various widths of the waveguide, with a fixed height of 220 nm. 3-26
- 4.1 (a) Illustration of a modern Vernier caliper [?]. (b) Close-up of both measuring scales (not related to (a)), with a second close-up at the top right corner indicating the region where the two scales align [?]. The single scale reads 3.7 cm, while the addition of the second scale improves the measurement resolution such that a size of 3.746 cm is measured 4-2
- 4.2 Traditional Vernier configuration for a single polarization [3] . . . 4-4

4.3	Vernier principle: top row shows the spectra of the individual sensing and reference rings in solid and dashed lines before and after a binding event, while the bottom row shows the corresponding Vernier cascade spectrum. At a time t_2 a differential shift $\Delta\lambda_1$ of the individual rings is amplified to a shift $\Delta\lambda_2$ of the Vernier cascade.	4-5
4.4	Vernier cascade adhering to inequality 4.1 to obtain a comb of peaks with a smoothly varying peak amplitude. The peak amplitudes can be fit to a squared Lorentzian in order to obtain the peak position and hence the shift of the Vernier cascade [3].	4-6
4.5	SEM picture of a dual polarization Vernier design consisting of three SOI microrings. The point annotated by "A" indicates the pass port of the TE ring.	4-10
4.6	Simulated and measured spectra of the output ports of the Vernier cascade, with the port numbers shown on figure 4.5. (a) Measured spectrum of port 1, (b) simulated spectrum of port 1. (c) Measured spectrum of port 3, (d) simulated spectrum of port 3. (e) Measured spectrum of port 7, (f) simulated spectrum of port 7. The measured spectra are compensated for the transmission spectrum of the grating coupler.	4-12
4.7	Simulated Vernier spectrum at point A, indicated in Figure 4.5, obtained by transmission through the drop port of the reference ring and consequently transmission through the pass port of the TE ring.	4-13
4.8	Simulated spectra of (a) $T_3 = T_{ref,drop} \cdot T_{TE,drop}$ and (b) $T_A = T_{ref,drop} \cdot T_{TE,pass}$. The individual ring spectra that make up these Vernier cascades for the area in (a) and (b) which is marked by a red rectangle, are pictured in (c): $T_{ref,drop}$ in blue, $T_{TE,drop}$ in green and $T_{TE,pass}$ in red.	4-14
4.9	Vernier spectrum convolved with a Gaussian AWG channel of 0.5 nm wide. Through the sampled discrete points, a squared Lorentzian is fit to determine the peak position.	4-16
4.10	Classical limit of detection in function of the length of the sensor ring in a single polarization Vernier cascade for several AWG designs.	4-17
4.11	Measurement framework to determine the thickness and refractive index of a bound molecular layer to the surface of the microrings making up the dual polarization Vernier cascade.	4-19
4.12	Relation between the FWHM of the envelope of a Vernier cascade and the FWHM of the envelope obtained by filtering this Vernier through an AWG with channel width of 1 nm. The sensor ring has a length of 4 μ m. The envelope of the Vernier cascade is swept from 5 to 50 nm.	4-20
5.1	Resonance wavelength shift of the fundamental TE mode and fundamental TM mode of the BSA experiment in function of time.	5-3

-
- 5.2 Shift of a TE mode in a microring resonator from water to PBS with pH 3 and pH 7. The graph shows that the acidity has a small influence on the resonance wavelength of the cavity. 5-4
- 5.3 Thickness and refractive index profile of the layer consisting of adsorbed BSA molecules. 5-5
- 5.4 Adsorbed mass of BSA molecules to the silicon surface. 5-5
- 5.5 Evolution of the conformation of the BSA molecules as they adsorb to the silicon surface under influence of a change in pH value of the PBS buffer in which they are suspended. 5-6
- 5.6 Wavelength shifts of a TE mode during the attachment of (a) hynic silane to the silicon surface and (b) during the attachment of DNA probe 1 to the hynic silane. 5-11
- 5.7 Binding curves of hybridization in a PBS buffer containing (a) 25 v/v% and (b) 50 v/v% of formamide at 35°C 5-12
- 5.8 Shifts of the adsorption of HEG for different concentrations, together with the shifts of the subsequent complementary DNA-strand. Adsorption of HEG at sufficient concentration has a positive influence on the hybridization. 5-13
- 5.9 Binding curves of complementary DNA in 50 v/v % formamide in PBS pH 7.4 at 35°C (a) without the prior adsorption of HEG and (b) with a prior adsorption step of 1 mg/ml HEG 5-14
- 5.10 Shifts of a dual polarization measurement on a planarized SOI chip. Both the TE and the TM mode are plotted. 5-15
- 5.11 (a) Refractive index and (b) thickness profile during coupling of DNA probes to the surface and adsorption of 1 mg/ml HEG polymer5-15
- 5.12 Illustration of the sequences of the DNA detection assay. The silicon surface is silanized with a Hynic silane which can bind to a modified DNA probe containing a HEG spacer. In a second step, a HEG polymer adsorbs to the surface and reorients the DNA probes. Finally, hybridization takes place by means of a complementary DNA strand. 5-17
- 6.1 Schematic representation of the assembly with layer-by-layer technology of a microcapsule loaded with a drug component, by using a porous template. The drug is first inserted into a porous template, after which a bilayer polymer system is consequently wrapped around this template by the alternating coating with a positive polyelectrolyte and a negative polyelectrolyte. 6-2
- 6.2 On the left one cycle of the polymer experiment is shown as calculated from the shifts of the TE and the TM modes. Since the calculation is only correct when there is a water cladding above the waveguide and polymer layer, only these parts are retained in the final figure on the right. All following figures will be shown in this final form. 6-5

6.3	Recording of the wavelength shifts of a TE and TM mode during the whole bilayer experiment for (a) E1 and (b) E2: adsorption of a PEI layer, followed by 5 cycles of PSS/PAH bilayers. Zoom of the wavelength shifts during adsorption of the initial PEI layer for (c) E1 and (d) E2.	6-7
6.4	Refractive index and thickness profile during the first cycle of PSS/PAH for (a) E1 and (b) E2.	6-8
6.5	Illustration of homogeneous and integrative adsorption, two extreme cases of adsorption behavior, accompanied by their thickness and density profiles. Dual polarization sensing allows us to distinguish between these two. Bilayer 1 is characterized by t_1 and n_1 , while bilayer 2 is characterized by t_2 and n_2	6-9
6.6	Total mass of the multilayer stack during cyclic adsorption of PSS-PAH for (a) E1 and (b) E2. Thickness and refractive index for respectively (c) E1 and (d) E2.	6-10
6.7	(a) Incremental mass per cycle referenced to the total mass of the stack on which the layer in question adsorbs. (b) Incremental thickness per cycle referenced to the total thickness of the stack on which the layer in question adsorbs.	6-12

List of Tables

2.1	Design parameters of a coupling section sweep.	2-21
5.1	Comparison of the thickness, refractive index and adsorbed mass between the technique described in this paper (SOI Microring) and the silicon nitride dual polarisation interferometric (DPI) technique used in [4].	5-8
5.2	Thickness and refractive indices of the complete stack after silanization, attachment of DNA probe and adsorption of HEG.	5-16
6.1	Comparison of the characteristics of the adsorbed PEI layers, as recorded by the dual polarization microring for different experiments E1 and E2.	6-7
6.2	Comparison of the characteristics of the total stack consisting of PEI/PAH or PEI/PAH/PSS (the terminating layer is indicated by the subscript), as recorded by the dual polarization microring for different experiments E1 and E2.	6-9

List of Acronyms

A

AFM	atomic force microscopy
APTES	3-aminopropyltriethoxysilane
ATP	adenosine triphosphate

B

BSA	bovine serum albumin
-----	----------------------

C

CMOS	complementary metal-oxide-semiconductor
------	---

D

DMF	dimethylformamide
DNA	deoxyribonucleic acid

E

EtOH	ethanol
ER	extinction ratio

F

FDA	US food and drug administration
FIB-SEM	focussed ion beam - scanning electron microscopy
FWHM	full-width at half maximum
FSR	free spectral range

H

HEG	hexaethylene glycol
Hynic	hydrazinonicotinamide

L

LBDD	ligand-based drug design
LOD	limit of detection

M

MZI	Mach-Zehnder interferometer
-----	-----------------------------

N

NMR	nuclear magnetic resonance
-----	----------------------------

P

PBS	phosphate buffered saline
PDMS	polydimethylsiloxane
PEG	polyethylene glycol

Q

Q	quality factor
QCM-D	quartz crystal microbalance with dissipation monitoring

R

RCA	rolling circle amplification
RIU	refractive index unit

S

SEM	scanning electron microscope
SBDD	structure-based drug design
SOI	silicon-on-insulator
SPR	surface plasmon resonance
S-4FB	succinimidyl-4-formylbenzamide

T

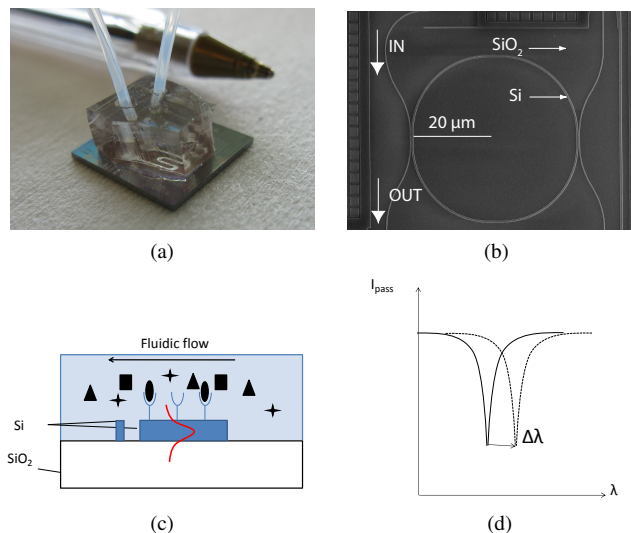
TE	transverse electric
TM	transverse magnetic

X

XPS	x-ray photoelectron spectroscopy
-----	----------------------------------

Nederlandstalige samenvatting

Gedurende de laatste tien jaar verkeert de farmaceutische industrie in een staat van crisis. Er worden maar mondjesmaat antwoorden gevonden voor de voornaamste hedendaagse aandoeningen zoals alzheimer, de ziekte van Parkinson, depressie, kanker, diabetes, etc. In diezelfde periode is de kost om een nieuw geneesmiddel van het lab naar de markt te brengen gestegen van 1 miljard euro in 2003 naar een duizelingwekkende 2,6 miljard euro in 2014, ofwel een jaarlijkse stijging van 8.5 %. Het lijkt erop dat het laaghangend fruit geplukt is en dat het huidige paradigma in geneesmiddelenonderzoek niet langer werkt voor deze nieuwe, complexe welvaartsziekten. Eén van de vaak terugkomende oorzaken in vakliteratuur voor deze malaise, is de beperkte kennis die we hebben wat de biologische fysica en moleculaire chemie betreft van de proteïnen en de geneesmiddelen die op deze proteïnen inwerken. Het vinden van een nieuw geneesmiddel is namelijk een iteratief semi-empirisch proces waarbij vooral gekeken wordt naar het vinden van moleculaire componenten die een goede binding vertonen met een bepaald proteïne, waarvan geweten is dat ze aan de oorzaak van een bepaalde aandoening liggen. Hoe deze binding er op moleculair niveau precies uitziet is daarbij vaak niet geweten. Het probleem ligt dus deels bij de onderzoekscultuur, maar ook bij de beschikbare tools om deze bindingen te bestuderen. Het is vanzelfsprekend dat om in te grijpen bij het falen van bepaalde moleculaire entiteiten in het menselijk lichaam, we tools nodig hebben die op dit zeer elementair en fysisch niveau kunnen kijken, daar waar alle bindingscomplexiteit tot uiting komt. Een belangrijke component van dit biofysische gedrag van moleculen is hun conformatie, wat zoveel betekent als hun vorm, opvouwing of ruimtelijke organisatie, en hoe die precies verandert onder invloed van binding of omgevingsfactoren. Proteïnen en andere biomoleculen zijn namelijk allermindst statisch, maar veranderen voortdurend van conformatie. Onderzoek heeft aangetoond dat deze (subtiële) conformaties een grote rol spelen in regulerende aspecten van het menselijk lichaam. Sterker nog, bepaalde degeneratieve ziektes zoals alzheimer hebben een directe oorzaak in deze conformaties. Het ontvouwen van bepaalde proteïnen zorgt er namelijk voor dat ze hun regulerende functie niet meer kunnen uitoefenen. Bovendien is er recentelijk vooruitgang geboekt door geneesmiddelen te produceren die via een conformationele verandering een proteïne kunnen deactiveren (allosterische binding). Deze geneesmiddelen zijn een stuk specifiek en accurater dan de traditionele geneesmiddelen die de binding met ATP, een moleculaire energie-eenheid, beletten (orthosterische binding). Deze ATP-bindingspockets zijn namelijk gemeenschappelijk voor een grote familie van proteïnen, met alle bijwerkingen van dien.

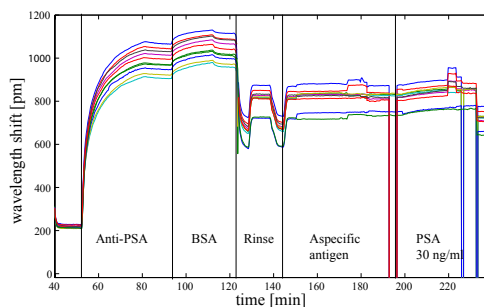


Figuur 1: (a) Afbeelding van de SOI-chip met een microfluidische cel uit PDMS, die bovenop de SOI-chip bevestigd werd. (b) Rasterelektronenmicroscopbeeld van een microringresonator met twee toegangsgolfgeleiders. (c) Illustratie van de doorsnede van de microringresonator met de receptormoleculen bovenop het ringoppervlak. (d) Spectrum van de uitgang van de toegangsgolfgeleider die de resonantiedip toont en de verschuiving hiervan onder invloed van een bindingsevent.

De huidige technieken die gebruikt worden om de structuur van een molecuul en diens dynamiek te bestuderen zijn echter niet erg geschikt voor het onderzoek in life science of de farmaceutische industrie. De voornaamste reden is dat veel technieken tekortkomen op vlak van resolutie, ofwel in de tijd (röntgendiffractie, fluorescentie), dan wel in de ruimte (ellipsometrie) om de dynamieken van een systeem te bestuderen dat doorgaans dimensies heeft kleiner dan 10 nm. Sommige technieken bieden wel een hoge resolutie, maar nemen erg veel tijd in beslag, vereisen getraind personeel om de uiterst complexe analyse uit te voeren, en hebben geen hoge verwerkingscapaciteit zoals nucleaire magnetische resonantie (NMR). Deze hoge verwerkingscapaciteit is cruciaal voor een technologie die geïntegreerd dient te worden in het onderzoek naar geneesmiddelen. Optische technieken die gebruik maken van een oppervlak waar de moleculen aan binden, kunnen informatie verschaffen over de conformatie van de moleculen door de dikte en de dichtheid van die dunne laag moleculen te bepalen. Deze technieken hebben vaak een hoge resolutie wat betreft de gebonden massa, maar hebben moeilijkheden om de dikte of dichtheid van die laag te bepalen. Een uitstekende techniek die dit wel kon, was de tweevoudigepolarisatieinterferometrie van het ondertussen opgedoekte Farfield Ltd, maar ook deze techniek had beperkte parallelisatiemogelijkheden, wat de doorvoercapaciteit belemmerde.

In deze doctoraats thesis hebben we een oplossing onderzocht voor dit probleem door middel van een microringresonator in het silicium-op-isolator-platform (SOI-platform), afgebeeld op Figuur 1(a,b,c). Doordat het standaard fabricatieproces voor elektronische chips ook gebaseerd is op silicium, betekent dit een gigantisch economisch schaalvoordeel t.o.v andere materialen. Veel fabricatietools, die duizenden chips per keer bakken, en de knowhow over dit materiaalsysteem, die de voorbije vijftig jaar is opgebouwd, kunnen immers in grote mate aangewend worden om optische chips te bakken. Door de extreem hoge kosten van dergelijke lithografische machines, bakken we de chips niet zelf. Dit wordt uitbesteed aan imec, een Leuvens bedrijf dat een wereldspeler is op het vlak van optische chips, via de dienst ePIXfab. Als een optische chip het analoog is van een elektronische chip, dan zijn de golfgeleiders dat van een elektrische koperdraad. Als met een dergelijke golfgeleider een gesloten cirkel gevormd wordt, spreken we van een microringresonator, afgebeeld met een elektronenmicroscop op Figuur 1(a). Deze component heeft de functionaliteit van een spectrale filter: als een tweede golfgeleider (d.i. de toegangsgolfgeleider) dicht genoeg tegen deze microring geplaatst wordt, dan plukt hij exact die golflengtes uit de golfgeleider die vrij kunnen propageren in deze microring. Alle andere golflengtes hebben een vrije doorgang langs de microring. Dit zorgt voor een dip in het uitgangsspectrum van deze toegangsgolfgeleider, zoals afgebeeld op Figuur 1(d). Anders dan de elektrische stroom in een koperdraad, zit niet al het licht perfect opgesloten in deze golfgeleider: een kleine fractie penetreert door de wanden van de golfgeleider en sterft dan exponentieel uit, weg van het oppervlak. Deze evanescente staart is de basis van het sensing principe van de microringresonator. Wanneer een biomolecule namelijk op het oppervlak van de microringresonator bindt, zal het licht dat propageert in de ring dit gewaarworden, waardoor de golflengtes die netjes in de ring passen, verschuiven. Door het licht in de toegangsgolfgeleider vervolgens van de chip te koppelen, kunnen we deze golflengteverschuiving opmeten. Opdat we met deze microringresonator bv. een specifiek antige zouden kunnen detecteren, moeten we eerst het oppervlak van de ring chemisch behandelen, zodanig dat er een antilichaam op kan gebonden worden. Vervolgens integreren we de optische chip met een microfluidisch kanaal om een oplossing met een onbekende hoeveelheid antige naar de ring te kunnen transporteren. Deze kanalen kunnen we eenvoudig met buisjes connecteren om zodoende een biomoleculair detectie-apparaat te verkrijgen. Op Figuur 2 staat een experiment afgebeeld waar een dergelijke microringresonator gebruikt wordt om een 30 ng/ml prostate specific antige (PSA) te detecteren, door eerst anti-PSA op het oppervlak te bevestigen.

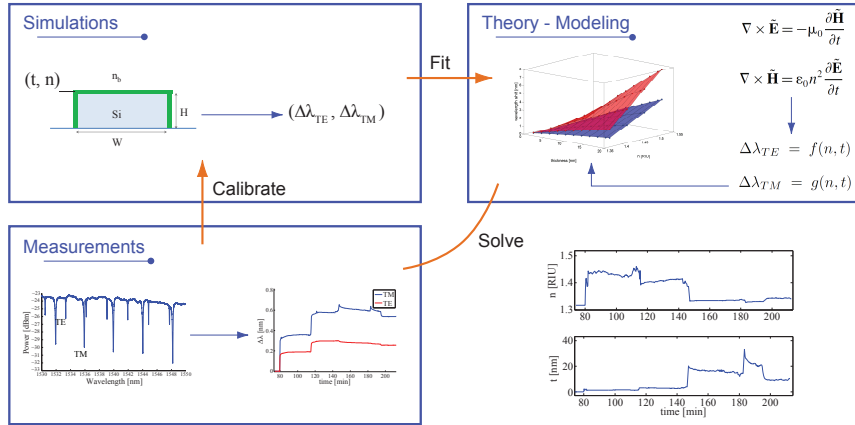
Deze microringconfiguratie verschaft ons echter geen informatie over de ruimtelijke aspecten van de proteïnen op de ring. De golflengteverschuiving is namelijk gerelateerd aan de optische dikte, wat het product is van de dikte (t) en de brekingsindex (n) van de dunne moleculaire laag. De optische dikte schaal op zijn beurt met de gebonden massa of de hoeveelheid biomoleculen op het ringoppervlak. Daarbij is n gerelateerd aan de massaconcentratie (d.i. de specifieke dichtheid) van het analiet in de gebonden laag. Dit betekent dat een microringresonator met en-



Figuur 2: Sensorgram van een microringresonator waarover een sequentie van biochemische moleculen gestroomd werden. Door PSA-antilichamen aan het oppervlak te binden, kon vervolgens een PSA antigen met concentratie van 30 ng/ml gedetecteerd worden.

kele golfgeleidermode, zoals hierboven beschreven, niet kan differentiëren tussen een dunne, dichte laag en een dikke, waterige laag. Om informatie te verkrijgen over de vorm, uitgereetheid, en de ruimtelijke verdeling van de moleculen op het microringoppervlak, is het noodzakelijk dat we de dikte en de brekingsindex onafhankelijk bepalen. Om dit te bewerkstelligen, koppelen we twee verschillende polarisaties in de microringresonator: een transversale elektrische (TE) polarisatie en een transversale magnetische (TM) polarisatie. Beide polarisaties hebben een verschillende set aan golflengtes die in de ring passen en een verschillende respons vanwege een bindingsevent op het oppervlak. Hierdoor kunnen we de contributies wegens dikte en wegens brekingsindex van elkaar ontkoppelen. Allereerst zijn we erin geslaagd om beide polarisaties simultaan in de microring te koppelen via een asymmetrische koppelsectie en één enkele toegangsgolfgeleider. Vervolgens hebben we de golflengteverschuivingen van beide modes geëxtraheerd uit het spectrum van die enkele toegangsgolfgeleider. Uiteindelijk hebben we een raamwerk gebouwd, dat bestaat uit calibratiemetingen, simulaties en fysische modellering, dat ons toelaat om de dikte en de brekingsindex te berekenen uit de opgemeten TE- en TM-golflengteverschuivingen (Figuur 3)

Dit systeem is vervolgens gekarakteriseerd en de kleinste verandering die kan worden opgepikt door het systeem (detectielimiet) is bepaald als minder dan 100 pm op de dikte en 1 mRIU op de brekingsindex, voor typische biomoleculaire lagen met een dikte groter dan 2 nm en een brekingsindex groter dan 1,41. De dunste laag met een aannemelijke brekingsindex ($n = 1,416$) die betrouwbaar kan worden gedetecteerd, d.w.z. met een relatieve fout op de dikte kleiner dan 10 %, is bepaald als slechts 0,75 nm groot. Dit is 7,5 maal groter dan de straal van een chloor-atoom, wat aantoont dat het met deze sensor mogelijk is om op moleculair

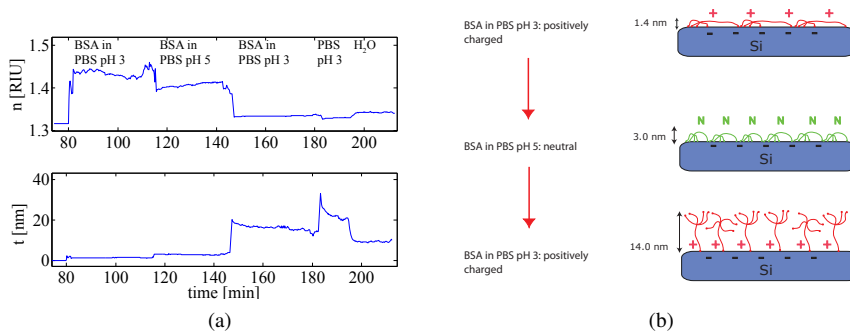


Figuur 3: Schematisch overzicht van de verschillende aspecten van het oplossingsraamwerk. Het spectrum wordt opgemeten en de golflengteverschuivingen van de TE en de TM mode worden hieruit berekend. Een deel van deze metingen gebruiken we om de golfgeleider in de simulaties te calibreren. Deze simulaties worden vervolgens gebruikt om een theoretisch model op te stellen. Uiteindelijk worden de golflengteverschuivingen aan de hand van dit model omgezet naar de dikte en de brekingsindex van de moleculaire laag.

niveau bindingen te analyseren. Om dit in perspectief te plaatsen: ellipsometrie, een techniek die gelijkaardig is in functionaliteit en fysische principes en de standaardtechniek om n en t te bepalen van een dunne laag, kan geen lagen resolveren die een dikte hebben dunner dan 10 nm. De mogelijkheid om lagen dunner dan 5 nm te bestuderen in hun natuurlijke natte omgeving, gecombineerd met gemakkelijke integratie van microfluidica, de mogelijkheid om standaard biochemische oppervlaktefunctionalisatie te hanteren, goedkope fabricatie en een hoge graad van parallelisatie of een hoge verwerkingscapaciteit, leiden tot een unieke tool die in staat is om systemen te bestuderen op moleculair niveau, wat zijn toepassing heeft in vele aspecten van life science en het onderzoek naar geneesmiddelen.

Om de verscheidene applicatiedomeinen van deze sensor toe te lichten hebben we ze gebruikt in drie aspecten van het onderzoek in life science: conformationele analyse van proteïnen, detectie van specifieke DNA-fragmenten en de fabricatie van slimme geneesmiddelcapsules met behulp van gelaagde polyelektrische systemen.

Eerst hebben we de conformaties van bovine-serum-albuminmoleculen (BSA-moleculen) bestudeerd terwijl ze adsorberen op het silicium oppervlak. Literatuur heeft aangetoond dat de pH-waarde van de buffer waarin ze opgelost zijn een invloed heeft op de conformatie van deze BSA-moleculen, die overigens een goed bestudeerde vorm hebben. Door deze experimenten te herhalen hebben we kunnen

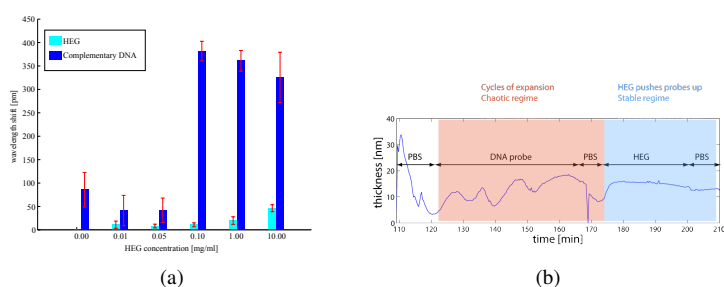


Figuur 4: (a) Dikte- en brekingsindexprofiel van een laag bestaande uit geadsorbeerde BSA-moleculen. (b) Evolutie van de conformatie van de BSA-moleculen, terwijl ze adsorberen op het silicium oppervlak onder invloed van een veranderende pH-waarde van de PBS-buffer waarin ze opgelost zijn.

verifiëren dat onze sensor conformationele veranderingen kan oppikken op een betrouwbare manier. We hebben inderdaad kunnen opmeten dat de BSA-moleculen hun vorm aanpassen aan de pH-waarde van de buffer (zie Figuur 4), en de opgemeten dimensies komen goed overeen met diegene in de literatuur.

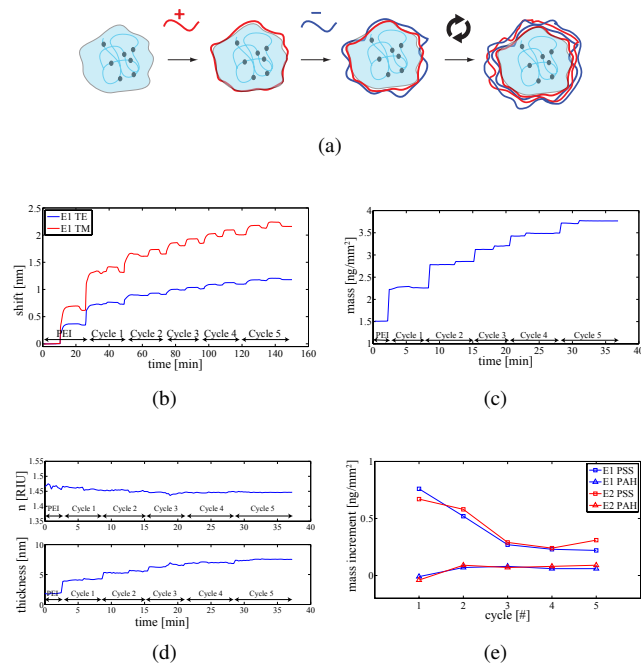
Ten tweede is er een DNA-detectieplatform ontwikkeld in samenwerking met de vakgroep polymeerchemie en biomaterialen van UGent (PBM-UGent). In het bijzonder was het werk van Anabelle van Eeghem, Sam Werquin, Arne Goes en Prof. Dubruel daarbij van cruciaal belang. Een snel detectieplatform voor bepaalde sequenties van nucleotiden (DNA of RNA) is erg in vraag in bepaalde diagnostische settings. Zo is bijvoorbeeld de snelle identificatie van een infectie door het viraal RNA te detecteren noodzakelijk. Op deze manier kunnen de hoge hoeveelheden antibiotica die op dit moment nutteloos worden ingenomen, terugschroefd worden. Ook in kankerdiagnostiek vindt een dergelijk detectieplatform zijn toepassingen. Wanneer men de genetische blauwdruk van een tumor kan bepalen aan de hand van een aantal biomerkers op DNA-niveau, is men in staat om a priori te bepalen voor welke behandelingen een bepaalde patiënt al dan niet in aanmerking komt. Deze zogeheten gepersonaliseerde diagnostiek is een trend die in veel takken van de geneeskunde haar intrede vindt. In veel dergelijke DNA-platformen werkt het detectieprincipe via hybridisatie: een complementaire DNA-streng wordt vastgehecht aan het oppervlak. Deze streng doet dienst als biomarker om een bepaalde genetische sequentie te detecteren in een onbekend staal. Gezien de uitgestrektheid en de flexibiliteit van DNA-strengen, is de oriëntatie van de DNA-streng op het oppervlak erg bepalend voor de daaropvolgende hybridisatie. Het is echter vaak onmogelijk om de oriëntatie van deze strengen in-situ te volgen wegens een gebrek aan tools met een voldoende hoge (dynamische) resolutie.

Met de tweevoudigepolarisatietechniek hebben we vastgesteld dat een hexaethyleen glycol (HEG) polymeer zich tussen de probes nestelt en deze in een meer rechtopstaande positie duwt en de stabiliteit van de laag DNA-strengen verhoogt (Figuur 5(b)). Dit leidt tot een verhoging van de hybridisatie-efficiëntie met een factor 3 tot 4 (Figuur 12(a)). Met dit experiment toont de tweevoudigepolarisatietechniek dat ze ook kan worden gebruikt als een directe optimalisatietechniek om de biochemische oppervlaktefunctionalisatie van detectieplatformen te verbeteren, wat steeds een heikel punt is van deze assays.



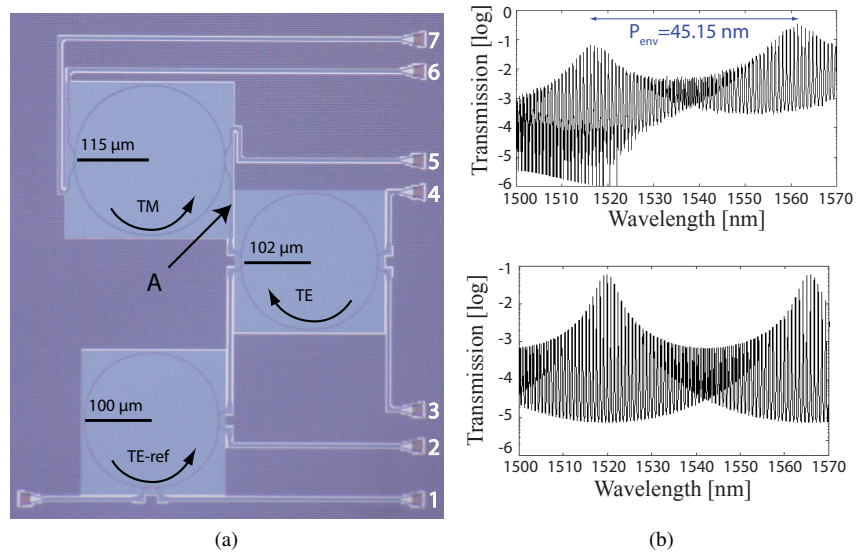
Figuur 5: (a) Hybridisatie-efficiëntie van een complementaire DNA-streng in functie van de HEG-concentratie. Een verhoging van de efficiëntie met een factor 3 tot 4 is verkregen met voldoende HEG-concentratie. Data opgemeten door Anabelle van Eeghem. (b) Dikteprofiel opgemeten tijdens de binding van een DNA-streng op het oppervlak, gevolgd door de adsorptie van 1 mg/ml HEG-polymeer.

In een derde serie experimenten hebben we de sensor toegepast op een polyelektrisch tweelagensysteem, dat gebruikt wordt als een nieuw nanomateriaal om geneesmiddelmoleculen mee te encapsuleren. Deze zijn in staat om door de celwand heen te manoeuvreren, terwijl het moment van afgifte van de inhoud contextsensitief kan worden gemaakt door middel van de eigenschappen van de lagen. Een dergelijke microcapsule kan worden gemaakt door bv. een paar dunne lagen rond een poreus materiaal waarin het geneesmiddel zich bevindt, te adsorberen (zie Figuur 6(a)). Er is echter weinig geweten over de eerste paar lagen die op het substraat adsorberen, aangezien deze slechts een paar nanometer dik zijn. Wij hebben de adsorptie van de eerste 5 cycli van een tweelagensysteem bestudeerd met behulp van de microringresonator. Figuur 6(b) toont de opgemeten golflengteverschuivingen van de TE en de TM mode. Daarmee kan de geadsorbeerde massa bepaald worden (Figuur 6(c)) alsook de dikte en de brekingsindex (Figuur 6(d)). Deze tonen een erg stabiele, stapsgewijze opbouw, waarbij de massaconcentratie stabiel blijft over de verschillende cycli heen. Verder kunnen we een duidelijke overgang van een interfaceregime naar een bulkregime constateren na 2 cycli (Figuur 6(e)). Dit experiment toont dat deze techniek kan gebruikt worden voor adsorptiefysica van dunne lagen.



Figuur 6: (a) Illustratie van een mogelijke constructie van een microcapsule door middel van de tweelagentechnologie die zich rond een poreus materiaal wikkelt waarin een geneesmiddel bevat zit. De positief en negatief geladen polyelektrische lagen adsorberen beurtelings rond het poreus materiaal om zo de capsule te vormen. (b) Golfteverschuiving van TE en TM modes gedurende de adsorptie van 5 cycli op het oppervlak van de microring. (c) Gedeponeerde massa en (d) dikte- en brekingsindexprofiel. (e) De toegevoegde massa per cyclus van twee verschillende experimenten.

De meetsetup die gebruikt werd om de microring uit te meten voor deze experimenten bestaat o.a. uit een laser met instelbare golflengte en een camera, waardoor tijdsresoluties kunnen worden behaald van 0.1-1 seconde. Om snelle conformatie- veranderingen op te meten is een tijdsresolutie van 1 milliseconde echter aangewezen. Dit kan verkregen worden door drie microringen te combineren in een tweevoudigepolarisatie-Verniercascadeontwerp (Figuur 7). Op die manier kan een signaalversterking van 250 verkregen worden, zodat een instelbare laser niet langer nodig is om de kleine golflengteveranderingen op te meten. Deze versterkte verschuivingen kunnen opgesplitst worden over verschillende golflengtekanalen met een breedte van 1 nm. Elk kanaal wordt dan met een aparte golfgeleider met een uitgangskoppelaar verbonden, die dit kanaal afbeeldt op een afzonderlijke pixel op de camera. Hierdoor kan het volledige spectrum in parallel worden opgemeten met behulp van een breedbandige LED, in tegenstelling tot de setup met een laser die golflengte per golflengte sequentieel opmeet. Met een snelle camera



Figuur 7: (a) Elektronenmicroscopbeeld van een tweevoudigepolarisatie-Verniercascadeontwerp bestaande uit drie microringen. (b) Opgemeten en gesimuleerd spectrum van poort 3.

kunnen we zo de tijdsresolutie verhogen met een factor 2000, terwijl de kost van het uitleessysteem met twee grootteordes verminderd wordt. Dit design met driedvoudige ringresonator is gefabriceerd, gekarakteriseerd en vervolgens geverifieerd met simulaties. Met behulp van een nieuw uitmeetraamwerk is aangetoond hoe de dikte en de brekingsindex uit deze gecompliceerde spectra kan geëxtraheerd worden. Uiteindelijk hebben we aangetoond dat dit systeem robuuster is doordat een zelf-refererend principe gehanteerd wordt dat gemeenschappelijke ruisfactoren afzwakt. Via theoretische afleidingen is aangetoond dat een verbetering van de detectielimiet mogelijk is, zowel met als zonder de hogere temporele resolutie in rekening te brengen.

English summary

For over ten years now, the pharmaceutical industry is having major difficulties providing answers to the diseases of our time: Alzheimer, Parkinson's disease, depression, cancer, diabetes, etc. At the same time, the cost of the complete product development cycle of a new drug is rising at an average of 8.5% per year since 2003 to a staggering \$1-2.6 billion today (source dependent). The easy targets have been hit and the current drug development paradigm does not seem to work for these complex diseases of civilization. This evolution has been studied in scientific and popular literature alike and one of the main problems is the lack of knowledge we have on the biophysics and molecular chemistry of the proteins and drug candidates they interact with. This is as much a problem of industry culture as it is of the available tools we have. It only makes sense that in order to interact with the intricate biomolecular deficiencies which often cause these diseases, that we need the tools to observe and study these phenomena at their most native level of complexity. One major component of this biophysical behavior is the conformations or the shape dynamics these biomolecular actors have. These conformations play a big role in all regulatory aspects in the human body. At the same time, they are often the direct cause of a disease through a misfolding of a crucial protein, which is for example the case for some degenerative diseases. Furthermore, recent progress shows that drugs which directly influence the conformations of certain proteins (allosteric binding) can be more specific and more accurate than those who do not.

However, the techniques that are being used for the analysis of the shape of biomolecules are not well-adopted to be integrated in life science research or the pharmaceutical industry. Most of the options lack the resolution, either in time (crystallography, labeled fluorescence) or in space (ellipsometry), to study dynamics of sub-10 nm systems. Some techniques like nuclear magnetic resonance do offer high resolution but are very time-consuming and require highly trained personnel to analyze the complex set of data. Furthermore, these techniques rarely offer high-throughput capacities, which is important to integrate the tool in the context of drug research. A different set of optical techniques bind the molecules to a surface (e.g. surface plasmon resonance) and could provide information on the conformation by means of the thickness and density of the thin molecular layer on this surface. Although these techniques are easily integrable with microfluidics, are often high-throughput and have high resolution in bound mass, they have difficulties determining the thickness or the refractive index of this layer independently.

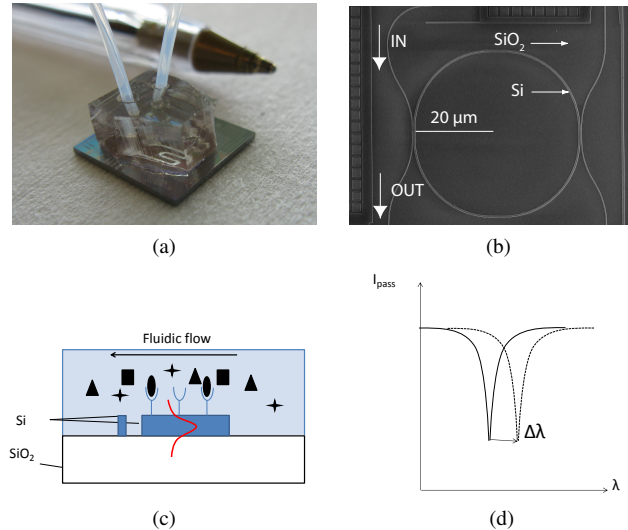


Figure 8: (a) Picture of the SOI chip with bonded PDMS microfluidic cell on top, connected with tubings. (b) SEM image of a microring resonator with two access waveguides. (c) Illustration of the ring cross section that shows the receptor molecules on top of the ring. (d) Spectrum of the output of the access waveguide, showing the resonance dip and the shift in wavelength due to a binding event.

An excellent technique such as the dual polarization interferometry technique by the now defunct Farfield Ltd has made advances in this respect, but is lacking any multiplexing capabilities to be integrated in a high-throughput research environment such as drug research.

We have attempted to offer a solution for this problem by using a microring resonator in the silicon-on-insulator (SOI) platform, shown in Figure 8(a,b,c). Working with this technology allows cheap mass-production of photonic chips by using the same lithographic tools which are being used in CMOS electronics industry. Due to the stellar costs of these tools, we do not fabricate these chips ourselves. They are fabricated by imec, located in Leuven, which is one of the world leading players in silicon photonics chip technology, through the ePIXfab service. A photonic chip is the optical analogue of an electronic chip, and the waveguide that of an electrical wire. When a waveguide is routed in a closed circle, it forms a microring resonator. These resonators function like a wavelength filter: when a second waveguide is placed close enough, the microring picks up the wavelengths which can propagate freely in the ring and lets the other wavelengths pass unaltered. This creates a dip in the spectrum of the access waveguide as shown in Figure 8(d). Different from an electrical wire however, the light in a waveguide is not fully confined to it: a small fraction of the light can penetrate through the waveguide surface. This portion is called the evanescent tail since it decays ex-

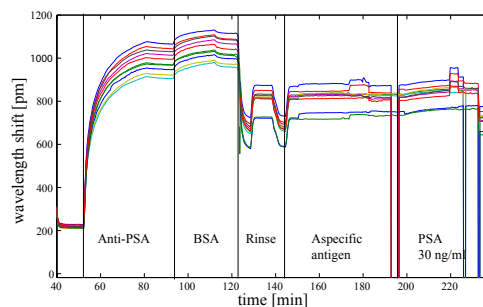


Figure 9: Sensorgram of a microring resonator where a series of molecular agents were bound to the ring surface. By attaching an antibody to protein specific antigen (PSA), we could detect PSA with a concentration of 30 ng/ml

ponentially away from the core, and it is this tail which allows us to use these microrings for sensing. If a biomolecule would bind to the surface, the light in the microring would "feel" this and the wavelength which fits in the ring would change, which we can measure by coupling the access waveguide off the chip. To make these microrings detect e.g. a specific antigen, we can chemically modify the surface such that the antigen's antibody can be linked to it. By integrating these photonic chips with microfluidic channels to transport the analytes to the ring surface, we obtain a specific biomolecular detection device (pictured on Figure 8(a)). On Figure 9, an experiment is shown where we have used such a microring to detect 30 ng/ml of PSA, by attaching anti-PSA to the surface.

This microring configuration does not give us any information on the shape of the biomolecules bound on top however. The wavelength shift is related to the optical thickness $n \cdot t$ of the bound layer, which is linked to the deposited mass or the number of biomolecules which bind on top. The refractive index (n) is directly coupled to the mass concentration (a measure for specific density) of the analyte in the bound layer on the chip surface. This means that a single waveguide mode can't distinguish between a thin dense layer and a thick sparse layer. To gain information on the molecule's shape, elongation and distribution on the waveguide surface, we require the thickness and refractive index to be determined independently. In order to do so, the microring is excited with two different polarizations simultaneously: a transversal electric (TE) polarization and a transversal magnetic (TM) polarization. Due to the different response of both modes to a binding event on top of the microring, the contributions to thickness and refractive index can be disentangled. In a first step we managed to excite both polarizations simultaneously through an asymmetrical coupling section, with a single access waveguide. Next, the shifts of both resonant modes were extracted from the gathered spectra

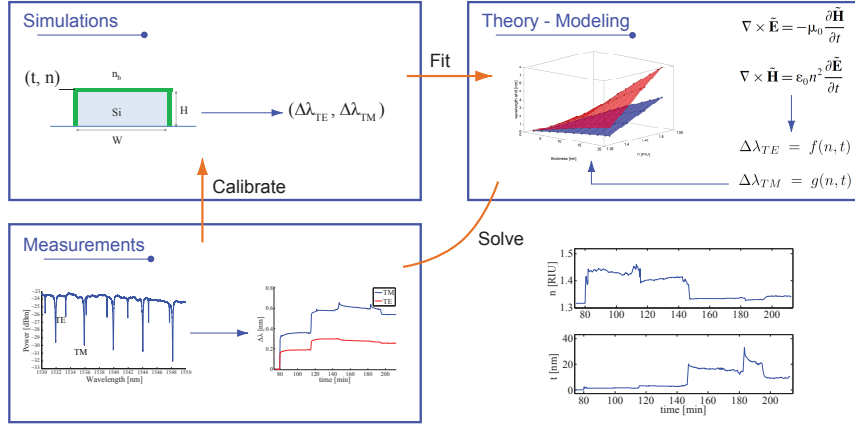


Figure 10: Schematic overview of the different aspects of the solving framework. The spectrum is measured and the peaks of the TE and TM modes are tracked. This feeds into the simulations to calibrate the waveguide profile. These simulations are fit to a theoretical model, derived from waveguide theory. Finally, the measured shifts are solved with this model to obtain the thickness and refractive index profile.

of this access waveguide. Finally, a framework was built, containing calibration measurements, simulations and physical modeling which allows the extracted resonance wavelength shifts of both TE and TM modes to be solved to a thickness (t) and refractive index (n) profile (Figure 10).

Analysis on system level has led to determining the limit of detection on thickness to be less than 100 pm and on refractive index to be 1 mRIU, for a layer which is larger than 2 nm in size and has a refractive index over 1.41. The thinnest layer which is reasonably dense ($n=1.416$) that can be faithfully detected (with a relative error smaller than 10% on thickness) is determined to be only 0.75 nm thick. This is 7.5 times bigger than the radius of chlorine atom, and shows that this technique is capable of analyzing molecular-size systems. To put this in perspective: ellipsometry, which is similar in function and physics and is the standard technique to obtain thickness and refractive index of a thin layer, is not able to resolve layers which are thinner than 10 nm, while being less practical to integrate with fluidic components. The capability to analyze sub-5 nm layers in a native wet environment, combined with easy microfluidic integration, standard biochemical surface functionalization strategies, cheap fabrication and high multiplexing, make for a unique tool which can study molecular-size systems in many aspects of life science and drug development research.

To highlight the various domains of application of this novel sensor, we have applied it to three different aspects of research in life science: conformational analysis of proteins, DNA detection assays and fabrication of drug capsules via

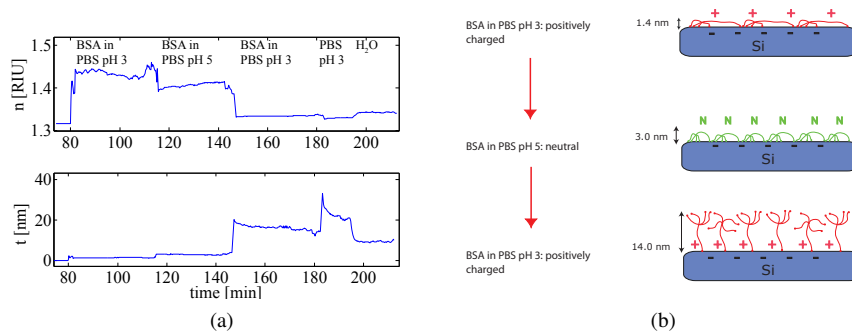


Figure 11: (a) Thickness and refractive index profile of the layer consisting of adsorbed BSA molecules. (b) Evolution of the conformation of the BSA molecules as they adsorb to the silicon surface under influence of a change in pH value of the PBS buffer in which they are suspended.

multilayer polyelectrolyte systems.

In a first experiment, we studied the conformations of BSA molecules while they adsorb to the silicon surface. It was shown in literature that the pH value of the buffer has an influence on the conformation of the BSA molecules, which have a well-known shape. By repeating these experiments we could verify that our sensor can pick up conformational change in a reliable way. The conformational changes due to a change in pH-value of a buffer were indeed observed (see Figure 11), and the measured dimensions agreed well with literature.

Second, a DNA detection assay was developed in cooperation with the polymer chemistry and biomaterials group of UGent. Primarily, the contributions of Anabelle van Eeghem, Sam Werquin, Arne Goes and Prof. Dubruel were instrumental in this development. With their help, the detection of single-stranded DNA was achieved. A fast detection assay for specific nucleotides is highly desired in diagnostic settings. For example, the quick identification of an infection through its viral RNA can reduce the amount of unnecessary intake of antibiotics. In cancer therapy, the genetic fingerprint of a tumor cell can be obtained in order to determine a priori which therapy might be more successful for a specific patient. In most surface DNA assays, the detection works via hybridization: a complementary single-stranded DNA probe is attached to the surface which serves as a biomarker to detect a specific genetic sequence. The orientation of this surface probe is decisive for efficient hybridization. However, it is notoriously difficult to gain insight in the in-situ orientation of these probes due to a lack of high-resolution tools which can track these in their native condition. Using the dual polarization technique, we observed that the adsorption of a hexaethylene glycol(HEG) polymer after the

probes were attached, reorients them in an upright position and locks the overall shape of the probes (Figure 12(b)). This led to a significant 3-4 times increase in hybridization efficiency (Figure 12(a)). The added value of the dual polarization technique in this experiment shows it can serve as an enabling technology to improve the biochemical functionalization of many existing surface assays.

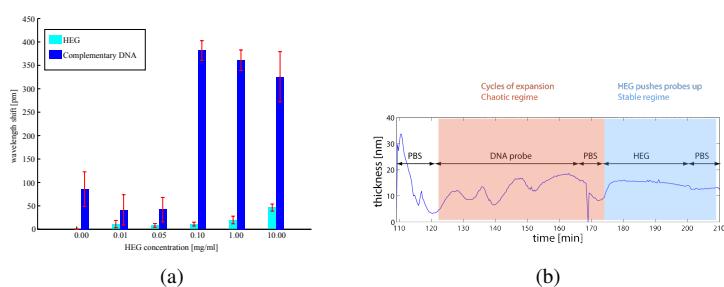


Figure 12: (a) Hybridization efficiency of the complementary DNA-strand in function of the concentration of the adsorbed HEG polymer. Adsorption of HEG at sufficient concentration shows a 3-4 fold increase in hybridization efficiency. Data obtained by Anabelle van Eeghem. (b) Thickness profile during coupling of the DNA probe to the surface and subsequent adsorption of 1 mg/ml HEG, explaining the increased hybridization efficiency due to a reorientation of the DNA probes.

In a third series of experiments we have applied the sensor to polyelectrolyte bilayer systems which are used as a novel material for drug vessels. They form as a few thin layers around e.g. a porous template in which the drug is loaded, as illustrated in Figure 13 (a). These new nanomaterials are highly engineerable and allow to the drug vessel to traverse the cell membrane. The unloading of the drug content can for example be made context-sensitive by means of the properties of the polyelectrolytes. Literature shows that little is known about the first interface layers adsorbing to a substrate, since these are typically only a few nanometers in size. We tracked the adsorption of the first five bilayer cycles on top of the microring resonator. Figure 13(b) shows how the wavelength shifts of the TE and TM modes are tracked, which are solved to the deposited mass (Figure 13(c)) and the thickness and refractive index profile (Figure 13(d)). These show a stepwise increase in thickness, while the refractive index stays relatively constant over the different cycles. Using the dual polarization technique, we could clearly distinguish the interface from the bulk regime, which sets in after 2 cycles (Figure 13(e)). Furthermore, the first PEI layer was clearly observable although it is only 1 nm thick, offering an experimental verification of the resolving power of the system. This experiment shows the applicability of this technique to adsorption physics in general.

The setup with a single microring and a tunable laser which has been used for

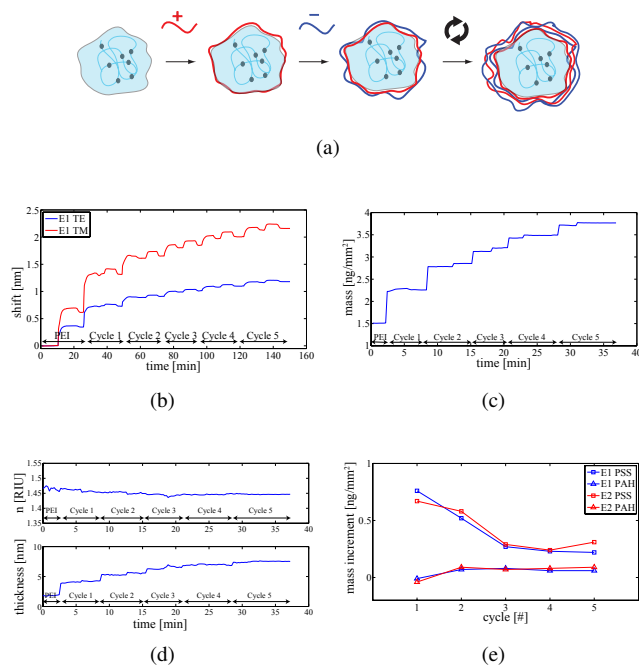


Figure 13: (a) Schematic representation of the assembly with LbL technology of a microcapsule loaded with a drug component, by using a porous template. The drug is first inserted into a porous template, after which a bilayer polymer system is wrapped around this template by the alternating coating with a positive polyelectrolyte and a negative polyelectrolyte. (b) Wavelength shifts of TE and TM mode recorded during the adsorption of 5 cycles of the bilayer system. (c) Deposited mass and (d) thickness and refractive index profile. (e) Mass increment per cycle of two different experiments showing an interface and a bulk regime.

these experiments, offers time resolutions in the order of 0.1-1 second. For fast conformational changes, a time resolution in the order of milliseconds would be better. By combining three microrings in a dual polarization Vernier cascade design (Figure 14), a signal amplification in the order of 250 can be attained, such that we no longer require a tunable laser to read the small microring wavelength shifts. These amplified shifts can be split in wavelength channels with an on-chip arrayed waveguide grating (AWG) with a channel width of 1 nm. Every channel is then routed to a dedicated output coupler, which images it on a separate pixel of a camera. This means that we can measure the complete spectrum in parallel by exciting the sensor with a broadband LED as opposed to the tunable laser which fires the wavelengths one-by-one. With a fast-enough camera, we can improve the time resolution this way by a factor of 2000, while reducing the cost of the read-out system by two orders of magnitude. The triple ring transducer has been fabricated,

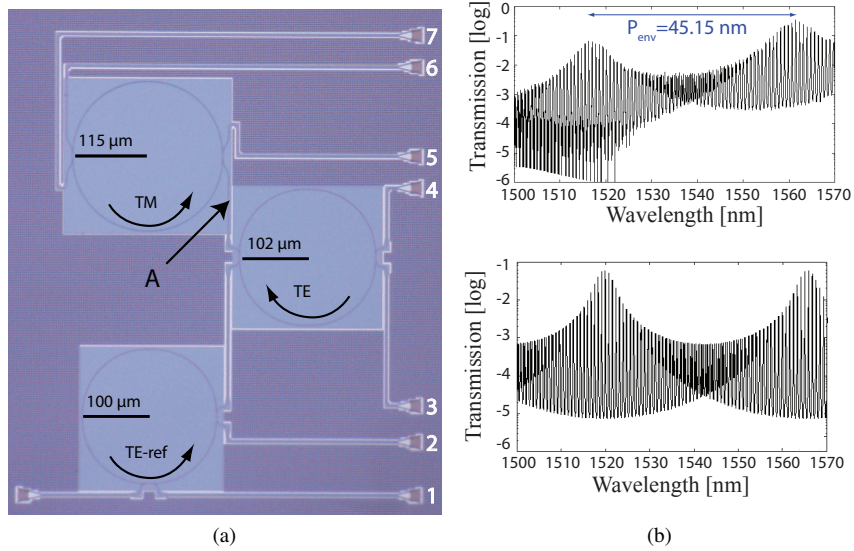


Figure 14: (a) SEM picture of a dual polarization Vernier design consisting of three SOI microrings. (b) Measured spectrum at port 3, and simulated spectrum at port 3

characterized and matched with simulations. By providing a measurement framework, we show how the thickness and refractive index can be extracted from these complicated spectra. Finally, we show that this system is more robust due to a reduction of common noise factors via the inherent self-referencing. A theoretical improvement of the limit of detection is shown, with and without including the effects of an improved temporal resolution.

1

Introduction

1.1 Inertia in pharma

The pharmaceutical industry is in a state of crisis since 2005-2007. The low-hanging fruits have been picked and the advent of new drugs for widespread diseases remains low. Alarming signs can be seen in the number of approvals by the U.S. Food and Drug Administration (FDA) for new drugs, as it has decreased from 45 in 1996 to a yearly average of 21.9 between 2005 and 2010 [1]. At the same time, costs for development are rising. A 2014 report by Tufts (Center for the study of drug development) shows that the total development cost of a drug compound up until market approval is estimated at \$ 2.6 billion [2], with a development cycle of over 10 years. A similar report was made in 2003, where the costs were estimated at \$802 million. Averaged out, we are looking at an annual growth rate of 8.5 % on the drug development cost. At the income side, big pharmaceutical players such as Novartis, AstraZeneca and Pfizer see their revenues shrinking due to the recent evaporation of key patents. The patents for many of the biggest-selling drugs have started to expire from 2013 onwards, allowing smaller companies to release generic drugs on the market at a reduced price. This resulted in massive layoffs in the R&D sectors of the big companies. The FDA 2015 summary of drug approvals shows the reorientation of the industry due to this massive disruption. They conclude that more orphan drugs, which are drugs intended to treat rare diseases usually not considered to generate sufficient revenue, than any previous year in their history have been approved. Furthermore, 60% of the approvals

are improvements over existing therapies, also a record in their track history [3]. These new directions do not generate the results which they hoped for. Deloitte and Thomson Reuters show that the average forecast for the peak sale of an asset declined by 43% from \$866 million dollars in 2010 to \$466 million in 2013 [4]. The internal rate of return of R&D has also dropped by half in the same period to 4.8%. The increasing cost and lower revenue can only be compensated for if these new specialty and orphan drugs are very expensive. Indeed, a 2014 EvaluatePharma report shows that the median price of the top 100 selling drugs in the USA increased seven-fold, from \$1,260 in 2010 to \$9,400 in 2014 [5].

This major decrease in development efficiency is not due to a lack of medical conditions to be treated, but due to a mismatch in the killer conditions of our time such as diabetes, cancer and Alzheimer and the methodology that is being used. The ruling paradigm which worked wonders before the turn of the millennium is no longer an efficient one, in spite of the euphoria related to the sequencing of the human genome in 2000. This was realized by the FDA and they launched the FDA Critical Path Initiative in 2004 to address the increasing difficulty and unpredictability of medical product development [6]. A major point of attention was that a better product development toolkit is urgently needed. In a 2011 *Nature Chemistry Insight* [7], the authors state that the reason for the high failure rate in drug development can be found in the lack of appropriate high-throughput tools to study molecular behavior **at an analytical and biophysical level**. There is for example little knowledge on the subtle changes in conformation (i.e. shape) of proteins or enzymes, even though they are defining for cell metabolism and the failure thereof, leading to illnesses. Evidently, medication should take notice and attempt to manipulate these fundamental processes. Current degenerative diseases (Alzheimer, Huntington, Parkinson, etc.) that prove difficult to produce effective drugs for, often find their cause in this misfolding of crucial proteins [8]. It is confirmed in the Tufts report that one of the reasons for the money drain in drug development, is the difficulty of targeting chronic and degenerative diseases [2]. This has its roots in the traditional screening of drug candidates, which largely neglect these biophysical phenomena. It is a very empirical, hit-and-miss affair. The selection of appropriate targets to go through with, is often based on binding metrics such as affinity and rate of association, which obscure the underlying conformations.

1.2 Proteins' hidden dance

In recent review articles, the importance of the conformation of the actors of a biological binding event is confirmed. Fenwick et al. pointed out the relevance

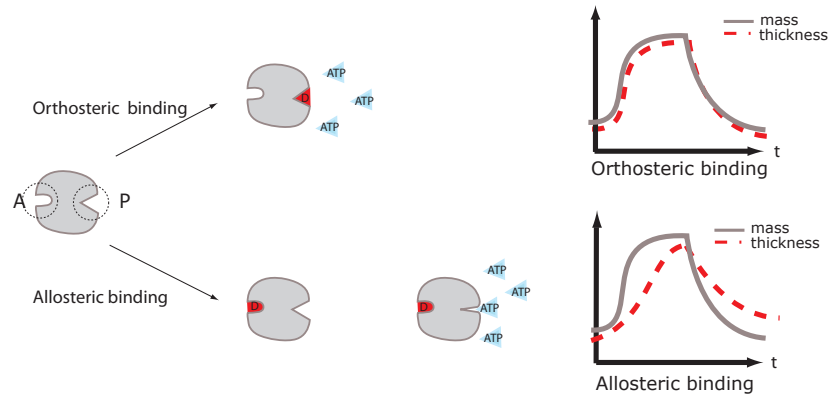


Figure 1.1: Illustration of orthosteric and allosteric binding, and the response of a sensor that can track mass as well as thickness. The protein has a primary binding site, indicated by P and an allosteric binding site, indicated by A. When ATP binds in the primary binding site, the protein is activated. In orthosteric binding, the drug ligand inhibits this primary binding site, while in allosteric binding, the drug ligand binds at a secondary binding spot, to render the primary binding spot inaccessible by conformational change. ATP is indicated in blue, while the drug is indicated in red.

of conformation for the analysis of general biomolecular dynamics and molecular recognition [9], while its key role in protein function and regulation has been stressed recently by Hatzakis et al. [10]. For example, in order for a certain protein to move from the place of synthesis to its target structure inside the cell, it needs to traverse the cellular soup, crowded with other biological agents. To prevent being manipulated or even activated at the wrong place, the protein conforms in a closed state and only opens up where it is needed.

A very tangible example of where a conformational biosensor can make a difference, is to differentiate between orthosteric and **allosteric binding** of a drug ligand, as illustrated in Figure 1.1. Orthosteric binding is the traditional method for drugs to shut down certain proteins associated with a condition. The primary binding site of a protein is often used for activation by binding with adenosine triphosphate (ATP). The drug ligand binds to this site and as such inhibits the binding of ATP. However, these ATP binding pockets are similar for a wide range of proteins belonging to a certain class, hence the side-effects often accompanying the intake of medicines. A different strategy is to bind away from this primary site, at an allosteric site. Binding at an allosteric site can induce a conformational change which renders the primary site not accessible, shutting down the protein as well. While orthosteric binding is a competitive reaction between the drug ligand and the ATP molecule, an allosteric site with little binding competition by native

molecules can be found, reducing the necessary amount of drugs. Also, allosteric sites can be topographically different from one another and hence allosteric drugs can differentiate between subtypes of a certain family. For a traditional mass or concentration sensor, it is impossible to know where exactly on the protein the ligand has bound. However, by acquiring a conformational signal (e.g. thickness of a bound layer), the time delay between the mass increase and the conformational change can be a differentiator towards the type of binding, as it is expected that there is a delay in the order of 100 ms between the two signals in the case of an allosteric binding. The potential of allosteric binding has been shown in several domains of pharmacology. In the field of cancer research, protein kinases are often targeted and their functionality is known to be exceptionally sensitive to its conformation [11]. This led to the advent of imatinib, the first small-molecule kinase inhibitor, lending its efficiency to its allosteric nature. In its wake, other conformational inhibitors look promising, for e.g. RAF kinase [12]. Furthermore, many psychiatric and neurological disorders are related to the functioning of a subclass of G protein-coupled receptors. In contrast to traditional orthosteric inhibitors, allosteric modulators have proven to be subtype-selective and are exciting potential therapeutics for Alzheimer, anxiety, depression, epilepsy and Parkinson's disease, amongst others [13]. In the research concerning HIV infections, advances have been made by stabilizing CCR5 receptors on the surface of white blood cells in a conformation that has a lower affinity for the HIV virus, blocking its entry into the cells [14].

However, the leverage that a better understanding of the conformational aspects of biomolecular interaction could have on the development of new chemicals is not reflected by the available tools to study these subtle dynamics. In the examples given, the conformations are often studied with sub-optimal tools, computer modeling, or indirect measurements. The conformational change *an sich* is hardly measured due to a lack of resolution, either in time or space, let alone in a high-throughput way, a much-wanted feature for integration in pharmaceutical development.

1.3 Current landscape of conformational tools

Obtaining structural information of organic molecules is a field for which many techniques exist. However, for these classical techniques to also detect dynamic structural information during an interaction is a different story. Getting this information on a time resolution so as to detect subtle conformation dynamics is extremely challenging. In general, the tools providing this information can be subdivided in three categories: computational, labeled, or labelfree. The technique

we present in this thesis is a label-free technique so we will focus on sketching the landscape of label-free techniques. For completeness however, computational techniques can provide a virtual screening for binding partners of drug ligands and a protein. Based on knowledge of the 3D-structure of the protein, the small-molecule, or neither, techniques such as structure-based drug design (SBDD), ligand-based drug design (LBDD) and sequence-based design can be used [15]. These methods are relatively cheap, very high-throughput, but generally require accurate experimental data to render the results reliable. Labeled techniques use the introduction of (usually) a fluorescent label, which can be a fluorescent protein or a chemical dye. The cloning of the green fluorescent protein (GFP) from a jellyfish in 1992 propelled this research domain forwards [16]. GFP and other fluorescent proteins can be used in combination with Förster Resonance Energy Transfer (FRET) to detect conformational change. When a single fluorophore is brought in close proximity to a second fluorophore, the energy that the first fluorophore would otherwise use to emit photons, can be transferred in a non-radiative way to the second fluorophore, such that it can relax via fluorescence itself. This phenomenon is very sensitive to the distance between the two fluorophores, which should be under 10 nm to produce a FRET signal. By introducing two fluorescent proteins at different locations on the protein, conformational changes can be observed by tracking the fluorescence intensities of both [17]. While the sensitivity of these labeling techniques is often very high, the introduction of a label disrupts the natural behavior of the biomolecules-under-test. The molecular weight of GFP is approximately 27 kDa, similar to the proteins or larger than the small molecules it wishes to study. Furthermore, labeling is a costly and labor-intensive affair with little high-throughput possibilities. In contrast, label-free techniques do not require the use of a label, but detect the analyte via direct transduction of certain physical parameters.

1.3.1 Label-free sensing

Two of the most long-used techniques for structural analysis of proteins are X-ray crystallography and nuclear magnetic resonance (NMR). X-ray crystallography has solved 93466 3D protein structures to date, which makes it the most prolific structural technique, while nuclear magnetic resonance comes in second with 9723 solved structures [18]. X-ray crystallography captures the pattern of X-rays as they diffract on a crystallized sample which can be used to reconstruct the 3D-structure. This ancient technique however requires the molecules to be crystallized and can only generate static information. It is still very relevant today though, to locate novel binding sites, as shown in [19] where it is used in HIV research. While NMR was traditionally used for the determination of 3D-structures, the technique

can be used to study dynamics of conformations as well [20]. NMR measures the molecules as they are suspended in bulk solution, with the advantage that the molecule-under-test experiences less steric hindrance than a molecule that is bound to a surface and the conformations are as such unperturbed. The chemical shift of a nucleus is measured under influence of a strong magnetic field. It shows great analytical power, but the data is difficult to analyze, it is not suitable for high-throughput screening and it requires a large amount of proteins [21]. A different class of solution techniques are those who capture scattered light from a sample. These techniques do not determine the 3D structure in detail, yet provide an averaged metric of size. Dynamic light scattering can determine conformations by measuring the diffusion constants which are related to the hydrodynamic radius [22], while multi-angle light scattering can measure the mass and the size of a compound by means of the radius of gyration (typically larger than 10 nm [23]). In both light scattering techniques, the shape is approximated by a sphere averaging over all three dimensions. None of these techniques allow for a high throughput however.

While X-ray diffraction and NMR resolve the structure of the biomolecules in a direct way, many techniques first immobilize the biomolecules on a surface, to which a drug ligand can bind and subsequently generate a signal related to the thickness and the density of the adsorbed or bound layer. When the molecules change shape, the thickness and density will change as well. This density is often determined via a related quantity such as refractive index or mass concentration. Traditional **surface techniques** can have difficulties with layers of biomolecules in their native wet environment and more problematically, they lack the resolution to measure layers smaller than 10 nm, which is more than the size of a typical protein. Ellipsometry measures thickness and refractive index at the same time but this is not possible for very thin layers due to fitting difficulties [24]. In this case, the refractive index is usually determined first on a thick layer and subsequently the thickness of the thin layer can be determined. This practice is not applicable to biomolecules however, which only make up a single layer. A new ellipsometric technique tailored for thin layers in wet conditions by use of contrast enhancing surfaces looks promising, but assumptions have to be made on the refractive index of the layer [25]. Quartz crystal microbalance with dissipation monitoring (QCM-D) uses a piezoelectrical transduction to measure the mass of a thin layer of molecules via the quartz resonance frequency and can offer additional information via the dissipation of the energy of the oscillation. In [26], the dissipation of energy was related to changes in the viscoelastic properties which were caused by conformational changes in the bound proteins. As it is a non-optical technique, it allows to measure in non-transparent liquids as well. Atomic force microscopy (AFM) typically measures the topography and thickness of a dry layer but it has

difficulties with kinetic measurements due to long acquisition times, while step measurements can be impractical and prone to uncertainties. Progress has been made by measuring the intermolecular forces instead of the thickness at a higher acquisition rate [27], obtaining kinetic information.

A more recent surface technique that is widely accepted in science is surface plasmon resonance (SPR). It is commercialized by Biacore which delivers a tool for the life science and drug research market and is able to measure reaction affinity, kinetics and concentrations. It is a standard tool in these environments. The biomolecular layers are measured with an evanescent field that decays away from the surface, hence the sensitivity to surface-bound proteins. The evanescent field senses changes in the optical thickness of the layer, which is the product of the refractive index (n) of the layer, scaling with the mass percentage of the protein or the volume density, and the thickness (t) of the layer. This product $t \cdot n$ essentially scales with the deposited mass. This is a crucial point which counts for all evanescent field sensors. They are in essence blind to shape change of the attached molecules, which do only change refractive index or thickness, but not their product, i.e. the total bound mass. They can't tell a thin dense layer from a thick sparse layer. Other evanescent field technologies include reflectometry [28], Mach-Zehnder interferometers [29] or optical cavities [30–32].

Many approaches have been suggested to circumvent this basic physical limitation. Often however, the refractive index is assumed constant, and the signal change is attributed solely to a change in thickness. It is usually assumed that the refractive index of the layer equals a standard refractive index of a dry protein around 1.45, but this is only true in the limit of a perfectly dense monolayer. The refractive index of the adsorbed surface layer can indeed differ a lot from this value, depending amongst others on the conformation of the bound proteins. Neglecting this will manifest itself as an error on thickness. Other integrated surface sensor systems provide information on thickness by growing a large number (>50) of layers and fitting the response of the sensor to simulations in order to obtain the thickness and the refractive index of a single layer. This is done for bilayer systems with Mach-Zehnder interferometers [29] and microrings [33]. This technique is interesting for global trends of the layer system, but cannot elucidate the behavior of a single molecular binding layer, since an averaging over many layers is performed. In general, an additional measurement is required in order to solve for the thickness and the refractive index, as opposed to solving for the optical thickness. In [34] a surface plasmon resonance (SPR) technique generates these extra measurements by exciting the cavity with three wavelengths simultaneously. This way, multiple signals are obtained which all relate to the optical thickness, such that the thickness and refractive index can be disentangled. The

downside of this technique is that by interrogating the layer with different wavelengths, the measured absolute characteristics of the molecular layer are prone to dispersive effects, introducing uncertainties. An excellent approach was offered however by the now defunct Farfield Ltd. Their dual polarization interferometry technique uses two different optical modes in a slab waveguide, which was picked up by the research community for conformational analysis of a.o. proteins, aptamers and DNA [35–37]. Unfortunately, this technique was lacking multiplexing capabilities so as to be integrated in a high-throughput research environment such as drug research.

This overview of technologies which can analyze the conformational aspects of a protein-ligand binding event shows that there is indeed a lack of tools which are fit for drug research. We can sum up the necessary requirements as:

- **High throughput**
In order to integrate in the research flow of pharmaceutical industry, a high-throughput tool is necessary. This excludes the use of bulk solution techniques (with exceptions).
- **Analysis in a native wet environment**
To reduce diverging from a biological situation, the transport of fluids containing the analytes should be as easy as possible. Preferably the analysis tool is non-restrictive to various types of solvents or body fluids.
- **High contrast relative to the substrate**
A typical protein has a size of a few nanometers, while small peptides or ligands are typically smaller. So a surface technique must generate resolvable results for layers which are less than 10 nm thick.
- **High spatial resolution**
In the sub-10 nm range, small conformation changes must be detectable. A spatial resolution of a few Å is desired.
- **High temporal resolution**
Although switching between conformational sub-states can occur on time scales as short as picoseconds, larger global conformational changes and general unfolding occur in milliseconds to seconds [38].
- **Ease-of-use**
The number of preparatory steps should be reduced to a minimum as should the complexity of the data analysis still required by the end-user. When highly-trained personnel is needed (as for NMR) to conduct and interpret the experiment, this increases the cost of the overall experiment. The maintenance that has to be done to the tool should be kept to a minimum as well.

In the best case, consumables are used, avoiding the need for regenerating the sensing surface.

1.4 Integrated Silicon Photonics

One approach to reach these requirements is by using the merits of silicon photonics. Today, almost every small or big company in optical communications is dealing with silicon photonics in one way or another. This huge popularity can be attributed to the relocating of computation and data storage to the cloud [39]. To illustrate, Facebook has recently built a third data center in Iowa which occupies about 10 hectares [40]. This can be regarded as a supercomputer where all the data is stored, but where also major computations need to be done in order to answer to the requests which are done by a Facebook user. To allow this data to be searched, processed and communicated, data needs to be send back and forth through these enormous football-fields-spanning data centers. This is not just done by Facebook, but many enterprises outsource their computations to the clouds. Electrical cables can't provide the data rates needed within such a data center and hence optical communication is needed. These have higher bandwidths, can send data over longer distances and require less energy than electrical wires. This is no longer the conventional type of long-distance optical communication as it was started for transatlantic optical communications, but small distances, where many optical transceiver components are needed. This high demand for fast optical components to keep the clouds running is a big driver for the photonics industry. To keep on increasing these data rates, the role of the electrical signal is decreasing. Up until very recently, the division was clear: data was processed by electrical chips and transmitted and received by optical chips. In May 2015, IBM launched the first fully integrated monolithic chip which combines electrical and optical functionalities [41]. Other major companies which push forwards the silicon photonics chip technology are the likes of Intel, Luxtera and Hamamatsu Photonics. Indeed, these are often companies who were producing electronic CMOS chips which are now spending big budgets on silicon photonics research. This is not a coincidence: silicon is also the material of chose in consumer electronics and hence there is a huge economical benefit to push photonics on silicon. All the manufacturing mass-production tools can be re-used partially, completely, or at least be reconfigured to produce silicon photonics chips instead of silicon electronic chips. These silicon photonics chips are not restricted to telecommunications however: they can be used as well for biomolecular sensing with the benefit that a single silicon sensing chip, when mass produced, costs about 1 euro. From a user point-of-view, these chips can be considered a consumable. No regeneration or cleaning procedures have to be applied, simplifying and speeding up the measurements. Not just the cost, but also the quality of the optical circuits which we will use for sensing is thus

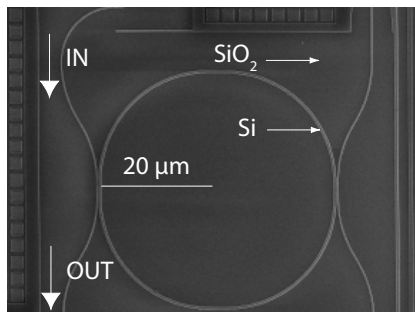


Figure 1.2: SEM image of a microring resonator in the SOI platform.

very high compared to other material systems that do not enjoy this huge research and industrial push.

The material system of such an optical chip is silicon-on-insulator (SOI) and a sensing chip uses the most simple form of such a chip: a collection of passive waveguides which can be seen as wires that confine and guide the light. The actual sensing component which we will use is a microring resonator, which is nothing more than a waveguide which is routed in a closed circle [31, 32], as illustrated on Figure 1.2. In these microrings, only light is allowed to circulate whose wavelength fits an integer number of times in the ring. However, a small portion of the light leaks out of the waveguide, on the contrary to electrical current in a copper wire, and decays exponentially away from the surface. This fraction is called the evanescent tail of the waveguide mode and it probes whatever is on top of the ring surface. On this surface, capturing molecules are attached which only bind to the molecules we want to detect or research, illustrated in Figure 1.3(b). Because of the evanescent field, the specific wavelength which fits in the ring is sensitive to the binding of molecules on top of this ring. Therefore, whenever a binding event takes place, the resonance wavelength shifts and this shift is measured and further analyzed, see Figure 1.3(c).

In order to transport the molecules to the surface of the sensor, the chip is integrated with microfluidics. This comprises a wide scale of technologies which offer various fluidic functionalities on a micrometer-scale. In its simplest form, a fluidic cell is fabricated which contains micrometer-size channels. By bonding this cell on top of the silicon chip, the channels can be interfaced to the user by means of simple tubing. This allows the easy streaming of DNA, proteins, polymers, small ligands, etc. over the sensor surface. However, microfluidics can also offer more complicated steps like filtering unwanted biological debris out of a complex matrix such as serum, urine or sputum, before it is transported to the

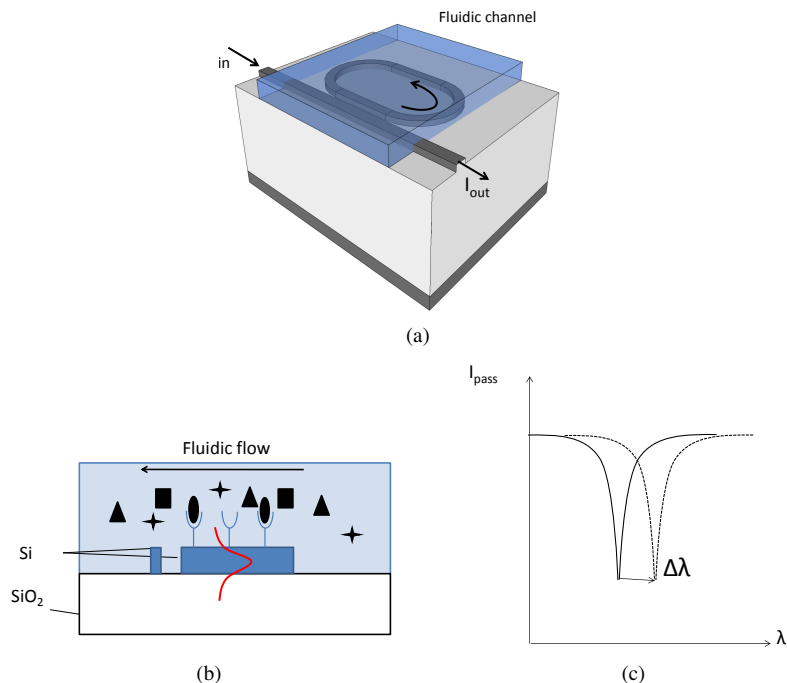


Figure 1.3: (a) Illustration of the microring with fluidic channel on top as an angled perspective view and (b) as a cross section that shows the receptor molecules on top of the ring. (c) Spectrum of the output of the access waveguide, showing the resonance dip and the shift in wavelength due to a binding event.

microring sensors. Micro-meter sized reaction chambers with integrated heating can be manufactured, as well as mixing containers where two or more fluids can be mixed together in a passive way. Combining these functions of sample preparation, sample handling and detection on a single centimeter-sized component truly has the potential of reducing a complete biological lab onto a single chip, hence the aptly coined term lab-on-a-chip. Therefore, it comes as no surprise that many companies are attempting to offer a tabletop or point-of-care analysis tool which can perform DNA or protein analysis in under an hour. These are for example Philips, Roche, Alere, Cepheid, Mycartis, Iqum or Biocartis.

The economical pull of the CMOS industry is not the only reason why we do sensing with silicon photonics. One exceptional feature of the SOI material system is the extremely high index contrast between the silicon, which guides the light, and the silicon dioxide substrate, on which these waveguides lie. This high contrast confines the light so well, that these rings can be made with a radius of only

5-20 μm , paving the way for extremely high-multiplexing systems. Recently, 128 ring resonators have been stacked in a matrix, integrated with microfluidics and read out simultaneously [30]. With advanced biological spotting techniques, every ring can be made receptive to a different biomarker, thus creating a very performant bio-assay. A second advantage of this high index contrast is that the evanescent tail of the resonating mode in the microring is only sensitive to 60 nm above the surface. This evanescent field is the sensing mechanism and the more of this evanescent field is filled up by the molecular layer, the more sensitive an evanescent field technique is. For comparison, an SPR sensor has an evanescent tail of a few hundreds of nanometers [33]. Detection limits of this microring platform are ranging from 0.3 pg/mm^2 to 3 pg/mm^2 .

1.5 Dual Polarization Microring

A microring resonator fabricated in SOI suffers from the same drawback as all evanescent field sensing techniques, as noted above, namely that it is sensitive to the optical thickness and blind to conformational changes. However, we will describe a method to obtain information on the contextual conformation of biomolecules, by simultaneously determining the thickness and the refractive index of a biolayer. To track both t and n , the microring sensor is excited by two optical modes simultaneously such that we obtain a two-equation system for these two independent variables, as opposed to the single equation we obtain by using only one mode. This sensor is able to sense small changes in thickness and density of a layer which has a thickness smaller than 10 nm and can do so in its native wet regime. Combining this with the ease-of-use of the microfluidics, the multiplexing abilities of the microring actuator and the low cost of the silicon platform, a tool with excellent capabilities for the pharmaceutical industry is proposed.

To put this sensor in perspective, it can be compared to the standard technique to study thin layers: ellipsometry. From a physics standpoint, both tools show similarities, in the sense that ellipsometry also determines t and n by tracking two separate signals. In the case of ellipsometry, this is done by tracking the change in the phase (Δ) and the amplitude (Ψ) of the ratio of reflection coefficients of two orthogonally polarized beams. However, it is shown in [42] that it is impossible to determine t and n simultaneously of a layer which is much smaller than the interrogation wavelength (thin film approximation). In this case, the change in Ψ can no longer be detected and only one signal remains: the change in phase. This is insufficient to determine two independent parameters simultaneously and thus an assumption is usually made on the refractive index in order to determine the thickness [24]. It is also shown [42] that it is not possible to generate more inde-

pendent data for very thin films by using many wavelengths as in spectroscopic ellipsometry, since the signals are highly coupled. Many experimental studies have confirmed ellipsometry's lower limit on the resolvable thickness of a layer, including for the more advanced contrast-boosting in-situ null ellipsometry, with reported values around 10 nm [43–46].

In contrast, the dual polarization microring technique has a resolution lower than 0.1 nm on thickness for layers which are over 2 nm thick and only has relative errors over 10%, for layers which are thinner than 0.75 nm. Although going down from 10 nm to 0.75 nm as minimum layer thickness which can be faithfully detected seems like a small improvement, it opens up new fields of applications which were difficult to reach before. Primarily, it allows to study the natural dynamics of molecular-size systems in a fast and easy way, which we will explore over the course of this thesis.

1.6 Publications

1.6.1 Patent applications

1. P. Bienstman, T. Claes, K. De Vos, J.-W. Hoste, W. Bogaerts, *Methods and systems for biosensing* US 2012/0296604 A1

1.6.2 Publications in international journals

1. J.-W. Hoste, P. Soetaert, and P. Bienstman, Improving the detection limit of conformational analysis by utilizing a dual polarization Vernier cascade, *Optics Express*, under review.
2. J.-W. Hoste, Bruno G. De Geest, and P. Bienstman, Analysis of the interface layers of an adsorbed polyelectrolyte stack by an integrated photonic dual polarization technique, *Analytical and Bioanalytical Chemistry*, under review.
3. J.-W. Hoste, S. Werquin, T. Claes, and P. Bienstman, Conformational analysis of proteins with a dual polarisation silicon microring, *Optics Express*, 22(3), pp. 2807-2820 (2014).

1.6.3 Publications in international conferences

1. D. Delbeke, A. Subramanian, P. Cardile, W. Woestenborghs, A. Ruocco, J.-W. Hoste, D. Martens, A. Dhakal, P. Bienstman, G. Roelkens, N. Le Thomas, R. Baets, "Silicon photonics for on-chip spectrophotometry", Group IV photonics, United States, 2015.

2. J.-W. Hoste, B.G. De Geest, P. Bienstman, "Determination of thickness and density of a wet multilayer polymer system with sub-nanometer resolution by means of a dual polarization silicon-on-insulator microring", SPIE Photonics West, United States, 93370E-1-93370E-7, 2015.
3. C. Lerma Arce, E. Hallynck, S. Werquin, J.W. Hoste, D. Martens, "Silicon photonics biosensing : different packaging platforms and applications", SPIE Photonics West, 9320, United States, 932006-1-932006-6, 2015.
4. J.W. Hoste, Bruno G. De Geest, P. Bienstman, "Employing a Dual Polarisation Microring to Determine Refractive Index and Thickness of a Thin Polymer Layer", 16th International Conference on Transparent Optical Networks (ICTON 2014), Austria, Mo.C5.4.1-Mo.C5.4.4, 2014.
5. J.W. Hoste, S. Werquin, P. Bienstman, "Employing dual polarisation biosensing to study the conformational behaviour of BSA molecules during the adsorption to a silicon microring", EUROPT(R)ODE X11 Conference on optical Chemical Sensors & Biosensors, Greece, 2014.
6. J.F.I.B Hoste, S. Werquin, P. Bienstman, "Dual polarisation biosensing with an SOI microring", Proceedings of the 18th Annual Symposium of the IEEE Photonics Society Benelux Chapter, Netherlands, 113-116, 2013.
7. J.W. Hoste, T. Claes, P. Bienstman, "Using dual polarization silicon ring resonators to monitor pH-induced conformational changes in BSA molecules", European Congress and Exhibition on Advanced Materials and Processes (EUROMAT 2013), Spain, 2013.
8. P. Bienstman, S. Werquin, C. Lerma Arce, E. Hallynck, T. Claes, J.W. Hoste, D. Martens, "Silicon nanophotonics on-chip sensing", Progress In Electromagnetics Research Symposium (PIERS 2013), Sweden, 1032, 2013.
9. P. Bienstman, S. Werquin, C. Lerma Arce, D. Witters, R. Puers, J. Lammer-tyn, T. Claes, E. Hallynck, J.W. Hoste, D. Martens, "Nanophotonic biosensors in silicon-on-insulator", The 17th International Conference on Solid-State Sensors, Actuators and Microsystems (Transducers 2013), Spain, 2588-2591, 2013.
10. P. Bienstman, S. Werquin, C. Lerma Arce, D. Witters, R. Puers, J. Lammer-tyn, T. Claes, E. Hallynck, J.W. Hoste, D. Martens, "Ring resonator based SOI biosensors", 2013 Photonics West Conference, 8629, United States, 8629-8641, 2013.

References

- [1] U.S. Department of Health, Human Services: Food, and Drug Administration. *Is it true FDA is approving fewer drugs lately?* <http://www.fda.gov/AboutFDA/Transparency/Basics/ucm247348.htm>, 2011.
- [2] Tufts center for the study of drug development. *Tufts CSDD 2014 Cost Study*. http://csdd.tufts.edu/news/complete_story/pr_tufts_csdd_2014_cost_study, 2014.
- [3] FDA. *Novel new drugs 2014 summary*. <http://www.fda.gov/downloads/Drugs/DevelopmentApprovalProcess/DrugInnovation/UCM430299.pdf>, 2015.
- [4] Thomson Reuters Deloitte. *Measuring the return from pharmaceutical innovation 2013. Weathering the storm?* <http://www2.deloitte.com/content/dam/Deloitte/uk/Documents/life-sciences-health-care>, 2013.
- [5] EvaluatePharma. *Budget-Busters: The Shift to High-Priced Innovator Drugs in the USA*. <http://info.evaluategroup.com/usa-svp-lp-ep.html>, 2013.
- [6] U.S. Food and Drug Administration. *Innovation or stagnation: Challenge and opportunity on the critical path to new medical products*. <http://www.fda.gov/ScienceResearch/SpecialTopics/CriticalPathInitiative/default.htm>, 2004.
- [7] Patrick R. Connelly, T. Minh Vuong, and Mark A. Murcko. *Getting physical to fix pharma*. *Nat. Chem.*, 3(9):692–695, September 2011.
- [8] E Reynaud. *Protein Misfolding and Degenerative Diseases*. *Nature Education*, 3(9), 2010.
- [9] R. Bryn Fenwick, Santi Esteban-Martin, and Xavier Salvatella. *Understanding biomolecular motion, recognition, and allostery by use of conformational ensembles*. *Eur. Biophys. J.*, 40:1339–1355, 2011.
- [10] Nikos S Hatzakis. *Single molecule insights on conformational selection and induced fit mechanism*. *Biophys. Chem.*, 186:46–54, February 2014.
- [11] Matthias Rabiller, Matthäus Getlik, Sabine Klüter, André Richters, Sandra Tückmantel, Jeffrey R Simard, and Daniel Rauh. *Proteus in the world of proteins: conformational changes in protein kinases*. *Archiv der Pharmazie*, 343(4):193–206, 2010.

- [12] Georgia Hatzivassiliou, Kyung Song, Ivana Yen, Barbara J Brandhuber, Daniel J Anderson, Ryan Alvarado, Mary J C Ludlam, David Stokoe, Susan L Gloor, Guy Vigers, Tony Morales, Ignacio Aliagas, Bonnie Liu, Steve Sideris, Klaus P Hoefflich, Bijay S Jaiswal, Somasekar Seshagiri, Hartmut Koeppen, Marcia Belvin, Lori S Friedman, and Shiva Malek. *RAF inhibitors prime wild-type RAF to activate the MAPK pathway and enhance growth*. *Nature*, 464(7287):431–5, March 2010.
- [13] K.J Gregory, E. N. Dong, J. Meiler, and P. J. Conn. *Allosteric Modulation of Metabotropic Glutamate Receptors: Structural Insights and Therapeutic Potential*. *Neuropharmacology*, 60(1):66–81, 2012.
- [14] Patrick Dorr, Mike Westby, Susan Dobbs, Paul Griffin, Becky Irvine, Malcolm Macartney, Julie Mori, Graham Rickett, Caroline Smith-burchnell, Carolyn Napier, Rob Webster, Duncan Armour, David Price, Blanda Stammen, Anthony Wood, and Manos Perros. *Maraviroc (UK-427 , 857), a Potent , Orally Bioavailable , and Selective Small-Molecule Inhibitor of Chemokine Receptor CCR5 with Broad-Spectrum Anti-Human Immunodeficiency Virus Type 1 Activity*. 49(11):4721–4732, 2005.
- [15] Peter Fechner, Oliver Bleher, Melanie Ewald, Kathrin Freudenberger, Dominik Furin, Urs Hilbig, Felix Kolarov, Katrin Krieg, Lothar Leidner, Goran Markovic, Günther Proll, Florian Pröll, Sabrina Rau, Johannes Riedt, Barbara Schwarz, Patricia Weber, and Julia Widmaier. *Size does matter! Label-free detection of small molecule-protein interaction*. *Analytical and bioanalytical chemistry*, 406(17):4033–51, July 2014.
- [16] Eckenrode Virginia K. Ward William W. Prendergast Frank G. Cormier Milton J. Prasher, Douglas C. *Primary structure of the Aequorea victoria green-fluorescent protein*. *Gene*, 111:229–233, 1992.
- [17] Martin J Lohse, Susanne Nuber, and Carsten Hoffmann. *Fluorescence / Bioluminescence Resonance Energy Transfer Techniques to Study G-Protein-Coupled*. 64(2):299–336, 2012.
- [18] Protein data bank. *PDB current holdings breakdown*. <http://www.rcsb.org/pdb/statistics/holdings.do>, 2015.
- [19] Nathalie Goudreau, Christopher T Lemke, Anne-marie Faucher, Chantal Grand-maître, Sylvie Goulet, Jean-eric Lacoste, Jean Rancourt, Eric Malenfant, Jean-franc Mercier, Steve Titolo, and Stephen W Mason. *Novel Inhibitor Binding Site Discovery on HIV1 Capsid NTerminal Domain by NMR and Xray Crystallography*. *ACS Chem. Biol.*, pages 1074–1082, 2013.

- [20] David D Boehr, H Jane Dyson, and Peter E Wright. *An NMR Perspective on Enzyme Dynamics*. Chem. Rev. (Washington, DC, U. S.), 106(8):3055–3079, 2006.
- [21] Maurizio Pellecchia, Ivano Bertini, David Cowburn, Claudio Dalvit, Ernest Giralt, Wolfgang Jahnke, Thomas L. James, Horst Kessler, Claudio Luchinat, Bernd Meyer, Hartmut Oschkinat, Jeff Peng, Harald Schwalbe, and Gregg Siegal. *Perspectives on NMR in drug discovery : a technique comes of age*. Nat. Rev. Drug Discovery, 7(9):738–745, 2008.
- [22] Daniel Some. *Light-scattering-based analysis of biomolecular interactions*. Biophys. Rev., 5(2):147–158, June 2013.
- [23] Wyatt. *Multi-Angle Light Scattering Detectors*. <http://www.wyatt.eu/index.php?id=mals-detectors&L=0%22%20onfocus%3D%22blurLink%28this%29,2014>.
- [24] John E Wong, Florian Rehfeldt, Peter Ha, Motomu Tanaka, and Regine Klitzing. *Swelling Behavior of Polyelectrolyte Multilayers in Saturated Water Vapor*. Macromolecules, 32:7285–7289, 2004.
- [25] Amandine M. C. Egea, Melinda Metivier, Philippe Croguennoc, Magali Remaud-Simeon, and Christophe Vieu. *Real-Time Monitoring of Dextranucrase-Based Enzymatic Reaction Through Surface-Enhanced Ellipsometric Contrast (SEEC) Microscopy in Liquid Environment*. Bio-NanoScience, 4(1):37–45, November 2013.
- [26] Erik Nileback, Fredrik Westberg, Johanna Deinum, and Sofia Svedhem. *Viscoelastic Sensing of Conformational Changes in Plasminogen Induced upon Binding of Low Molecular Weight Compounds*. Anal. Chem., 82(20):8374–8376, 2010.
- [27] Toshiaki Mori, Megumi Asakura, and Yoshio Okahata. *Single-Molecule Force Spectroscopy for Studying Kinetics of Enzymatic Dextran Elongations*. J. Am. Chem. Soc., pages 5701–5703, 2011.
- [28] Florian Pröll, Bernd Möhrle, Michael Kumpf, and Günter Gauglitz. *Label-free characterisation of oligonucleotide hybridisation using reflectometric interference spectroscopy*. Anal. Bioanal. Chem., 382(8):1889–1894, August 2005.
- [29] Eva Melnik, Paul Müllner, Roman Bruck, Michael Lämmerhofer, and Rainer Hainberger. *Biofilm Growth Monitoring on a-Si : H Based Mach-Zehnder Interferometric Biosensors*. In Optical Sensors.

- [30] S. Janz, D. Xu, M. Vachon, N. Sabourin, P. Cheben, H. McIntosh, H. Ding, S. Wang, J. H. Schmid, A. Del age, J. Lapointe, A. Densmore, R. Ma, W. Sinclair, S. M. Logan, R. Mackenzie, Q. Y. Liu, D. Zhang, G. Lopinski, O. Mozenon, M. Gilmour, and H. Tabor. *Photonic wire biosensor microarray chip and instrumentation with application to serotyping of Escherichia coli isolates*. Opt. Express, 21(4):4623–4637, 2013.
- [31] Muzammil Iqbal, Martin A Gleeson, Bradley Spaugh, Frank Tybor, William G Gunn, Michael Hochberg, Tom Baehr-jones, Ryan C Bailey, and L Cary Gunn. *Label-Free Biosensor Arrays Based on Silicon Scanning Instrumentation*. IEEE Journal of Selected Topics in Quantum Electronics, 16(3):654–661, 2010.
- [32] K. De Vos, J. Girones, T. Claes, Y. De Koninck, S. Popelka, E. Schacht, R. Baets, and P. Bienstman. *Multiplexed Antibody Detection With an Array of Silicon-on-Insulator Microring Resonators*. IEEE Photonics Journal, 1(4):225–235, October 2009.
- [33] Matthew S Luchansky, Adam L Washburn, Teresa A. Martin, Muzammil Iqbal, L Cary Gunn, and Ryan C Bailey. *Characterization of the evanescent field profile and bound mass sensitivity of a label-free silicon photonic microring resonator biosensing platform*. Biosens. Bioelectron., 26(4):1283–1291, 2010.
- [34] Pavel Adam, Jakub Dost alek, and Ji  Homola. *Multiple surface plasmon spectroscopy for study of biomolecular systems*. Sens. Actuators, B, 113(2):774–781, February 2006.
- [35] Kristin E D Coan, Marcus J Swann, and Johannes Ottl. *Measurement and differentiation of ligand-induced calmodulin conformations by dual polarization interferometry*. Analytical chemistry, 84(3):1586–91, February 2012.
- [36] Veli Cengiz Ozalp. *Dual-polarization interferometry for quantification of small molecules using aptamers*. Analytical and bioanalytical chemistry, 402(2):799–804, January 2012.
- [37] B. Lillis, M. Manning, H. Berney, E. Hurley, A. Mathewson, and M. M. Sheehan. *Dual polarisation interferometry characterisation of DNA immobilisation and hybridisation detection on a silanised support*. Biosens. Bioelectron., 21(8):1459–1467, February 2006.
- [38] Heather A. Carlson. *Protein flexibility and drug design : how to hit a moving target*. Current opinion in chemical biology, 6:447–452, 2002.

- [39] Yurii A. Vlasov. *Yurii A. Vlasov plenary presentation on silicon integrated nanophotonics at SPIE Photonics West 2015*. <http://spie.org/x112677.xml>, 2015.
- [40] Data Center Knowledge. *Facebook to build third data center in Iowa*. <http://www.datacenterknowledge.com/archives/2015/06/04/third-facebook-data-center-coming-to-iowa/>.
- [41] IBM. *IBMs Silicon Photonics Technology Ready to Speed up Cloud and Big Data Applications*. <http://www-03.ibm.com/press/us/en/pressrelease/46839.wss>, 2015.
- [42] R Reiter, H Motschmann, H Orendi, A Nemetz, and W Knoll. *Ellipsometric Microscopy . Imaging Monomolecular Surfactant Layers at the Air-Water Interface*. *Langmuir*, (8):1784–1788, 1992.
- [43] Jagoba J. Iturri Ramos, Stefan Stahl, Ralf P. Richter, and Sergio E. Moya. *Water Content and Buildup of Poly(diallyldimethylammonium chloride)/Poly(sodium 4-styrenesulfonate) and Poly(allylamine hydrochloride)/Poly(sodium 4-styrenesulfonate) Polyelectrolyte Multilayers Studied by an in Situ Combination of a Quartz Crystal Microb*. *Macromolecules*, 43(21):9063–9070, November 2010.
- [44] Peter Nestler, Stephan Block, and Christiane A Helm. *Temperature-Induced Transition from Odd-Even to Even-Odd Effect in Polyelectrolyte Multilayers Due to Interpolyelectrolyte Interactions*. *J Phys Chem A*, 116:1234–1243, 2012.
- [45] Fredrik Tiberg and Mikael Landgren. *Characterization of Thin Nonionic Surfactant Films at the Silica / Water Interface by Means of Ellipsometry*. *Langmuir*, 9:927–932, 1993.
- [46] J Ruths, F Essler, G Decher, and H Riegler. *Polyelectrolytes I : Polyanion / Polycation Multilayers at the Air / Monolayer / Water Interface as Elements for Quantitative Polymer Adsorption Studies and Preparation of Hetero-superlattices on Solid Surfaces*. *Langmuir*, 37(4):8871–8878, 2000.

2

Components of a conformational biosensor

2.1 Introduction

The aim of this research work is to retrieve more information on a layer of molecules by interrogating them not with one, but with two different optical modes simultaneously in an optical cavity. This will allow us to measure the thickness and the refractive index of a molecular layer. The two optical modes which we will use are called a transversal electric (TE) and a transversal magnetic (TM) mode. But before we discuss the molecular layers and the kind of experiments we can perform on them, we need to go through the physics theory that enables us to perform these kind of experiments. What is a mode exactly and what causes these modes to be clearly separated in a TE and TM state? Once we know what a mode is, we need to know how to get these modes in an optical cavity and how this cavity will help us to learn more about molecular layers. With this knowledge, we can proceed towards the practical nature of things and look at what the obstacles are that stand in between performing a biomolecular sensing experiment and the design of an optical cavity. A typical biosensing experiment is exemplified by discussing the detection of protein specific antigen. Finally, we will shortly discuss how to interpret the refractive index of a molecular layer, as measured by a dual polarization biosensor.

2.2 Waveguides and their separation in modes

The question where modes, and more specifically the separation in TE and TM modes, come from can be answered in various ways: from a more mathematical utilitarian perspective, which is the standard way in textbooks approaching optics from an engineering perspective, or from general symmetry statements which stem from a more fundamental physics perspective. Of course, both are valid and we will briefly explore them to gain insight in this matter.

Whichever way we chose to approach this, the starting point is identical: the four Maxwell equations which dictate *all* the properties of electromagnetic waves and their interaction with matter. We will cast Maxwell's equations in a form which make sense for the passive waveguide systems we will study. In this form we will work with the following fields: the electric field \mathbf{E} and the magnetic field \mathbf{H} . The material and its response to these fields is represented by the permeability $\mu_0\mu_r(\mathbf{r}, t)$ and the permittivity $\epsilon_0\epsilon_r(\mathbf{r}, t)$. The permeability is the response to the magnetic field and the permittivity is the response to the electric field. We also make the following assumptions:

- **non-magnetic materials**

We will treat only materials where $\mu_r(\mathbf{r}, t) = 1$, as is the case for most materials in nature. This means there is no direct magnetic response, other than the fundamental response in vacuum.

- **no sources of energy**

In the most general form of Maxwell's equations, there is an electric charge density ρ at the right-hand side of equation 2.3 and an electric current density vector \mathbf{J} at the right-hand side of equation 2.2. When there are no sources present these are set to zero. Remark that we will obtain nonzero solutions of these equations, even though there are no sources to drive these! The study of these equations are hence relevant for all forms of communication studying the propagation and transmission of these fields. These fields propagate as waves in media without sources.

- **mixed isotropic dielectric linear medium**

The material system is a composite of different materials which are linear, homogeneous and isotropic and which do not change with time. This means that the relative permittivity $\epsilon_r(\mathbf{r})$ is a scalar which depends only on the position. In every medium the permittivity can hence be different, but in a specific medium, it behaves isotropically. As such, the material does not differentiate between waves under a different angle. The fact that it is linear means that the material does not change its response depending on the strength of the fields.

The equations take the following form:

$$\nabla \times \mathbf{E}(\mathbf{r}, t) + \mu_0 \frac{\partial \mathbf{H}(\mathbf{r}, t)}{\partial t} = 0 \quad (2.1)$$

$$\nabla \times \mathbf{H}(\mathbf{r}, t) - \epsilon_0 \epsilon_r(\mathbf{r}) \frac{\partial \mathbf{E}(\mathbf{r}, t)}{\partial t} = 0 \quad (2.2)$$

$$\nabla \cdot [\epsilon_r(\mathbf{r}) \mathbf{E}(\mathbf{r}, t)] = 0 \quad (2.3)$$

$$\nabla \cdot \mathbf{H}(\mathbf{r}, t) = 0 \quad (2.4)$$

The components we use for sensing are made out of waveguides which are functionally very simple structures: they do nothing more than guiding the light. To find out in what way the light is guided in these waveguides, all we need to do is solve these equations in the mixed dielectric medium that is a waveguide. However, by closely inspecting these equations we can pre-organize the solutions. These equations are linear and hence we can separate the time dependence from the space dependence. Furthermore we consider monochromatic harmonic waves, which are waves with a single frequency:

$$\mathbf{E}(\mathbf{r}, t) = \mathbf{E}(\mathbf{r}) e^{i\omega t} \quad (2.5)$$

$$\mathbf{H}(\mathbf{r}, t) = \mathbf{H}(\mathbf{r}) e^{i\omega t} \quad (2.6)$$

It seems rather blunt to reduce the complete complexity of Maxwell's equations into a time dependence so strict as a harmonic sinusoidal wave. However, Fourier analysis tells us that any time dependence can be written as a suitable linear combinations of these harmonic modes. And since Maxwell's equations are linear, if two solutions are found, then any linear combination of these solutions is *also* a solution. Hence we can construct complex functions in time and space using this decomposition. The spatial patterns $\mathbf{E}(\mathbf{r})$ and $\mathbf{H}(\mathbf{r})$ are called the modes of the system. An optical mode is thus a solution of Maxwell's equations in a specific material geometry represented by the permittivity (and permeability) functions. Inserting these monochromatic fields in the two curl equations 2.1 and 2.2, we obtain:

$$\nabla \times \mathbf{E}(\mathbf{r}) + i\omega \mu_0 \mathbf{H}(\mathbf{r}) = 0 \quad (2.7)$$

$$\nabla \times \mathbf{H}(\mathbf{r}) - i\omega \epsilon_0 \epsilon_r(\mathbf{r}) \mathbf{E}(\mathbf{r}) = 0 \quad (2.8)$$

In optics, the relative permittivity is usually addressed via the equivalent refractive index n , where

$$n^2 = \epsilon_r \quad (2.9)$$

Focusing on obtaining the modes for a waveguide system we face the problem of continuity. Maxwell's equations demand that the fields are differentiable, hence

they must be continuous in the respective dielectric parts of the waveguide. However, moving from one dielectric to the next, for instance from the waveguide core to the waveguide cladding, means the permittivity changes abruptly, for which it is not directly apparent how the fields should respond. Luckily, there is a set of boundary conditions which can be applied to the electromagnetic field which dictates exactly this. These conditions do not appear out of thin air however, they can be readily obtained by applying Gauss' divergence theorem and Stokes' theorem on the four Maxwell equations. More details can be found in [1]. For a waveguide we obtain:

$$\mathbf{E}_{\parallel,1} = \mathbf{E}_{\parallel,2} \quad (2.10)$$

$$\epsilon_1 \mathbf{E}_{\perp,1} = \epsilon_2 \mathbf{E}_{\perp,2} \quad (2.11)$$

$$\mathbf{H}_{\parallel,1} = \mathbf{H}_{\parallel,2} \quad (2.12)$$

$$\mathbf{H}_{\perp,1} = \mathbf{H}_{\perp,2} \quad (2.13)$$

These state that the tangential part of the electric field vector remains continuous going from one dielectric to the next, while the normal component experiences a discontinuous jump. In practice this means that when we move from the core of a waveguide to the cladding, the normal component of the electric field will increase abruptly, since the core material always has a higher permittivity than the cladding (in the case of index guiding).

Before we solve these, we can pre-organize the fields once more. The nature of the waveguides we study is that they guide the fields along one direction. This is the propagation direction of the fields and we chose this direction to be the z -direction. This allows us to drag the z -dependency of the fields out of $\mathbf{E}(\mathbf{r})$ and $\mathbf{H}(\mathbf{r})$:

$$\mathbf{E}(\mathbf{r}, t) = \mathbf{E}(x, y) e^{i(\omega t - \beta z)} \quad (2.14)$$

$$\mathbf{H}(\mathbf{r}, t) = \mathbf{H}(x, y) e^{i(\omega t - \beta z)} \quad (2.15)$$

Here β is the propagation constant. This looks like a rather arbitrary decision. However we can see that at one specific time at one specific z -coordinate, the fields have a certain phase. This specific phase now moves in z -direction with a speed equaling the phase velocity ω/β , while the mode profile $\mathbf{E}(x, y)$ does not change. Hence the name propagation constant. The next section on symmetries explains this in a more fundamental way however. Inserting these two fields in the

two curl equations 2.7 and 2.8 provides the following set of equations:

$$\left\{ \begin{array}{l} \frac{\partial E_z}{\partial y} + i\beta E_y = -i\omega\mu_0 H_x \\ -i\beta E_x - \frac{\partial E_z}{\partial x} = -i\omega\mu_0 H_y \\ \frac{\partial E_y}{\partial x} - \frac{\partial E_x}{\partial y} = -i\omega\mu_0 H_z \\ \frac{\partial H_z}{\partial y} + i\beta H_y = i\omega\epsilon_0 n^2(\mathbf{r}) E_x \\ -i\beta H_x - \frac{\partial H_z}{\partial x} = i\omega\epsilon_0 n^2(\mathbf{r}) E_y \\ \frac{\partial H_y}{\partial x} - \frac{\partial H_x}{\partial y} = i\omega\epsilon_0 n^2(\mathbf{r}) E_z \end{array} \right. \quad (2.16)$$

We proceed by solving these equations for the most simple waveguide profile, a slab waveguide, as depicted on Figure 2.1. This waveguide is in essence a 2D-structure, it has no y-dependency. Actually, it also has no z-dependency, it is only non-uniform in the x-direction, but we arbitrarily chose the z-direction to be the propagation direction. This boils down mathematically to setting all the y-derivatives to 0. Doing this breaks these 6 equations down to two decoupled sets of 3 equations. The first set of equations only has field components E_y , H_x and H_z . The solutions to this set are called transverse electric modes (TE modes), since the electric field is tangential to the propagation direction. The second set has field components H_y , E_x and E_z . Solutions to this set are called transverse magnetic mode (TM mode), since the magnetic field lies in the plane perpendicular to the propagation direction. For the TE modes we obtain from the set of equations 2.16 the following wave equation for E_y :

$$\frac{d^2 E_y}{dx^2} + (\omega^2 \mu_0 \epsilon_0 n^2(x) - \beta^2) E_y = 0 \quad (2.17)$$

The components H_x and H_z then follow directly from the solution of E_y . The solution for E_y is found by solving this wave equation in each of the three homogeneous dielectrics that make up the slab waveguide structure. This scalar wave equation can be readily solved by sinusoids or exponentials, depending on the sign of the $(\omega^2 \mu_0 \epsilon_0 n^2(x) - \beta^2)$ term. Since we are looking for *guided* modes of this system, we inhabit the core by a sinusoidal function and choose an exponential function in the cladding material, which decays away from the core. This sets the condition of the propagation constant for a mode to be guided, with the speed of light in vacuum $c = 1/\sqrt{\epsilon_0 \omega_0}$:

$$\beta > \frac{\omega n_{cl,max}}{c} \quad (2.18)$$

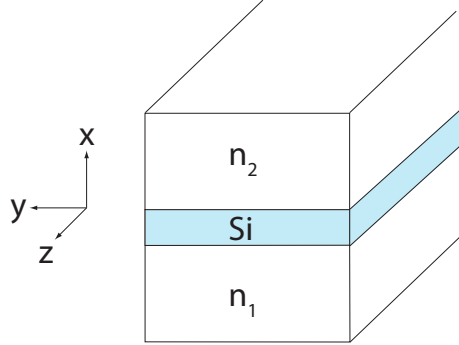


Figure 2.1: Illustration of a slab waveguide with a silicon layer as guiding layer. The refractive indices of the cladding layers above and below the guiding layer must be smaller than the refractive index of silicon. The structure is uniform in the y - and z -direction.

Here, $n_{cl,max}$ is the highest refractive index of the two cladding materials. The three different field profiles are then knitted nicely together by imposing the boundary conditions which match the tangential components of \mathbf{E} and \mathbf{H} across the interfaces. These operations generate an eigenvalue problem for the propagation constant, of which there exists a discrete number of solutions. Each of the solved propagation constants then feeds back and locks the field profiles. For the TM modes, the H_y component takes on a similar role as the E_y component did for the TE modes and dictates the shape of the E_x and E_z components [1, 2].

We note that the defining step to separating the modes in two distinct polarizations, which do not couple since they do not share any field vector components, is given by the uniformity of the structure in a transverse direction. However, if we move towards more practical waveguide structures, such as the wire waveguide depicted on Figure 2.2, which we will use throughout this thesis, then it is obvious this uniformity no longer holds. Yet, simulations with a 2D-mode solver such as Fimmwave, shows that the first two modes of these structures have a distinct TE-like or TM-like profile. Numerically, the first mode in a typical SOI waveguide with a cross section with a width of 450 nm and a height of 220 nm has a TE-fraction of 98 %, while the second mode has a TE-fraction of 3 %. This is the reason why these modes are often called quasi-TE or TE-like and quasi-TM or TM-like. We conclude that the technical-mathematical way of unfolding these two sets does not satisfy completely.

A more physical underlying principle regarding this separation is found via symmetry considerations, of which the concepts are largely described in the excel-

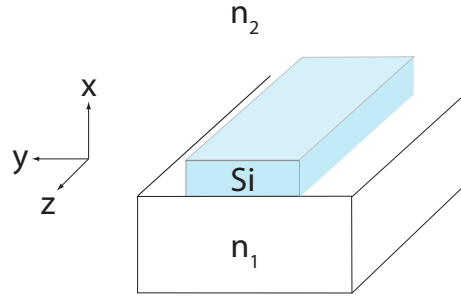


Figure 2.2: Illustration of a wire waveguide with rectangular cross section in silicon as guiding layer. The photonic wire rests on a substrate. In this thesis, this wire is in direct contact with the environment, such that the top and side cladding (n_2) is usually air or an aqueous fluid transporting analytes.

lent treatment on photonic crystals by Joannopolous et al. [3]. Where the ansatz in the previous section was to look for solutions of these equations in the separate dielectric homogeneous zones of the waveguide, and let the boundary conditions do the heavy lifting to tie everything together, we now consider the complete composite structure as one zone. The electric field in the two curl equations 2.1 and 2.2 can be eliminated to obtain an equation strictly in the magnetic field $\mathbf{H}(\mathbf{r})$:

$$\nabla \times \left(\frac{1}{\epsilon(\mathbf{r})} \nabla \times \mathbf{H}(\mathbf{r}) \right) = \frac{\omega^2}{c^2} \mathbf{H}(\mathbf{r}) \quad (2.19)$$

The power of formulating the equations in this way is that we now obtain an eigenvalue problem, of which the operator $\hat{\Theta}$ is Hermitian

$$\hat{\Theta} \mathbf{H}(\mathbf{r}) = \frac{\omega^2}{c^2} \mathbf{H}(\mathbf{r}) \quad (2.20)$$

Formulating the equations in function of $\mathbf{E}(\mathbf{r})$ however, would not generate a Hermitian operator, unless the space is homogeneous. Working with a Hermitian operator offers a lot of advantages: the eigenvalues are real, the eigenfunctions form a complete orthogonal set, and we can organize the eigenfunctions according to their symmetry properties [4].

These symmetry properties can be expressed by operators as well and finding the eigenfunctions of these simple operators allows us to categorize the electromagnetic modes before even looking how they conform under the electromagnetic principles. If we apply this to the slab waveguide pictured in Figure 2.1, we see that the slab has continuous translational symmetry in y and z . This means that

any operator $\hat{T}_{\mathbf{d}}$ which displaces the slab by a distance \mathbf{d} , with \mathbf{d} being any vector in the y,z -plane can generate an eigenfunction of our system. More so, an eigenfunction which is a simultaneous eigenfunction of *all* the $\hat{T}_{\mathbf{d}}$'s, should also be an eigenfunction of our system. It can be proven that this eigenfunction must be of the form $e^{-i\mathbf{k}_{\parallel}\mathbf{r}_{\parallel}}$:

$$\hat{T}_{\mathbf{d}}e^{-i\mathbf{k}_{\parallel}\mathbf{r}_{\parallel}} = e^{-i\mathbf{k}_{\parallel}(\mathbf{r}_{\parallel}-\mathbf{d}_{\parallel})} = e^{i\mathbf{k}_{\parallel}\mathbf{d}_{\parallel}}e^{-i\mathbf{k}_{\parallel}\mathbf{r}_{\parallel}} \quad (2.21)$$

This \mathbf{k}_{\parallel} is the wavevector, in the plane of the slab waveguide, according to which we can classify the modes. Since any wavevector in this plane produces an eigenfunction according to the continuous symmetry operator, they also produce an eigenfunction (or a mode) of $\hat{\Theta}$. So we can write these modes as

$$\mathbf{H}_{\mathbf{k}_{\parallel}} = e^{-i\mathbf{k}_{\parallel}\mathbf{r}_{\parallel}}\mathbf{h}(x) \quad (2.22)$$

If we look for modes who are propagating in z -direction, then the function $\mathbf{h}(x)$ is the magnetic field profile which we have obtained above. In waveguide theory we are looking at waveguides which guide the light in a specific direction. The shape of this waveguide (usually) does not change in the propagation direction. Hence, they all have continuous translational symmetry in the propagation direction (z -direction). We see that this term $e^{-i\beta z}$, which was more or less imposed in the previous section, is a direct consequence of this construction principle of waveguides. There is no other way for the light to propagate in a system which is invariant in its propagation direction. The propagation constant β is thus the z -component of the wavevector.

The slab waveguide has additional symmetries in the form of mirror symmetries. We focus on the mirror symmetry over the plane $y=0$: M_y . This transforms the vector \mathbf{y} to $-\mathbf{y}$, but leaves \mathbf{x} and \mathbf{z} alone. The operator based on this reflection is \hat{O}_{M_y} and it reflects both the input as well as the output of a vector field like $\mathbf{H}(\mathbf{r})$:

$$\hat{O}_{M_y}\mathbf{H}_{\mathbf{k}_{\parallel}}(\mathbf{r}) = M_y\mathbf{H}_{\mathbf{k}_{\parallel}}(M_y\mathbf{r}) \quad (2.23)$$

In [3] it is shown that for a wavevector which is in the mirror plane, such that $M_y\mathbf{k}_{\parallel} = \mathbf{k}_{\parallel}$, and for a point on the plane $M_y\mathbf{r} = \mathbf{r}$, we obtain an eigenvalue problem

$$\hat{O}_{M_y}\mathbf{H}_{\mathbf{k}_{\parallel}}(\mathbf{r}) = \pm\mathbf{H}_{\mathbf{k}_{\parallel}}(\mathbf{r}) \quad (2.24)$$

and a similar one for the electric field $\mathbf{E}_{\mathbf{k}_{\parallel}}$. Now we can classify these modes as either even or odd under the mirror operator. An even mode is one who is left unaltered by the operation, while an odd one acquires a minus sign. So we obtain for the even modes

$$M_y\mathbf{H}_{\mathbf{k}_{\parallel}}(\mathbf{r}) = \mathbf{H}_{\mathbf{k}_{\parallel}}(\mathbf{r}) \quad (2.25)$$

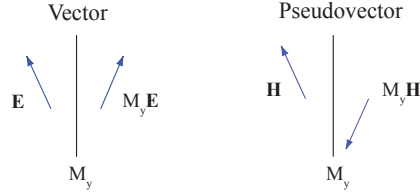


Figure 2.3: Caution must be made when transforming $\mathbf{H}(\mathbf{r})$. It transforms as a pseudovector, which means it acquires an extra minus under mirror reflection. The electric field $\mathbf{E}(\mathbf{r})$ is a vector and reflects as expected.

$$M_y \mathbf{E}_{\mathbf{k}_{\parallel}}(\mathbf{r}) = \mathbf{E}_{\mathbf{k}_{\parallel}}(\mathbf{r}) \quad (2.26)$$

Now the crucial point is that the electric field is a vector, while the magnetic field is actually a pseudovector. This means that under a mirror reflection, the magnetic field acquires an extra minus. The component of \mathbf{H} parallel to the mirror plane is thus reversed, while the component perpendicular to the mirror is not. This is illustrated on Figure 2.3. So the even modes can only have the following non-zero components: the tangential components of the electric field E_x and E_z and the perpendicular component of the magnetic field H_y . These are exactly the components of the TM modes from above. For the odd modes, we obtain that

$$M_y \mathbf{H}_{\mathbf{k}_{\parallel}}(\mathbf{r}) = -\mathbf{H}_{\mathbf{k}_{\parallel}}(\mathbf{r}) \quad (2.27)$$

$$M_y \mathbf{E}_{\mathbf{k}_{\perp}}(\mathbf{r}) = -\mathbf{E}_{\mathbf{k}_{\perp}}(\mathbf{r}) \quad (2.28)$$

Similarly, these can only have non-zero E_y , H_x and H_z , which makes them the TE modes from above. The only thing which is thus required to separate the modes in TE and TM polarizations, is a mirror plane. However, this separation only works under pretty strict requirements: only for points which are located on the symmetry plane itself and only for wave vectors which point in the plane. For a 1D slab waveguide, this is easily realized for waves propagating in the z -direction. Then the mirror plane can be the $y=0$ plane. Furthermore, this mirror plane can slide up and down the y -axis without any change in symmetry behavior, since the structure is uniform in \mathbf{y} . This means, we can always find a plane that fulfills the requirements $M_y \mathbf{k}_{\parallel} = \mathbf{k}_{\parallel}$ and $M_y \mathbf{r} = \mathbf{r}$. We conclude that for all points of the waveguide, the modes are hence either purely TE or purely TM. Mark how the uniformity in a direction orthogonal to the propagation direction is thus leveraged both by the preceding mathematical decoupling of TE and TM modes via solving Maxwell's equations, and by these symmetry considerations.

At first sight, it is peculiar how the separation of TE and TM modes comes down to \mathbf{H} being a pseudovector, and \mathbf{E} a vector. This looks like physics is being dictated by some mathematical sorcery. This is luckily not the case, \mathbf{H} is a pseudovector because of Ampere's law, which is encoded in the equation of Maxwell dealing with the curl of a magnetic field. If a current is running in a loop in counterclockwise direction, it generates a magnetic field pointing upwards. If this situation would be mirrored over a plane parallel to the magnetic field, then the current is running in a loop in clockwise direction, but the magnetic field vector would still be pointing upwards. This is non-physical: the magnetic field should be pointing downwards, and hence the magnetic field has to be a pseudovector.

Having found the root of this decoupling, let's have a look at the mirror symmetries of a rectangular waveguide. In figure 2.4 we see a rectangular waveguide which has two mirror symmetries, M_x and M_y . This corresponds e.g. to a wire waveguide which rests on a silicon dioxide substrate and which is also covered by silicon dioxide. Using the same M_y mirror symmetry as before, we see that we have the separation of modes in this plane. Contrary to the slab waveguide, there is just one M_y symmetry plane, such that outside of this plane, this separation no longer holds! There is also a second mirror symmetry according to which the modes can be categorized: M_x . It is clear that the symmetries are reversed: the TE-modes, which were the odd modes for M_y , are now the even modes for M_x and vice versa for the TM-modes. At points in the waveguide which are not on one of these symmetry planes, the fields are still dominantly polarized according to either TE or TM, as long as the structure is thin in comparison to the wavelength [3]. This is due to the continuity of the field lines. These modes are hence called "TE-like" and "TM-like" or "quasi-TE" and "quasi-TM". Even when the waveguide is an SOI waveguide with air or water as a top cladding and hence loses the M_y symmetry, as is the one we will use for sensing, there is still one symmetry plane left according to which the modes can be forced to be either TE or TM in this specific plane. The small dimensions of the waveguide does the rest by relaxing this polarization constraint slowly. In the following of the thesis we will always use the terms TE and TM, while we are in fact referring to these TE-like and TM-like modes.

Coming back to sensing analytes on top of a waveguide structure, we can have a look at the spatial profiles of these TE and TM modes in an SOI wire waveguide with water as top cladding. Recall that we want to interrogate a thin molecular layer on top of a waveguide with both a TE and a TM mode simultaneously. It is expected that if both modes have a similar mode profile in the watery cladding, it will be difficult to retrieve more information out of two polarizations as opposed to just one: they would roughly react the same way. The dominant electric field

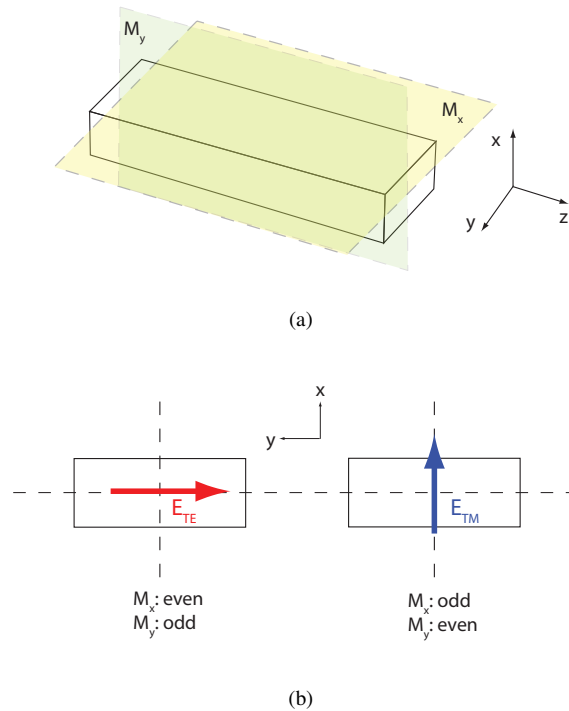


Figure 2.4: (a) Symmetry planes of a rectangular waveguide with equal cladding around the waveguide. (b) The TE and TM modes and their relation to these two symmetries.

components of the fundamental TE and TM mode are shown on Figure 2.5. As dictated by the boundary conditions, we see that the TM mode, which is mainly polarized in the x -direction, has a discontinuous jump at the top side, while the TE mode, which is mainly polarized in the y -direction, has a discontinuous jump at the side walls. Furthermore, we note that the TE mode is more confined to the waveguide core than the TM mode and consequently its propagation constant will be larger. According to these field profiles, the combination of a TE and a TM polarization looks promising for the enhanced analysis of molecular layers.

2.3 Microring resonator

In the previous section we saw how the modes of a waveguide system are a solution of Maxwell's equations for the geometry and the specific materials of the system, as can be seen clearly in the dependency on $\epsilon(\mathbf{r})$ of the eigenvalue problem of equation 2.19. The propagation constant is a scalar representation of this mode and measuring it thus offers a way to determine the specificities of the materials of

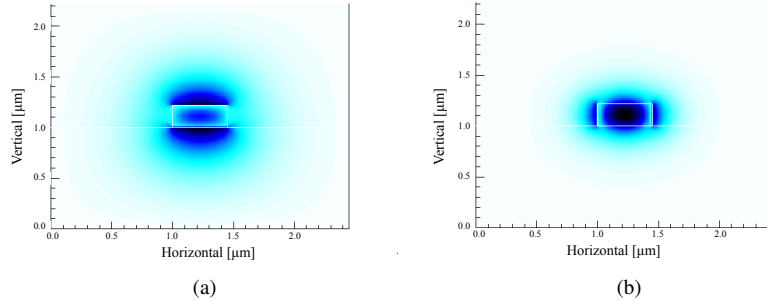


Figure 2.5: Plot of the (a) E_x component of the fundamental TM mode and b) the E_y component of the fundamental TE mode in an SOI waveguide with water as top and side cladding. With x and y defined as in Figure 2.4.

the system. However, the waveguide itself does not offer a straightforward way to measure or transduce this propagation constant. By connecting the input of such a waveguide to its output, we create an optical cavity. Forming a cavity with a waveguide *does* allow us to extract the propagation constant and this happens via the positions of the resonance features of this cavity. This circular waveguide cavity is called a microring resonator [5], whether the cavity forms a perfect circle or not.

What a cavity does, is further restricting the modes which are allowed in the waveguide. For a specific mode profile of a waveguide, we can find an instance of this mode in a continuous range of frequencies or wavelengths, above a certain cut-off wavelength for the specific mode profile. The reason for this is the continuous translational symmetry in the propagation direction which laid no restrictions on the propagation constant. The bounded 2D cross section only limits the modes to a discrete set in this plane. By folding the ring onto itself along the propagation direction, we lose this translational symmetry and the structure is now spatially bound in all three dimensions. Hence restrictions are now put on the propagation constant as well: only a specific discrete set of wavelengths is allowed to exist in the microring. The resonance condition determines which set this is, by zooming back in on the 2D propagating view of the structure. A mode can survive in the cavity, if the accumulated phase shift that is acquired by the 2D mode by running around the cavity exactly one time, is an integer times 2π . Then the mode can sustain itself via constructive interference:

$$\beta L = m2\pi \quad (2.29)$$

Here m is an integer and L is the circumference of the ring resonator. Furthermore,

we introduce a scalar quantity n_{eff} :

$$\beta = \frac{2\pi}{\lambda} n_{eff} \quad (2.30)$$

This allows to compare the propagation constant directly with the materials that interact with the mode via their refractive index. For example, the guided mode condition 2.18 reduces simply to $n_{eff} > n_{cl,max}$. From equation 2.29, the allowed wavelengths are given by:

$$\lambda = \frac{n_{eff} L}{m} \quad (2.31)$$

Thus only wavelengths which fit an integer number of times in the optical path of the cavity roundtrip are allowed in the cavity. A waveguide mode can feed this cavity mode when a waveguide is brought sufficiently close such that the evanescent tail of the cavity mode can overlap with the evanescent tail of the waveguide mode. When two different waveguides are coupling to a microring, the structure is called an add-drop resonator (see Figure 2.6). This is the resonator that has been used predominantly throughout this work.

2.3.1 Add-drop resonator

Coupling of the light to the cavity is governed by the coupling section which couples a fraction k^2 of the power to the adjacent waveguide. When there are no losses in the coupling section, the remaining power fraction r^2 stays in the access waveguide. Thus we obtain for the amplitude cross-coupling coefficient k and for the amplitude self-coupling coefficient r the following relation: $r^2 + k^2 = 1$. The loss due to propagating around the ring once is represented by a (without contributions from the coupling sections). We see on Figure 2.6 that the modes pick up a $\pi/2$ phase shift when they couple from one waveguide to the other. As such, light that couples from the access waveguide to the ring waveguide, does one roundtrip and couples back, interferes destructively with itself due to the resonance condition in the ring. For any wavelength which is allowed inside the cavity, a decrease in power at the pass-port of the add-drop ring resonator will thus be observed. The light keeps on circulating in the ring however, such that there are an infinite number of destructive contributions at the pass port. The ring is said to be critically coupled when all these contributions add up to cancel out the field at the output port completely. This occurs when the total loss in the ring for one roundtrip equals the self-coupling coefficient:

$$r_1 = ar_2 \quad (2.32)$$

At the drop port, the resonant wavelength can couple back out of the ring. This explains the functionality of this add-drop ring resonator as a filter component in WDM-systems for telecommunications [6].

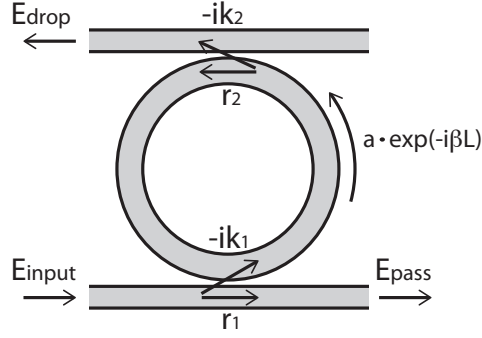


Figure 2.6: An add-drop ring resonator has two coupling sections.

Heebner et al. give a detailed derivation of the power transmission of both ports of this resonator [7]. This is done on the one hand by relating this resonator to the classical Fabry-Perot resonator which is solved using an infinite sum and on the other hand by matching the optical fields of this resonator in a continuous wave regime:

$$T_{pass}(\phi) = \frac{r_1^2 + a^2 r_2^2 - 2r_1 r_2 a \cos \phi}{1 - (ar_1 r_2)^2 - 2ar_1 r_2 \cos \phi} \quad (2.33)$$

$$T_{drop}(\phi) = \frac{a(1 - r_1^2)(1 - r_2^2)}{1 + (ar_1 r_2)^2 - 2ar_1 r_2 \cos \phi} \quad (2.34)$$

These spectra are plotted in Figure 2.7(a) where a repeating pattern of the spectrum is observed, owing to the integer m in the resonance equation. In Figure 2.7(b) we see a close-up of the resonances with the indicated characteristics which relate to the ring quantities as [8]:

$$P_{max} = \frac{(r_1 + ar_2)^2}{(1 + ar_1 r_2)^2} \quad (2.35)$$

$$P_{min} = \frac{(r_1 - ar_2)^2}{(1 - ar_1 r_2)^2} \quad (2.36)$$

$$D_{min} = \frac{a(1 - r_1^2)(1 - r_2^2)}{(1 + ar_1 r_2)^2} \quad (2.37)$$

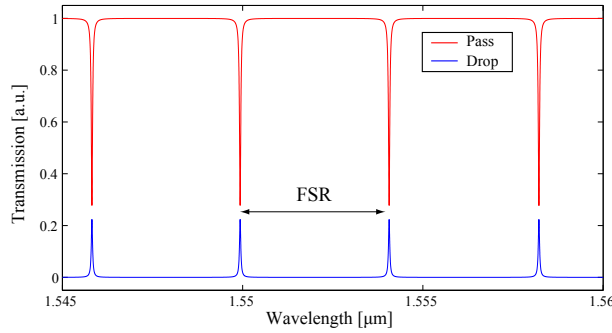
$$D_{max} = \frac{a(1 - r_1^2)(1 - r_2^2)}{(1 - ar_1 r_2)^2} \quad (2.38)$$

$$FWHM = \frac{(1 - ar_1 r_2) \lambda_{res}^2}{\pi n_g L \sqrt{ar_1 r_2}} \quad (2.39)$$

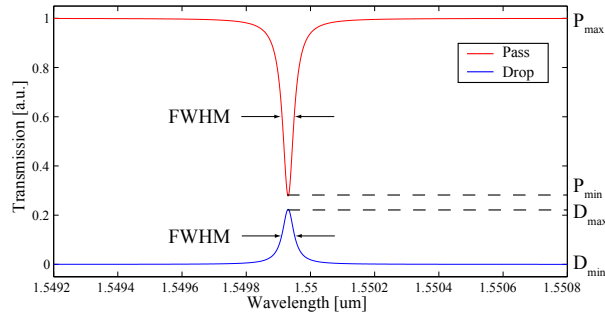
$$FSR = \frac{\lambda^2}{n_g \cdot L} \quad (2.40)$$

An often-used characteristic of a resonator is the Q-factor, which is a relative measure for the sharpness of the peak of a resonance. It also represents the number of oscillations of the field before the energy has decreased by $1/e$. This means that in order to have a high Q-factor, or a sharp peak, we require low loss in the ring:

$$Q = \frac{\lambda}{FWHM} \quad (2.41)$$



(a)



(b)

Figure 2.7: (a) Spectrum at the drop port and the pass port of an add-drop ring resonator with a radius of $20 \mu\text{m}$ showing the repeating filtering behavior. (b) Close-up of a resonance indicating the specific quantities.

A very similar microring resonator is the all-pass microring, which only has one waveguide coupled to the ring and thus only exhibits resonance dips. The

advantage of using this all-pass microring is that the loss in the ring is lower, since no light is lost due to the second coupling section. This increases the Q-factor of the ring. However, obtaining a decent coupling extinction ratio P_{max}/P_{min} (ER) is less evident since the critical coupling equation 2.32 now reduces to $a = r$. When designing this ring, we thus require knowledge of the loss in the ring, as well as an adequate determination of the coupling factor. For many a simulation software, accurate determination of the coupling characteristics can be tricky, due to e.g. the bended structures. Furthermore, the coupling section is very sensitive to fabrication variations such that simulations might be futile, even if they give an adequate estimate of the coupling ratios.

As opposed to an all-pass ring resonator, an add-drop ring resonator is often more robust to fabrication tolerances, since its critical coupling condition is self-referencing. If both coupling sections are designed to be equal, then we can expect any fabrication bias or variation to be equal as well, due to their close proximity. This decreases the effect of fabrication uncertainties. For low loss (high a), this implies further that r_1 will be slightly too high for critical coupling, such that we operate in an undercoupled regime. Equation 2.39 shows that this is beneficial for the Q-factor.

2.3.2 Sensing with a microring resonator

Since the propagation constant (or n_{eff}) of a mode is found together with the mode profile as a solution of the Maxwell's equations to the material system via an eigenvalue equation, it is obvious it will change when a thin layer of molecules is bound to the surface of the ring. Perturbation theory states that a change in $\epsilon(\mathbf{r})$ feeds back to a change in n_{eff} relative to the size of the fields at the perturbation. The fields at these perturbations are exponentially decreasing away from the core. These evanescent tails hence only effectively sense the action close to the waveguide. Because the field profiles of the TE and the TM mode are quite different, so is their sensitivity to these changes.

A change in n_{eff} in turn, determines a change in the resonance wavelength via the resonance condition, since the optical path length changes. The capturing of biomolecules on the microring surface is reflected by an increase in n_{eff} and thus implies a redshift of the resonance wavelength according to the following equation [8]:

$$\Delta\lambda(n, t) = \frac{\Delta n_{eff}(n, t) \cdot \lambda}{n_g} \quad (2.42)$$

In this equation, $\Delta n_{eff}(n, t)$ represents the change in effective refractive index of

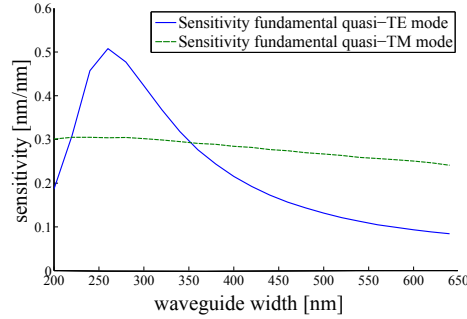


Figure 2.8: Sensitivity of the microring resonator to binding of a thin biolayer in water for fundamental quasi-TE mode and fundamental quasi-TM mode, obtained with Fimmwave. The height of the waveguide is fixed at 220 nm and the excitation wavelength is 1550 nm.

a specific mode due to the presence of the protein layer, λ is the resonant wavelength, while $\Delta\lambda(n, t)$ is the shift of this wavelength due to the protein layer. The group index is represented by n_g and its inclusion ensures that first order dispersive effects are taken into account. Figure 2.8 shows the sensitivity of both modes to a change in layer thickness, expressed as $\frac{\partial\lambda_{res}}{\partial t}$ as a function of the width of a waveguide, with t the thickness of the biolayer. It shows that for waveguides that have a cross section which is wider than 350 nm, the TM mode is more sensitive to changes in the thickness of the layer.

The temperature dependence of the TE and TM modes has been determined experimentally and amounts to 63 pm/K for the TE and 34 pm/K for the TM mode. The sensitivity to bulk index variations and the penetration depths of both modes have been determined via simulations. The sensitivity to bulk index variations for the TE mode amounts to 57 nm/RIU and 222 nm/RIU for the TM mode. The penetration depth is defined as the distance over which the energy density of the modes decrease by a factor $1/e$ and this amounts to 60 nm for the TE mode and 114 nm for the TM mode.

2.4 Designing a dual polarization microring resonator

The practical realization of an add-drop microring, or any of the passive structures in this work, is taken care of by ePIXfab through imec. These structures are fabricated in silicon-on-insulator through a lithographic process, described in [9]. The type of waveguide is a wire waveguide as shown on Figure 2.2. The height (H) of the rectangular cross section is fixed to 220 nm due to the lithographic process, while the width (W) of the waveguide is left free to choose. This width determines (a.o.) the number of modes which are allowed to propagate in the waveguide. We

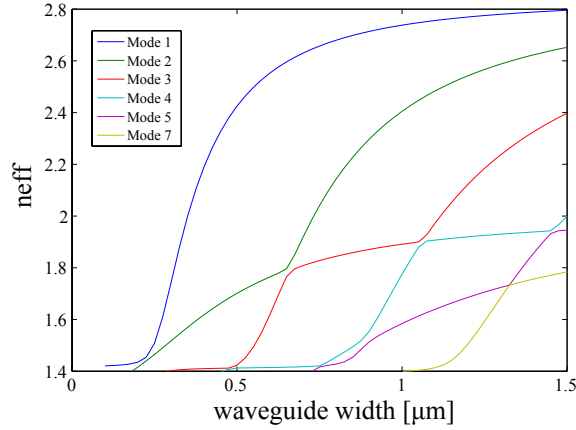


Figure 2.9: Effective index of the first six guided modes for a rectangular waveguide with a height of 220 nm and a watery cladding.

require that no other modes, aside from the fundamental TE and the fundamental TM mode, are allowed in the ring resonator, since coupling to higher-order modes can induce extra loss factors. A mode starts being guided when its effective index is higher than the refractive index of the silicon dioxide (condition 2.18), which equals 1.44. On Figure 2.9, the effective index of the first six modes is plotted with the commercial photonic eigenmode solver Fimmwave. This shows that in order for the third mode to remain in cut-off, the waveguide has to be narrower than 550 nm. Furthermore, we note that for decreasing width, the difference in effective index of the fundamental TE and fundamental TM mode decreases as well. Morichetti et al. have shown that this increases the mutual coupling between these modes in the bends of the microring [10]. The reduced width also causes the propagation losses to increase, which results in a decrease of the Q-factor of the cavity. These considerations lead to a choice of W between 450 and 550 nm.

2.4.1 Simultaneous coupling

Different approaches to excite the ring with two different polarizations are possible. One way would be to provide an access waveguide for each polarization. Leveraging the robustness of an add-drop ring resonator with equal coupling sections and taking care that the length of the coupling section is such that decent coupling is guaranteed for both modes, can lead to good extinction ratios for both TE and TM modes. This method was fabricated and tested in [8]. However, this requires routing to and from the ring of both the TE and the TM mode. It was observed that this creates wildly different power levels at the output due to a dif-

ference in losses, mainly insertion loss and propagation loss. This problem is enhanced in water, where the TM mode has higher absorption loss due to the less confined mode profile.

A different way is to route strictly in the TE mode and to restrict the existence of the TM mode to the microring resonator. This way, all problems due to an unbalanced routing are resolved and standard components for TE polarization, such as grating couplers which couple the light from a fiber to the photonic chip, can be used. To achieve this, the TE routing waveguide must also couple to the TM mode of the ring waveguide. Coupled mode theory can help to understand how we can achieve this. This theory dictates how modes in waveguides that are in close vicinity can couple to each other. Whereas the two adjacent waveguides would normally have to be studied as a compound structure with its own modes, the perturbation principle of coupled mode theory states that these supermodes are merely a linear combination of the modes of the isolated waveguides, with coefficients that vary in the propagation direction. For the simple case of two waveguides which are only supporting a single mode :

$$\begin{cases} \mathbf{E}(x, y) &= A(z)\mathbf{E}_1(x, y) + B(z)\mathbf{E}_2(x, y) \\ \mathbf{H}(x, y) &= A(z)\mathbf{H}_1(x, y) + B(z)\mathbf{H}_2(x, y) \end{cases} \quad (2.43)$$

Here \mathbf{E}_1 is the eigenmode of the access waveguide and \mathbf{E}_2 the one of the ring waveguide. In other words, the modes of the individual waveguide are not changed by the addition of a secondary waveguide, there is only a redistribution of power as we propagate along. Then we obtain for the power in the ring waveguide after a distance z

$$P_b(z) = \frac{|B(z)|^2}{|A_0|^2} = F \sin^2(\sqrt{\kappa^2 + \delta^2}z) \quad (2.44)$$

Here F is the maximum power-coupling efficiency, κ the coupling coefficient which scales with the overlap of the isolated modes, integrated only in the ring waveguide and δ a measure for the mismatch of the propagation constants of the waveguide mode and the ring mode:

$$F = \frac{1}{1 + (\delta/\kappa)^2} \quad (2.45)$$

$$\delta = \frac{\beta_1 - \beta_2}{2} \quad (2.46)$$

$$\kappa \approx \frac{\omega \epsilon_0 \iint_2 \mathbf{E}_1^* \cdot \mathbf{E}_2 \, dx \, dy}{\int_{-\infty}^{\infty} \int_{-\infty}^{\infty} \mathbf{u}_z \cdot (\mathbf{E}_1^* \times \mathbf{H}_1 + \mathbf{E}_2 \times \mathbf{H}_2^*) \, dx \, dy} \quad (2.47)$$

These equations tell us that in order to have a decent coupling efficiency F , we need either the mismatch of the propagation constants to be 0, or if this is not

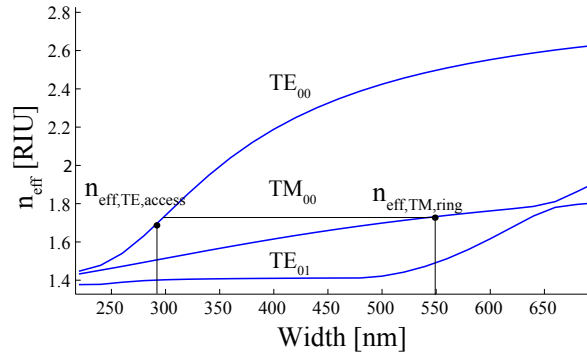


Figure 2.10: Effective index of the first three guided modes for a rectangular waveguide with a height of 220 nm and water cladding. The black lines show the slight phase mismatch for a 550 nm ring waveguide and a 290 nm access waveguide.

possible, the overlap of the fields should be large enough to compensate.

The coupling coefficient κ tells us that if the modes of both waveguides are polarized in a pure TE/TM way, they can't couple to each other since they do not share any field components. We saw in section 2.2 that this pure polarization only occurs in the mirror symmetry planes of the waveguide. This means that if we have an M_x symmetry, as indicated in Figure 2.4 (e.g. when the waveguide would be covered in silicon dioxide), κ is negligible. This plane cuts through both waveguides at the same time, such that the integration domain (the ring waveguide) is still relatively close to this plane. This means that, although the modes are not strictly polarized along the complete height, due to continuity of the field lines and the relative thinness of the waveguide, they are very dominantly polarized, even far away from the waveguide core. This is no longer the case when this symmetry plane disappears. Then the M_y symmetry plane of one of the waveguides is too far away from the other waveguide, where the overlap is integrated, to still force the polarization in an almost-pure state. As such, a non-zero κ is possible. Since this overlap is still small however, we require a high degree of phase-matching. This can be achieved by using an asymmetrical coupling section in which the widths of the access and the ring waveguide are tuned so as to phase match the fundamental TE to the fundamental TM mode [11, 12]. With a width of the ring waveguide of 550 nm and an access waveguide that is 290 nm wide, a small theoretical phase mismatch was achieved between the TE mode of the access waveguide and the TM mode of the ring waveguide of $\Delta n = 0.0481$. On Fig. 2.10, this phase matching

is illustrated. In order for this asymmetrical coupling section to also excite the TE mode of the ring waveguide, we need to overcome the high phase mismatch of both TE modes in the coupling section. To increase κ via the overlap of the fields, we decrease the gap between the two waveguides.

To test this add-drop dual polarization ring resonator, we have designed a ring resonator matrix in which the coupling section was varied from ring to ring. The phase mismatch was changed by taking three different widths of the ring waveguide, with a single width of the access waveguide of 290 nm. Furthermore, gaps between 80-140 nm and coupling lengths between 0-3 μm were chosen. The parameters of the sweep are shown in Table 2.1. Once the SOI chips containing this sensing matrix were fabricated, fiber-to-fiber measurements were performed with water as cladding. For every microring, the resonances were measured and the Q-factor and extinction ratio were extracted for both TE and TM modes, if applicable. On a single spectrum Q and ER are calculated as the median of 4-5 peaks in a span of 20 nm around 1550 nm. An example of a spectrum that exhibits dual polarization functionality is shown in Figure 2.11. The two sets of resonances are visible, each with a different free spectral range. An overview of this measurement is given in Figure 2.12 by means of scatter plots, organized per polarization. The spreads show that the dominant factor for obtaining a specific polarization under these conditions, is the size of the gap. For molecular sensing, a Q factor over 5000 is advisable, while the ER is preferably over 5 dB. On Figure 2.12 (a) we observe that for a gap of 140 nm (and higher), there are no TE modes at all. All twelve rings showed only a TM polarization. For these gaps, the spatial overlap of the electric fields can no longer compensate the phase mismatch. We see that the best TE characteristics are obtained for gaps exactly equal to 120 nm. If the gap is smaller, the resonances become quite small and broad. Furthermore, these small gaps are not reliable fabrication-wise, as they are often not completely etched through. For the TM modes on Figure 2.12 (b), we see that there are only appropriate TM modes for gaps which are 120 nm wide and larger. The generally lower Q-factor of the TM modes, compared to those of TE modes is due to the larger water absorption for TM modes. When we combine both workable regions for TE and TM, only rings with a gap of 120 nm are adequate for sensing.

Ring width	550-520-490	nm
Ring bus	290	nm
Lc	0-1-2-3	μm
Gap	80-90-100-110-120-140	nm
Radius	20	μm

Table 2.1: Design parameters of a coupling section sweep.

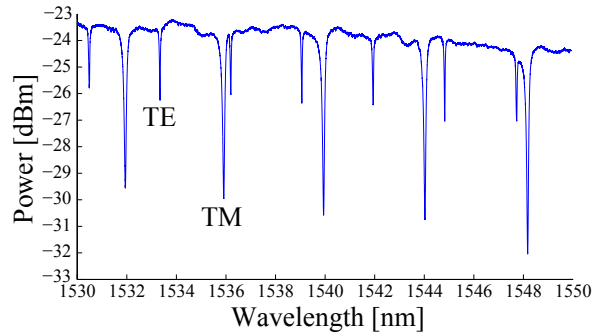
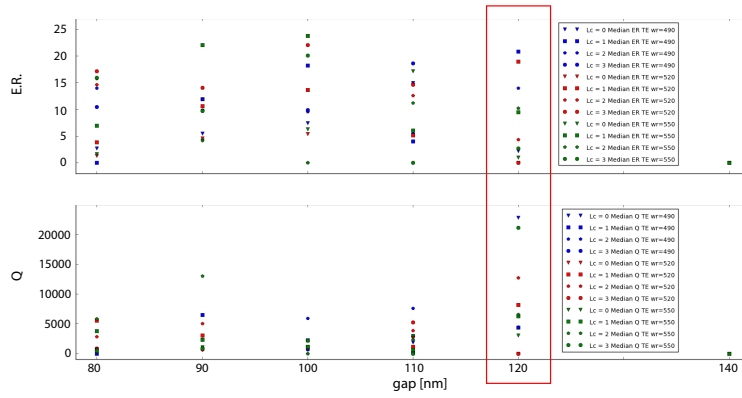


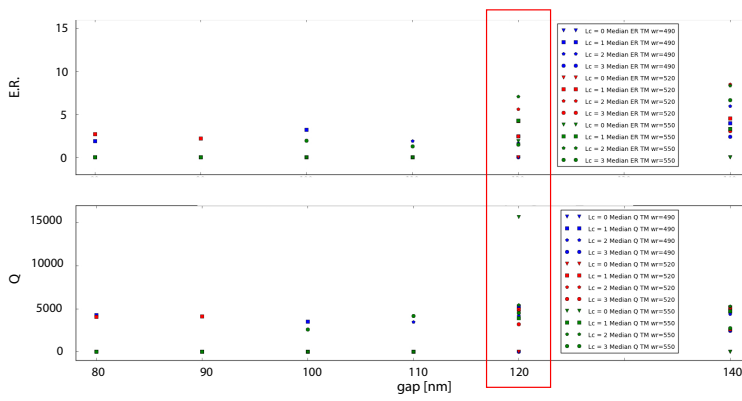
Figure 2.11: Example of a spectrum exhibiting dual polarization functionality, measured when the SOI chip was submerged in water.

After numerous sensing experiments with different chips, we found that the coupling length for a specific waveguide width that exhibits decent dual polarization behavior varies from chip to chip. Due to the small design window where dual polarization behavior is observed, combined with the chip-to-chip variability, we require a set of rings with slowly varying coupling length such that at least one or two rings per gap and ring width show the desired dual polarization functionality. Due to the nature of the lithography process and the small footprint of the sensors, this low yield can be compensated for by placing a sufficient amount of sensors on the chip.

Figure 2.13 shows a top view of the microring and a cross section of the coupling section, obtained with respectively a scanning electron microscope (SEM) and a focused ion beam scanning electron microscope (FIB-SEM). On the top view of the microring we can see that the access waveguide quickly bends away after the coupling section, to reduce the amount of residual coupling in the bends and to better control the coupling. On the view of the cross section we clearly see the asymmetrical coupling section with the broad ring waveguide and the more narrow access waveguide. The actual fabricated gap size amounts to 65 nm, showing the large bias to the gap size on the lithographic mask of 120 nm. This is due to optical proximity effects.



(a)



(b)

Figure 2.12: Scatter plot of the resonances in the microrings with dimensions as given in Table 2.1 of (a) the TE modes and (b) the TM modes. The only gap which exhibits dual polarization functionality are the ones which are 120 nm wide, independently of the phase matching.

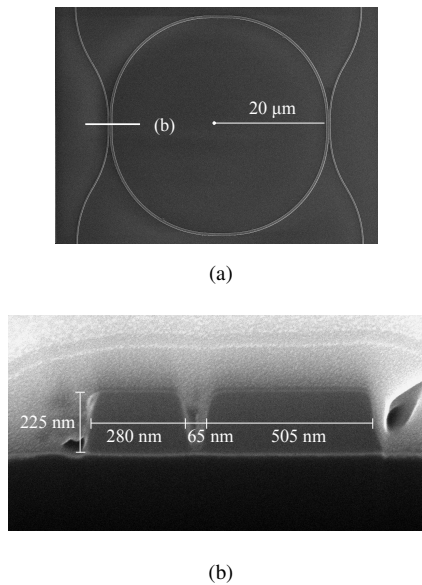
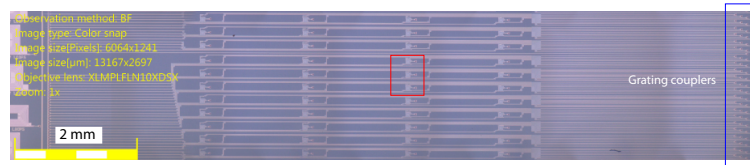


Figure 2.13: (a) SEM image of the microring with two access waveguide. (b) After an ion bombardment, a FIB-SEM image of the cross section of the coupling section is taken, which shows the waveguide dimensions.

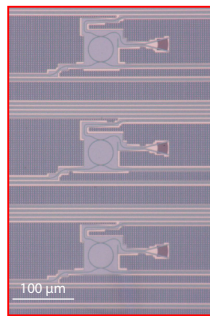
2.5 From a microring resonator to a sensing experiment

The radius of a microring resonator is only $20\ \mu\text{m}$ in size, and the top surface of the ring, where the interaction with the analytes takes place, is a mere $0.5\ \mu\text{m}$ in width. To perform an actual experiment, we need to address the difficulties that arise when working with these microscale sensors. This manifests itself on two levels. First we must interface the analytes which we want to measure with the microring. Since the analytes are dissolved, this is a task addressed by microfluidics. Second, we must measure the wavelength shift of these tiny microring resonators and interpret the result. This will be tackled by the optics and software of the measurement setup.

These practical difficulties are small compared to the new possibilities due to the massive integration and miniaturization effort that is done by silicon photonics. If the transducer has a footprint of $50\ \mu\text{m}$ in two dimensions, many of these transducers can be placed on a photonic chip that has a size of a few square centimeters, paving the way for highly multiplexed applications. Another advantage of this scale factor was mentioned in the design of the dual polarization microring:



(a)



(b)

Figure 2.14: (a) Bright field microscopic image of a section of the sensing matrix. The microring resonators are organized in four columns such that the microfluidic channel can meander easily from column to column. (b) Close-up of the red square in (a), showing three microring resonators.

a low yield of a small component can now more easily be compensated for by a large number of iterations.

From an optical design point of view, the number of microrings on a chip is not limited by the transducer itself, but by the routing of each transducer to in- and output grating coupler. This grating coupler allows the coupling of light from a vertical fiber or from a beam of light to the waveguides in the plane of the chip [13]. Advances have been made in making these couplers more compact and efficient, and in reducing the length which is needed to convert the size of the mode profile from the grating coupler to the narrow waveguide via focused grating couplers [14], but the bottleneck remains. A different approach is to get rid of the routing altogether, and integrate them directly on top of the ring resonators [15]. If we want to integrate these microrings with fluidic transport of analytes however, we find that this optical design limitation is often surpassed by the limitation imposed by the form factor of the microfluidics. Third, the sensor must be organized in such way, which adheres to the form factors of measurement setup as well. A sensing matrix typically used throughout this work is shown in Figure 2.14. The microring sensors are organized in 4 columns and the input and output grating

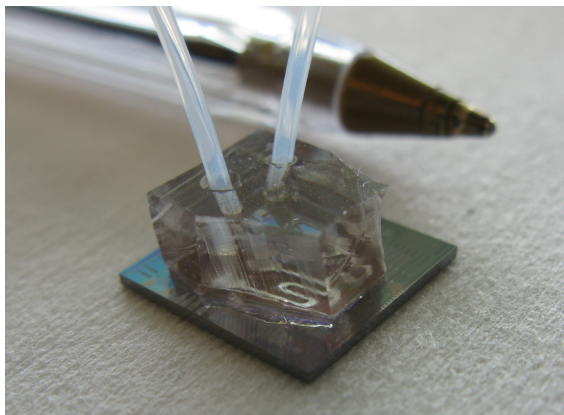


Figure 2.15: Picture of the SOI sensing chip with 5 mm high PDMS fluidic cell bonded on top. Tubings are inserted which connect the fluidic channels with the analytes.

couplers are on either side of the chip. It is clear that the microring sensors only make up a small fraction of this sensing matrix. Janz et al. have managed to cram 128 sensors on an SOI photonic chip with integrated microfluidics which could be read out simultaneously [16].

2.5.1 Microfluidics

By bonding a microfluidic polydimethylsiloxane (PDMS) cell [17], a fluid containing analytes can be flown over the chip surface through a microfluidic channel. These channels have a cross section of $400\ \mu\text{m} \times 50\ \mu\text{m}$ and meander over the microrings, which are organized in columns with sufficient spacing. Tubings can be inserted in the PDMS cell to connect the channels to a fluidic pump and a reservoir containing the analytes via a Rheodyne 6-port valve. The valve can switch between running fluid and a sample loop, such that specific analytes can be injected in small volumes. The sample loop is typically filled with about $100\ \mu\text{l}$. A picture of the photonic chip with PDMS cell bonded on top is depicted on Figure 2.15.

The pattern of the microfluidic channels can be designed via lithography. To do so, a mold with a periodic pattern of channels is made with photodefinable SU-8 on an unpatterned silicon wafer. The liquid PDMS is subsequently poured over this mold and left to cure for 4 hours at $80^\circ\ \text{C}$. The PDMS thickness is usually chosen to be 0.5 cm to facilitate the insertion of the tubes. After curing, the individual microfluidic chips can be cut out and holes are punched through them. This is done manually. To bond the silicon chip to the polydimethylsiloxane (PDMS) fluidic cell, both the chip and the PDMS are treated with an oxygen plasma. This activates the silicon surface by creating reactive silanol groups such that the silicon

chip can bind covalently to the PDMS cell during a 45 minute heating step of 135° C. Alternatively, a stamp-and-stick method can be used as bonding method. This method uses the UV-sensitive polymer SU-8 which functions as a glue between the PDMS cell and the SOI chip. After applying the glue and aligning SOI chip and PDMS cell, the bonding is assured via a 180 seconds UV illumination step. The advantage of this method is that high temperatures are avoided, which could be detrimental for biochemical functionalisation. A last method is to use a mechanical clamping to avoid both UV illumination and high temperatures. However, this complicates the alignment and makes the SOI chip subjective to mechanical stress, which can be picked up by the sensors. Details regarding the processing of PDMS, the direct bonding as well as the stamp-and-stick method can be found in the dissertation thesis of K. De Vos [18].

2.5.2 Measurement setup

For the sensing experiments conducted in this thesis we have used two setups to track the resonance features of the microrings. A Santec TSL-510 tunable laser is used, which is coupled vertically to the SOI sensing chip by means of either an optical fiber (setup 1) or via a collimator and free space illumination (setup 2). Setup 1 is shown on Figure 2.16 (a) and a close-up of the chuck stage is shown on Figure 2.16 (b). This setup can be easily altered to setup 2 by swapping the fiber stage for a collimator, which is shown in Figure 2.16 (c). The input grating couplers are excited and couple light via the routing waveguides to the microrings and at the other end of the chip, the output grating couplers divert the light back into the vertical direction, where collection optics gather the light and focus it onto a Xenics Xeva camera. This causes the various rings to be imaged on different pixels of the camera and hence these can be monitored simultaneously. The camera does not have a spectrally sensitive element, such that we have to sweep the single-wavelength laser in order to generate a spectrum. This requires careful triggering and synchronizing between software, laser and camera. The excitation wavelength is usually swept over a range of 10 nm. Custom-built software reconstructs the output spectrum, tracks the position of the resonant modes over time and solves these to a certain thickness and refractive index. This analysis system is largely covered in chapter 3.

The difference between the two setups is the manner of illumination. The free-space illumination of setup 2 relaxes the optical alignment requirements greatly, making the system robust. It can however generate a parasitic signal, which reflects from the bottom of the chip and couples back into the waveguide, causing a distortion of the output spectrum. The ripple on Figure 2.17(b) is due to this effect. This phenomenon is discussed in [19], where solutions are proposed. The

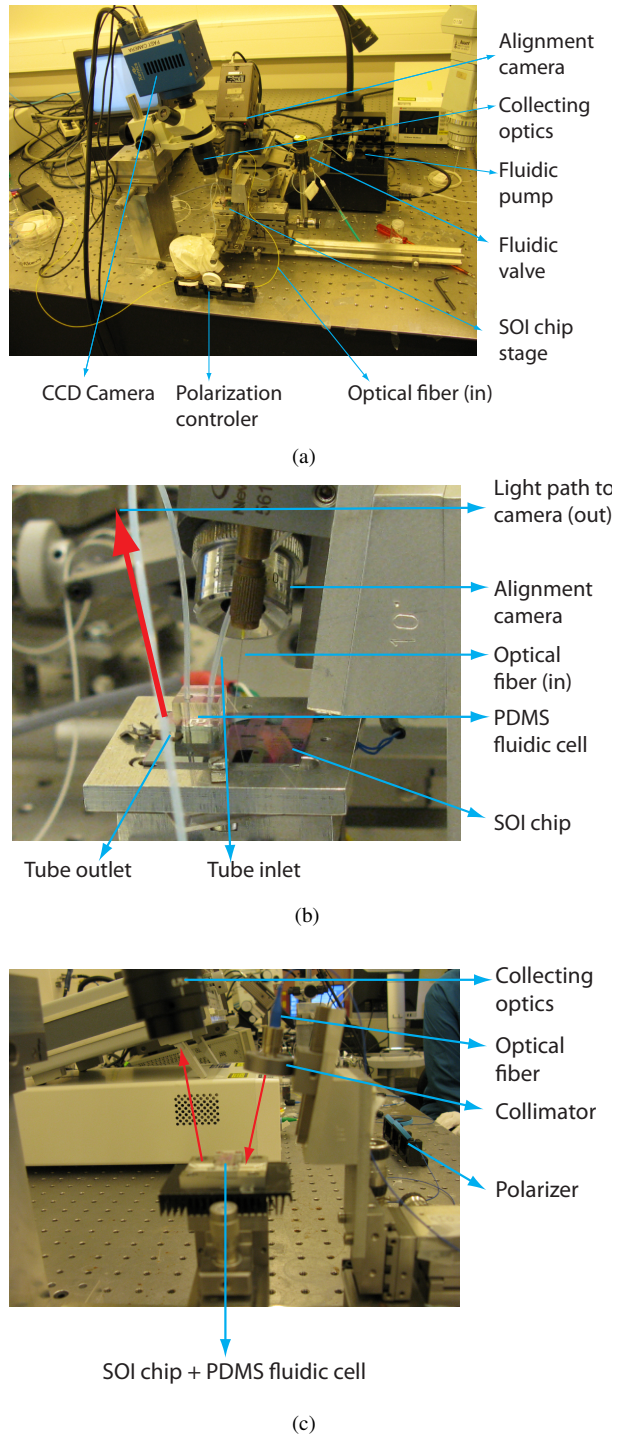


Figure 2.16: (a) Photograph of measurement setup 1 that excites the SOI chip with a fiber. (b) Zoom of the SOI chip stage of this setup that shows the PDMS cell bonded to the SOI chip. The input of the SOI chip is to the right, where the fiber couples light in. On the left-hand side of the SOI chip, the light couples back out vertically according to the red arrow, where it is collected by optics (not on the photograph). (c) This setup can be adjusted to setup 2 by replacing the fiber by a collimator. The alignment camera is in that case no longer necessary

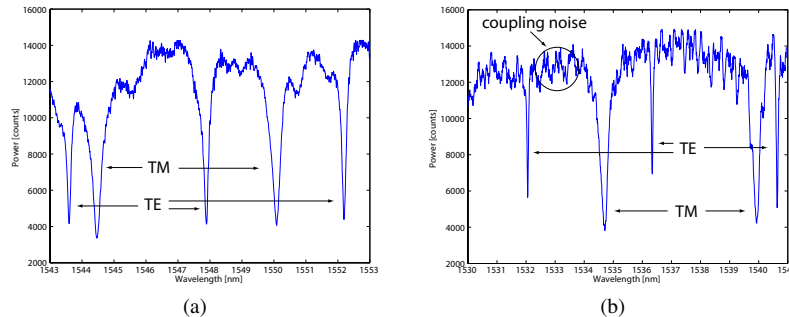


Figure 2.17: Spectrum of the sensing ring with a water cladding of as measured by the measurement setup for biochemical experiments. (a) The SOI microring has a rectangular cross section with a width of 520 nm and a height of 220 nm. The optical input section of the sensing ring is excited by means of an optical fiber. (b) The SOI microring has a rectangular cross section with a width of 550 nm and a height of 220 nm and the optical input coupler of the sensor is illuminated by a collimated laser beam.

fiber coupling method on the other hand does not suffer from this parasitic effect if the fiber can be carefully aligned over the grating coupler, for which an additional camera is required. If the sensors need to be addressed simultaneously for a multiplexed experiment with a fiber, then splitters are required in the optical chip to fan out the single input channel. These splitters might introduce reflections themselves however.

2.5.3 Detection of PSA antigens

In this section a typical bio-experiment is presented by means of the detection of protein specific antigen (PSA). For this experiment, free-space illumination (setup 2) was used and 10 microring resonators were tracked in parallel. The microring mode is the fundamental TE mode. The shifts have been plotted as a function of time on Figure 2.18. The goal is to immobilize PSA-antibodies on the surface, and in a later stage verify whether PSA-antigens can be detected at a concentration of 30 ng/ml. In order to attach biomolecules to a silicon surface, the surface needs to be silanized first. This is done beforehand with 3-aminopropylsilane (APTES), which introduces an NH₂ group on the surface. It is a standard process to silanize silicon surfaces with [20, 21]. After silanization, the SOI chip is bonded to the PDMS cell with the stamp-and-stick method. The chip is inserted in the setup and the surface is first activated with a glutaraldehyde crosslinker. Then the anti-PSA is streamed over the chip surface, followed by a BSA blocking step, and a glycine rinsing. Before and after every injection of a certain analyte, the fluid is switched back to buffer, which is phosphate buffered saline (PBS). This is because the amount of analyte which is bound to the chip surface is related to the net shift

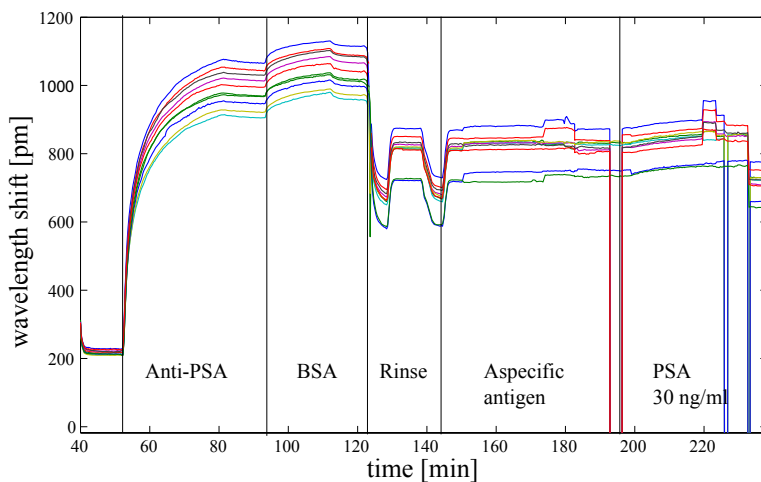


Figure 2.18: Detection experiment of PSA-antigen on an SOI chip on which the PSA-antibodies are immobilized on the microrings. This is done by using an APTES+glutaraldehyde strategy.

before and after binding. During the streaming of analytes there is an association phase followed by an equilibrium phase when the association and dissociation of analytes are balancing out. When the fluid switches back to buffer, there is only dissociation. From the association phase, the kinetics of the reaction can be obtained [18]. In this experiment an aspecific antigen does not produce significant response from the sensor. The subsequent streaming with a 30 ng/ml PSA in PBS does generate a net shift of 20-30 pm.

2.6 Obtaining physical characteristics

While the previous example showed how a single polarization experiment looks like, in the experiments of the following chapters, we will use two polarizations to interrogate the molecular layer. Each polarization will thus have its own sensorgram, similar to the one shown in Figure 2.18. In chapter 3, we will see how both sensorgrams can be solved to a thickness and refractive index profile of the molecular layer during the experiment. Some confusion can arise here concerning the interpretation of the refractive index. This refractive index of the thin layer is not a constant: it can not be measured outside of the microring setup and is not equal to the bulk refractive index of the analyte as given by the vendor, or found

in literature. It is a quantity related to the mass concentration of the analyte inside the thin molecular layer.

Optically, the region surrounding the waveguide is divided in two parts: a thin molecular layer with a certain refractive index n and thickness t , and a layer with infinite thickness and a different refractive index n_b above. This second layer represents the bulk fluid which is streaming over the microring resonator. In reality, the bulk fluid also surrounds the bound analytes in the thin molecular layer causing it to be hydrated. Therefore, the volume density of the analyte layer ρ has contributions from the mass concentration of the analyte in the layer ρ_a and from the mass concentration of the bulk fluid in the layer ρ_b :

$$\rho = \rho_b + \rho_a \quad (2.48)$$

The mass concentrations in the layer equal the product of the bulk volume density and the mass fraction in this specific layer. These bulk volume densities are constants. For the analyte, the bulk volume density is the dry density as obtained by the vendor.

$$\rho = \rho_{b,bulk} \cdot w_b + \rho_{a,bulk} \cdot w_a \quad (2.49)$$

The mass fractions in the layer can be related directly to the *measured* refractive index n of the molecular layer, by assuming linear relations:

$$w_b = \frac{n_a - n}{n_a - n_b} \quad (2.50)$$

$$w_a = \frac{n - n_b}{n_a - n_b} \quad (2.51)$$

Here, n_b is the bulk refractive index of the bulk fluid running over the sensor, while n_a is the refractive index of the dry analyte. The mass fraction of the bulk fluid in the molecular layer w_b can also be referred to as the hydration of the layer. Using these equations, we obtain the mass concentration of the analyte in the molecular layer as

$$\rho_a = \rho_{a,bulk} \frac{n - n_b}{n_{a,bulk} - n_b} \quad (2.52)$$

This equation is also found by Lillis et al. in [22]. Finally, the adsorbed mass per surface unit (M) is now easily calculated as the product of the analyte mass concentration (ρ_a) and the thickness (t) of the layer:

$$M = \rho_a t \quad (2.53)$$

References

- [1] A. Yariv and P. Yeh. *Photonics: optical electronics in modern communications*. Oxford, New York, 2007.
- [2] K. Okamoto. *Fundamentals of optical waveguides*. Elsevier, 2006.
- [3] J. D. Joannopoulos, S. G. Johnson, J. N. Winn, and R. D. Meade. *Photonic Crystals: Molding the Flow of Light*. Princeton University Press, New Jersey, 2008.
- [4] R. Shankar. *Principles of quantum mechanics*. Plenum Press., New York, 1982.
- [5] Wim Bogaerts, Peter De Heyn, Thomas Van Vaerenbergh, Katrien De Vos, Shankar Kumar, Tom Claes, Pieter Dumon, Peter Bienstman, Dries Van Thourhout, and Roel Baets. *Silicon Microring Resonators*. *Laser Photonics Rev.*, 6:1–28, 2011.
- [6] Peter De Heyn, Jeroen De Coster, Peter Verheyen, Guy Lepage, Marianna Pantouvaki, Philippe Absil, and Wim Bogaerts. *Fabrication-Tolerant Four-Channel Wavelength-Division-Multiplexing Filter Based on Collectively Tuned Si Microrings*. *Journal of Lightwave Technology*, 31(16):2785–2792, 2013.
- [7] J Heebner, R. Grover, and T. Ibrahim. *Optical Microresonators: Theory, Fabrication and Applications*. Springer, 2008.
- [8] Tom Claes. *Labelvrije biosensoren op basis van geavanceerde fotonische ringresonatoren in silicium*. PhD thesis, UGent, 2012.
- [9] S. K. Selvaraja, P. Jaenen, W. Bogaerts, D. Van Thourhout, P. Dumon, and R. Baets. *Fabrication of Photonic Wire and Crystal Circuits in Silicon-on-Insulator Using 193nm Optical Lithography*. *J. Lightwave Technol.*, 0:1–8, 2009.
- [10] Francesco Morichetti, Andrea Melloni, Associate Member, and Mario Martinelli. *Effects of Polarization Rotation in Optical Ring-Resonator-Based Devices*. 24(1):573–585, 2006.
- [11] Liu Liu, Yunhong Ding, Kresten Yvind, and Jørn M Hvam. *Silicon-on-insulator polarization splitting and rotating device for polarization diversity circuits*. *Optics express*, 19(13):12646–51, June 2011.
- [12] Peter De Heyn, Diederik Vermeulen, Dries Van Thourhout, and Gunther Roelkens. *Silicon-on-Insulator All-Pass Microring Resonators Using a*

- Polarization Rotating Coupling Section*. IEEE Photonics Technol. Lett., 24(14):1176–1178, 2012.
- [13] Dirk Taillaert, Frederik Van Laere, Melanie Ayre, Wim Bogaerts, Dries Van Thourhout, Peter Bienstman, and Roel Baets. *Grating Couplers for Coupling between Optical Fibers and Nanophotonic Waveguides*. Japanese Journal of Applied Physics, 45(8A):6071–6077, August 2006.
- [14] D Vermeulen, K Van Acoleyen, S Ghosh, S Selvaraja, W A D De Cort, N A Yebo, E Hallynck, K De Vos, P P P Debackere, P Dumon, W Bogaerts, G Roelkens, D Van Thourhout, and R Baets. *Efficient Tapering to the Fundamental Quasi-TM Mode in Asymmetrical Waveguides*. In European Conference on Integrated Optics, 2010.
- [15] Sam Werquin, Yannick De Koninck, and Peter Bienstman. *Ring Resonators With Vertically Coupling Grating for Densely Multiplexed Applications*. IEEE Photonics Technology Letters, 27(1):97–100, 2015.
- [16] S. Janz, D. Xu, M. Vachon, N. Sabourin, P. Cheben, H. Mcintosh, H. Ding, S. Wang, J. H. Schmid, A. Del age, J. Lapointe, A. Densmore, R. Ma, W. Sinclair, S. M. Logan, R. Mackenzie, Q. Y. Liu, D. Zhang, G. Lopinski, O. Mozenon, M. Gilmour, and H. Tabor. *Photonic wire biosensor microarray chip and instrumentation with application to serotyping of Escherichia coli isolates*. Opt. Express, 21(4):4623–4637, 2013.
- [17] J. Cooper McDonald, David C. Duffy, Janelle R. Anderson, Daniel T. Chiu, Hongkai Wu, Olivier J.A. Schueller, and George M. Whitesides. *Review General Fabrication of microfluidic systems in poly (dimethylsiloxane)*. Electrophoresis, 21(1):27–40, 2000.
- [18] Katrien De Vos. *Label-free Silicon Photonics Biosensor Platform with Microring Resonators*. PhD thesis, UGent, 2010.
- [19] Sam Werquin, Diedrik Vermeulen, and Peter Bienstman. *Implementation of Surface Gratings for Reduced Coupling Noise in Silicon-on-Insulator Circuits*. IEEE Photonics Technol. Lett., 26(16):1589–1592, 2014.
- [20] Katrien De Vos, Irene Bartolozzi, Etienne Schacht, Peter Bienstman, and Roel Baets. *Silicon-on-Insulator microring resonator for sensitive and label-free biosensing*. Optics express, 15(12):7610–5, June 2007.
- [21] Jos  Luis L pez-Paz, Miguel  ngel Gonz lez-Mart nez, Jorge Escorihuela, Mar a-Jos  Ba nuls, Rosa Puchades, and  ngel Maquieira. *Direct and label-free monitoring oligonucleotide immobilization, non-specific binding and DNA biorecognition*. Sensors and Actuators B: Chemical, 192:221–228, March 2014.

- [22] B. Lillis, M. Manning, H. Berney, E. Hurley, A. Mathewson, and M. M. Sheehan. *Dual polarisation interferometry characterisation of DNA immobilisation and hybridisation detection on a silanised support*. *Biosens. Bioelectron.*, 21(8):1459–1467, February 2006.

3

Analysis framework

3.1 Introduction

In the previous chapter we have seen that it is feasible to interrogate a molecular layer on top of a microring with two optical modes simultaneously. This required knowledge on the physics of the microring resonator and on the intricacies of optical integrated design. The descriptions in this chapter are on a higher level of abstraction: that of data processing and system design. This is largely necessary due to the complexity of the signal transduction. The shifts of the resonance wavelengths are no longer the final signal on which the analysis is made, as is the case for a microring resonator with a single polarization. For this dual polarization system, these resonance shifts are merely intermediate signals which need to be decoded to unveil the physical quantities thickness (t) and refractive index (n). The transduction penetrates to the molecular layer itself. This is not to say that a single polarization microring is not capable of giving direct first-hand information on the molecule under test. But in order to link the measured shift to a concentration for example, a calibration curve is required. A set of premade solutions with known concentration needs to be flown over the sample while the resonance shift is tracked. In a certain linear domain, an unknown concentration can then be extracted from a measured shift by using this calibration curve [1]. In other words, complete abstraction is made of whatever happens on the level of the microring sensor: all analysis is made on the temporal behavior of the shifts. Hence, anything that invokes a shift of the resonance wavelength will be interpreted as the binding

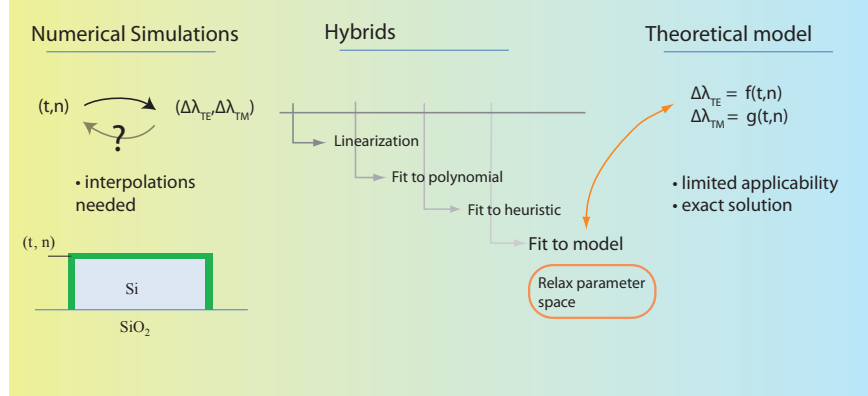


Figure 3.1: Different techniques on how to obtain the unknown thickness and refractive index out of the measured shifts. The techniques are ordered on a scale based on the relative importance of a theoretical model.

of the molecule which needs to be quantified. The selectivity is outsourced to the chemical probes on top of the microring.

In case of the dual polarization microring we need to install an analysis framework in between the resonance wavelength shifts and the biophysical behaviour of the molecules. Working with an experimental calibration in this case would be impossible: we would need to get hold of a certain molecule which we can force in a certain conformation. Furthermore, the experimental paradigm of this system is completely different than for a single microring which detects a single unknown. For a (t,n) measurement, we generally know the substance which we stream over the microring, but we are interested in the (unknown) conformation or the adsorption behaviour of the molecule. Hence we can't calibrate for it experimentally.

3.2 Different approaches to extract t and n

In its most simple form the analysis framework is a series of operations on the wavelength shifts of the TE and the TM mode such that the thickness and the refractive index are obtained:

$$t = F(\lambda_{TE}, \lambda_{TM}) \quad (3.1)$$

$$n = G(\lambda_{TE}, \lambda_{TM}) \quad (3.2)$$

It is more evident however to construct the opposite system which tells us what the wavelength shifts of the resonance modes are in function of t and n . Generally, there are two distinct ways to tackle this problem, which are illustrated in Figure

3.1: via a theoretical model or via numerical simulations.

With respect to a theoretical model, Maxwell's equations and waveguide theory form an excellent base. As such we obtain equations which come from analytical descriptions of the electromagnetic field in the mathematical form of functions which are valid over a wide range in time and space. Therefore, these are only completely valid for simple geometries such as a slab waveguide. The advantage of having such an analytical system of equations connecting (t, n) with $(\Delta\lambda_{TE}, \Delta\lambda_{TM})$:

$$\Delta\lambda_{TE} = f(n, t) \quad (3.3)$$

$$\Delta\lambda_{TM} = g(n, t) \quad (3.4)$$

is that we can use existing solving algorithms to invert these relations to give an exact solution for t and n , given a certain set of shifts. An example of this method put into practice is the dual polarization interferometry tool devised by the now defunct Farfield. The waveguides used in this method are slab waveguides such that a purely analytical treatment is possible [2].

Another way of tackling this problem is by using a simulation package which uses numerical methods such as Finite Element Method (FEM) to obtain the shifts for a complex waveguide structure with very high accuracy. This is the virtual analogue of performing a calibration measurement. However, since we are dealing with a system with two unknowns, it is not straightforward to invert this relation and obtain the molecular layer characteristics from the measured shifts, even more so since we only have the shifts for a discrete set of points. Interpolating and computational solving methods can give us the thickness and refractive index based on this simulated mesh, but errors will always be present due to the meshing and the highly nonlinear character of the functions f and g .

A system inbetween these two extremes where a function can be tied to the simulated discrete points to cross the gaps in between those points in a natural, physical way is desired. These solutions are the hybrids which are ordered on Figure 3.1 depending on the importance of the theoretical-analytical component. In the linearization process the simulations are limited to the sensitivities or the partial derivates of the effective index of both modes to changes in thickness and refractive index:

$$\begin{pmatrix} \Delta n_{eff,TE} \\ \Delta n_{eff,TM} \end{pmatrix} = \begin{pmatrix} \frac{\partial n_{eff,TE}}{\partial n} & \frac{\partial n_{eff,TE}}{\partial t} \\ \frac{\partial n_{eff,TM}}{\partial n} & \frac{\partial n_{eff,TM}}{\partial t} \end{pmatrix} \cdot \begin{pmatrix} n \\ t \end{pmatrix} \quad (3.5)$$

This small-signal analysis can be easily inverted to obtain unknown t and n , and is fast since a limited amount of simulations are needed. This system has been

suggested for dual polarization microring resonators in [3]. However, the extreme nonlinear behavior of functions f and g will introduce rather large errors for very small signals. Moving further towards the theoretical model case, we find approaches that fit a mesh of simulated points to a polynomial, spline or any other general mathematical formulation. While this does not give any physical interpretation of the simulation results, one might argue that any mathematical function can be decomposed in a polynomial series via a Taylor expansion. Therefore, increasing the number of polynomial factors would converge the function towards its underlying physical origin. This can be dangerous however, since the simulated results are also found by non-exact computational techniques. The converging stops whenever these points are perfectly fit to, but they themselves are not a perfect representation of the physics: we might look for something that can't be found by taking these simulated points as absolute truth. Also, any numerical mistakes made by the simulated software will be fitted to and can propagate, and this to a higher degree when the number of fitting parameters increases. More physically is a heuristic model which is inspired by physical concepts but not rigorously derived from its equations. For example, Claes et al. have suggested a model holding middle ground between a heuristic and a polynomial [4]:

$$\Delta\lambda_{TE}(n, t) = t \cdot (n - n_{bulk}) \cdot h_{TE}(n, t) \quad (3.6)$$

$$\Delta\lambda_{TM}(n, t) = t \cdot (n - n_{bulk}) \cdot h_{TM}(n, t) \quad (3.7)$$

Here, the shifts are defined relative to the situation where a bulk fluid is flowing over the sensor and no molecules have been in contact with the sensor yet. The refractive index of the bulk fluid is denoted as n_{bulk} , and the function h is an unknown function which is set to a first order polynomial in t and n in order to fit the simulations in an adequate way. The heuristic part comes from the realization that for a zero thickness and for a layer refractive index equal to the refractive index of the bulk fluid, the shift should be zero. Good results have been obtained, but the range of possible layers this solves correctly to is limited as well.

Different versions of the models which we have described here have been tested and applied to various experiments during the course of this PhD project with varying degrees of success in accuracy and robustness. Finally we have chosen to work with a model which is positioned closer to the theoretical model. In fact, a theoretical model has been devised which can be fitted to the simulated results. This seems like a paradox, since a true theoretical model has no fitting parameters. However, we have introduced certain parameters in the model to be fitted to, such that the rigid model would gain some flexibility. This is necessary to migrate from an idealized theoretical waveguide geometry which does not conform to the correct fabricated waveguide geometry of an SOI wire waveguide. This infusion of parameters is a careful one-by-one process. Too much parameters

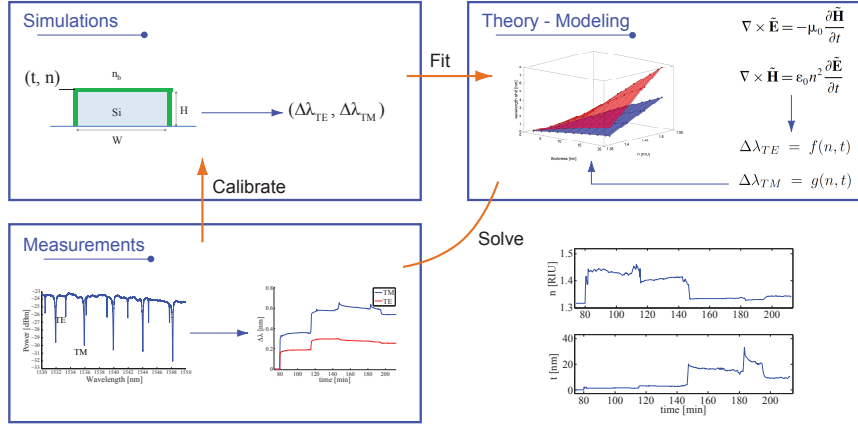


Figure 3.2: Schematic overview of the different aspects of the solving framework. The spectrum is measured and the peaks of the TE and TM modes are tracked. This feeds into the simulations to calibrate the waveguide profile. These simulations are fit to a theoretical model, derived from waveguide theory. Finally the measured shifts are solved with this model to obtain the thickness and density profile.

will provide the freedom for the model to also fit to numerical errors given by the simulation software, and a model which has not enough parameters can not adapt from the theoretical waveguide profile to the simulated one.

3.3 Solving framework overview

In this section we dive deeper and set up a practical signal flow which extracts t and n out of the resonance shifts. This framework encompasses three parts: measurements, simulations and theoretical modeling. A logical overview of this is given in Figure 3.2. We start where we have left off in the previous chapter: with the continuous capturing of the transmission spectra of the microring resonators. These spectra are analyzed using routines written in Python, which extracts the shift of the TE and TM resonances. This is not straightforward, since the TE and TM modes are mixed a single spectrum. An example of a spectrum is given in the *Measurements* section of Figure 3.2. The TM modes have a higher sensitivity than the TE modes and thus the order of the peaks is not constant during the experiment. Neither is the number of peaks since it occurs frequently that a TE and a TM peak overlap. Due to the sensitivity of the asymmetrical coupling section, the amplitudes of the TE or TM peaks can change from chip to chip such that a classification based on amplitude is not always possible, therefore we opt to differentiate based on FSR.

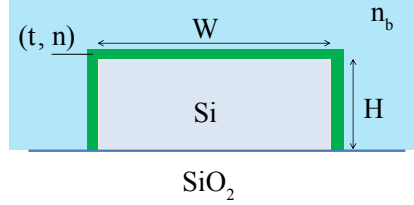


Figure 3.3: 2D cross section of an SOI wire waveguide as it is solved by Fimmwave. For a given set of parameters W , H and n_b , the waveguide profile is solved and n_{eff} and n_g are obtained for a number of modes. This is repeated for a wide range of possible layers with characteristics (t, n) , which cover the waveguide profile.

Using a 2D mode solver such as Fimmwave [5], we obtain the effective index n_{eff} and the group index n_g of the TE and TM mode of a wire waveguide with a rectangular cross section as depicted in Figure 3.3. The refractive index of the bulk fluid, as well as the width (W) and height (H) of the waveguide needs to be calibrated for (see section 3.5). In a first stage the mode characteristics are obtained without a thin molecular layer covering the silicon surface. This counts as a reference for the wavelength shifts. Afterwards, a thin layer is added and the modes are solved while sweeping over different values of t and n . Using equation 2.42, we obtain the TE and TM shifts for a two-dimensional grid spanned by $t = 0 - 200$ nm and $\Delta n = 0 - 0.2$ RIU, with $\Delta n = n - n_b$.

These simulated points serve as a starting point to fit a theoretical model to. However, it is possible for the simulation tool to produce a non-physical result. This is illustrated in Figure ?? where the group index is plotted for a layer thickness of 5 nm, in function of the refractive index of the layer which is added on top. By increasing the amount of modes the internal solver uses to compute the effective index, the amount of faulty points is reduced. However, for a single point, we observe a damped oscillatory behavior of the error of this point in function of the number of modes. To get rid of these kind of simulation errors, we fit the theoretical model in an iterative manner to the simulation results. Whenever a residue of the fit to the points is too large, we get rid of this point and redo the fitting. In essence, we use the model as a metric to locate numerical errors of the simulation software. Finally, the measured shifts are solved to this model and we obtain the refractive index and thickness profile. Both the fitting and subsequent solving is performed in Matlab.

After discussing the measurements and the simulations, we will now expand on the theoretical model, which is involved enough to warrant its own section.

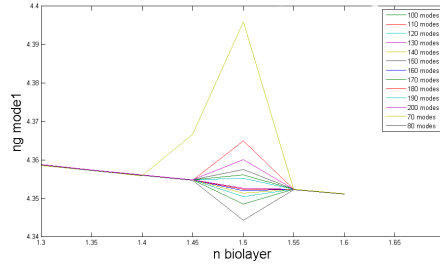


Figure 3.4: Example of the group index as simulated by Fimmwave for a thickness of the biolayer of 5 nm and various refractive indices. The different curves represent simulations done with an increasing amount of internal modes. This can be considered the resolution of the simulation. It is clear that by increasing the number of modes, the numerical error of the $n=1.5$ point gets damped, but it does not completely disappear.

3.4 Mathematical model

As we have seen in chapter 2, the electromagnetic field profiles of a waveguide can be found as the eigenfunctions of an eigenvalue problem of a linear Hermitian operator (equation 2.19). The eigenvalues linked to these field profiles are the frequencies (or the wavelengths). The effect of small perturbations due to for instance the addition of a thin layer is governed by perturbation theory. It says that a small perturbation in the dielectric profile propagates to the eigenvalues by means of a series expansion in terms of increasing power of the dielectric perturbation. This can be done in first order by using only the field profiles of the unperturbed space. Applying this to the current problem we obtain [4]:

$$\Delta\lambda \propto \lambda \frac{\int_{-\infty}^{\infty} \int_{-\infty}^{\infty} n(x, y) \Delta n(x, y) |\mathbf{E}(\mathbf{x}, \mathbf{y})|^2 dx dy}{\int_{-\infty}^{\infty} \int_{-\infty}^{\infty} n^2(x, y) |\mathbf{E}(\mathbf{x}, \mathbf{y})|^2 dx dy} \quad (3.8)$$

in which terms related to higher powers of the perturbation are omitted. Here, $\Delta n(x, y)$ is the perturbation of the refractive index profile due to the protein layer, such that the numerator is only non-zero in the protein layer. In order for the model to answer to a range of dielectric perturbations which surpasses the range normally governed by this function we altered the fields by using not the harmonic fields of the unperturbed waveguide profile, but by using the field profiles of the waveguide with the protein layer already in place.

To obtain these field profiles, we start with the method of Marcatili, as described in [6]. The cross section of the three-dimensional rectangular waveguide which we will use to derive the model is depicted in Figure 3.5. In comparison to the Marcatili method we have added a thin protein layer. The starting point of the Marcatili method is the subdivision of the modes into TE-like and TM-like

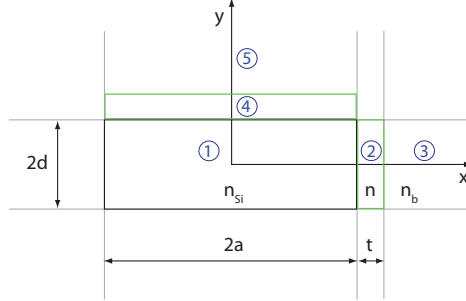


Figure 3.5: Waveguide cross section used in the adapted method of Marcatili, presented here to obtain the field profiles in the zones indicated. The zones 2 and 4 indicate the protein layer.

modes. Whereas this method starts from a rectangular profile which has a mirror symmetry in the $y=0$ plane, this is not the case for the SOI material system, where the waveguide rests on an oxide substrate. However, we have seen in chapter 2 that the subdivision in TE-like and TM-like modes still holds. This suggests the following field profiles for the first TE-like mode:

$$E_x = \begin{cases} A \cos(k_x x) \cos(k_y y - \psi) & \text{zone 1} \\ A \cos(k_x a) \cos(k_y y - \psi) e^{-\gamma_x(x-a)} \frac{n_{Si}^2}{n^2} & \text{zone 2} \\ A \cos(k_x a) \cos(k_y y - \psi) e^{-\gamma_x a} e^{-\gamma_x^*(x-a-t)} \frac{n_{Si}^2}{n_b^2} & \text{zone 3} \\ A \cos(k_x x) \cos(k_y d - \psi) e^{-\gamma_y(x-d)} & \text{zone 4} \\ A \cos(k_x x) \cos(k_y d - \psi) e^{-\gamma_y d} e^{-\gamma_y^*(y-d-t)} & \text{zone 5} \end{cases} \quad (3.9)$$

The fractions n_{Si}^2/n^2 and n_{Si}^2/n_b^2 come from the boundary condition that the normal component of the displacement field $\mathbf{D} = \epsilon\mathbf{E}$ has to be continuous across both interfaces. We have added the phase factor ψ since the structure is not symmetric in y -direction. The transverse wavenumbers k_x , k_y , γ_x , γ_y , γ_x^* and γ_y^* relate to the propagation constant β as

$$\begin{cases} \beta^2 + k_x^2 + k_y^2 = k^2 n_{Si}^2 & \text{zone 1} \\ \beta^2 - \gamma_x^2 + k_y^2 = k^2 n^2 & \text{zone 2} \\ \beta^2 - \gamma_x^{*2} + k_y^2 = k^2 n_b^2 & \text{zone 3} \\ \beta^2 + k_x^2 - \gamma_y^2 = k^2 n^2 & \text{zone 4} \\ \beta^2 + k_x^2 - \gamma_y^{*2} = k^2 n_b^2 & \text{zone 5} \end{cases} \quad (3.10)$$

Solving the integrals in the denominator of equation 3.8 in zones 2 and 4, and those in the numerator in zones 1-5 with the fields given in equation 3.9 gives us

the following solution:

$$\Delta\lambda(n, t) = B \frac{(n - n_b)n f_p(t, n)}{1 + n^2 f_p(t, n) + n_b^2 f_b(t, n)} \quad (3.11)$$

Here, contributions of the protein layer and the bulk fluid are denoted by the subscript p and b , which each have a term coming from the top surface of the waveguide and a term coming from the side wall of the waveguide:

$$f_p(t, n) = E_{H,0}^2 \frac{1 - e^{-2\gamma_x t}}{\gamma_x} + E_{V,0}^2 \frac{1 - e^{-2\gamma_y t}}{2\gamma_y} \quad (3.12)$$

$$f_b(t, n) = \frac{E_{H,t}^2}{2\gamma_x^*} + \frac{E_{V,t}^2}{2\gamma_y^*} \quad (3.13)$$

The constant factors are defined as

$$\begin{cases} E_{H,0} = \frac{A}{A_{res}} \left(\frac{\cos(2\psi) \sin(2k_y d)}{2k_y} + d \right) \cos(k_x a) \frac{n_{s,i}^2}{n^2} & \text{zone 2} \\ E_{H,t} = E_{H,0} \frac{n^2}{n_b^2} e^{-\gamma_x t} & \text{zone 3} \\ E_{V,0} = \frac{A}{A_{res}} \left(\frac{\sin(2k_x a)}{2k_x} + a \right) \cos(k_y d - \psi) & \text{zone 4} \\ E_{V,t} = E_{V,0} e^{-\gamma_y t} & \text{zone 5} \end{cases} \quad (3.14)$$

The constant A_{res} is the integration of the numerator in equation 3.8 in the core and substrate.

For this three dimensional model to fit correctly, we need to introduce 5 parameters: ψ , A/A_{res} , k_x , β and proportionality constant B . However, we have seen that this model is not very robust to fitting over a different range of waveguide profiles used in various experiments. Furthermore, it would be beneficial to reduce the amount of fitting parameters. As such we propose a pseudo-3D model based on this 3D model by assuming the waveguide to behave as 2 2D slabs as far as the protein layers are concerned. This means technically that for zone 2 and zone 3, k_y is set to 0 and for zone 4 and 5, k_x is set to 0. This relaxes the fitting of the wavenumbers to just a fitting of β :

$$\begin{cases} \kappa = \sqrt{k^2 n^2 - \beta^2} & \text{zone 1} \\ \gamma_x = \sqrt{\beta^2 - k^2 n^2} & \text{zone 2} \\ \gamma_x^* = \sqrt{\beta^2 - k^2 n_b^2} & \text{zone 3} \\ \gamma_y = \sqrt{\beta^2 - k^2 n^2} & \text{zone 4} \\ \gamma_y^* = \sqrt{\beta^2 - k^2 n_b^2} & \text{zone 5} \end{cases} \quad (3.15)$$

However, to maintain a differentiation between the two dimensions, the parameters ψ and A/A_{res} are replaced by $A_{H,0}$ and $A_{V,0}$ which are equivalent to the

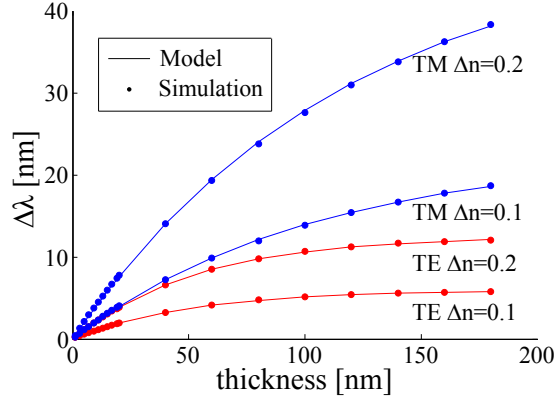


Figure 3.6: Simulations of the wavelength shifts for both modes in function of the thickness of the protein layer for various refractive indices of this layer. The fitting of this data to the model results in an R^2 value of 0.9998.

amplitude of the field in the waveguide for respectively x and y directions:

$$\begin{cases} E_{H,0} = A_{H,0} \cos(\kappa a) \frac{n_{S_i}^2}{n^2} & \text{zone 2} \\ E_{H,t} = E_{H,0} \frac{n^2}{n_b^2} e^{-\gamma_x t} & \text{zone 3} \\ E_{V,0} = A_{V,0} \cos(\kappa d) & \text{zone 4} \\ E_{V,t} = E_{H,0} e^{-\gamma_x t} & \text{zone 5} \end{cases} \quad (3.16)$$

For this pseudo-3D model, equations 3.11-3.13 are still valid, but we use the newly defined wavenumbers and amplitudes as defined by equations 3.15 and 3.16. A similar description provides the equations for the TM-like mode, where one must take caution to change the boundary conditions accordingly. The fitting parameters are (for each polarization) β , $A_{H,0}$, $A_{V,0}$ and B . The TE and TM shifts are fitted together. A standard metric to evaluate a fit is the R^2 metric. This number will approach 1 as the fit improves compared to fitting the data by taking its average:

$$R^2 = 1 - \frac{SS_{res}}{SS_{mean}} \quad (3.17)$$

$$SS_{res} = \sum (y_i - f_i)^2 \quad (3.18)$$

$$SS_{mean} = \sum (y_i - \bar{y})^2 \quad (3.19)$$

Here, y_i are the simulated points and f_i are the corresponding points as determined by the model.

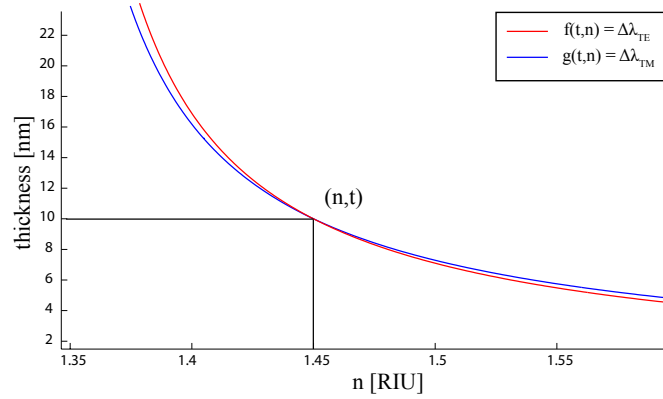


Figure 3.7: Visualization of the solving protocol by plotting $f(t, n) = \Delta\lambda_{TE}$ and $g(t, n) = \Delta\lambda_{TM}$, with the shifts corresponding to the shifts obtained for a layer with thickness 10 nm and refractive index 1.45.

We have fitted this model to Fimmwave simulations and obtained a near-perfect fit with a R^2 metric of 0.999992 on a span $t = 0 - 20$ nm and $\Delta n = 0 - 0.2$ RIU. It is absolutely necessary for the fit to have this high of an accuracy as this R^2 corresponds to an average fitting error on TE wavelength of 1-2 pm. In contrast, the heuristic model described by equations 3.6-3.7 has a R^2 value of 0.9999 [4]. Furthermore, this polynomial model is only valid for small thicknesses. Since it is a second-order polynomial with 7 total fitting parameters, it is unable to follow the saturating curve of the wavelength shifts in function of thickness for larger thicknesses. The model described here, due to its physical origin, does retain a good shape even when the thickness is increased to 200 nm, as can be seen on Figure 3.6, even though the TE mode saturates for a thickness over 100 nm.

After fitting the model we can solve the measured wavelength shifts $\Delta\lambda_{TE}$ and $\Delta\lambda_{TM}$ via the obtained functions $f(t, n)$ and $g(t, n)$ to t and n . By setting f and g equal to these shifts, we obtain two implicit functions in t and n which are plotted in Figure 3.7 for a layer with thickness of 10 nm and refractive index of 1.45. The intersection point of both curves corresponds to the solution of the experiment.

3.5 Calibration protocol

3.5.1 Off-line imaging techniques

To extract t and n from $(\Delta\lambda_{TE}, \Delta\lambda_{TM})$ via simulations done on the waveguide profile of Figure 3.3, we need to obtain the width (W) and height (H) of the cross section, as well as the refractive index of the buffer (n_b). As far as the geometry of the waveguide cross section goes, we have assessed several measuring techniques. These are illustrated in Figure 3.8, where all images are taken from a microring resonator with a cross section with nominal dimensions of 480 nm x 220 nm on the same SOI chip. On the top row we see two images taken with a FIB-SEM tool. On the left, the coupling section of the microring resonator is imaged after it has been sliced with the focused ion beam. To facilitate a clean cross sectioning, a platinum layer is deposited first to protect the waveguides. The ions remove the material such that the cross section of the SOI waveguide becomes apparent. Figure 3.8(a) shows the coupling section from a top-down angled view after slicing took place. The indicated region is the cross section of the coupling section, of which a close-up (after tilting the sample) is given in Figure 3.8(b). The images themselves are taken with a SEM-column, installed in the same tool. The image shows the asymmetric coupling section of the microring resonator, with a ring waveguide which is 452 nm wide and 223 nm high, with an accuracy of 5-10 nm. On the second row of Figure 3.8 we see an image taken of the waveguide with an atomic force microscope (AFM), which scans the topography of a 2D section of the chip. The waveguide is clearly visible in Figure 3.8 (c), which shows the height in function of the position. For the two indicated lines, the height is shown in Figure 3.8 (d). The height is measured to be 300 nm with a half-way width of 800 nm. We conclude that the step size of the waveguide is too high to be measured accurately with an AFM tool. At the bottom of Figure 3.8, the profile along a line as measured by a stylus profilometer is shown. This is a mechanical technique which scans the height with a stylus tip size of 2.5 μm radius. A zoom of the indicated feature, representing the waveguide is shown on the right. The measured height, averaged over 3 microrings on the sensing chip, with 2 measurements per microring, equals 221.7 nm with a variance of 1 nm. To measure the width accurately, the tip size is too large however.

We see that the height as measured by FIB-SEM and by the profilometer are similar and within the fabrication tolerances of 10 nm on the thickness of the guiding silicon layer. For the width, only the FIB-SEM technique provides realistic values. These diverge more from the designed width since they are very sensitive to the illumination dose during the lithographic process. For this specific wafer the option was chosen to sweep the illumination dose over one axis of the wafer. A chip coming from the left-end of the wafer can thus behave differently from a

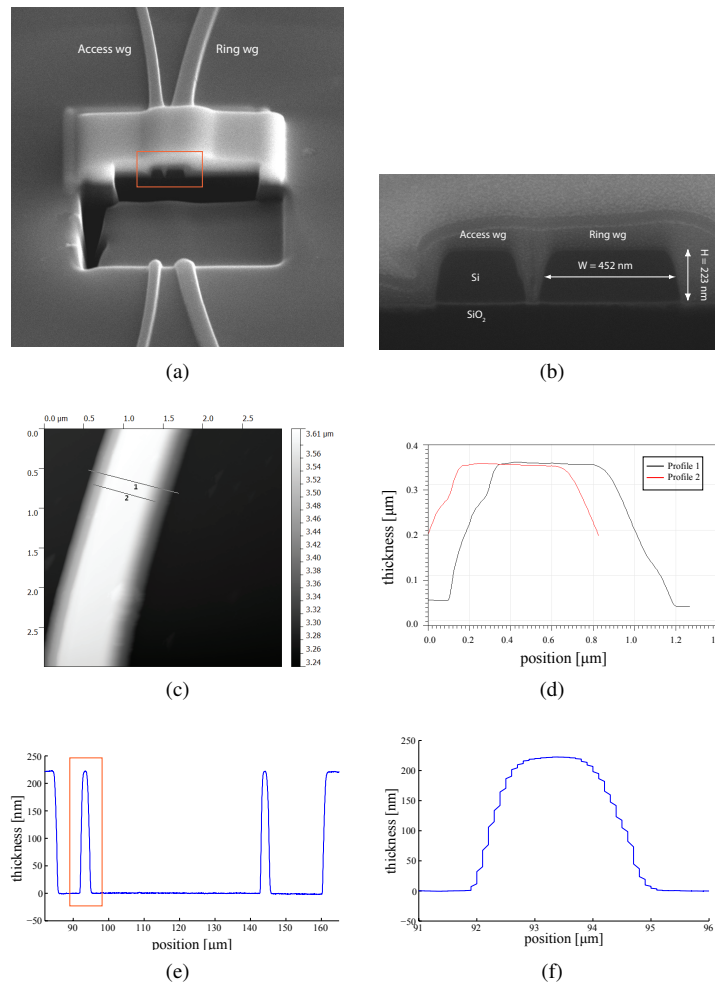


Figure 3.8: Various techniques to retrieve the width and height of the waveguide profile. All images are taken from the same SOI chip. (a) Focussed ion beam image, tilted perspective after the ions have bombarded the coupling section of microring resonator and (b) zoom on the indicated region. (c) Atomic force microscopy image indicating the height profile of a 2D section of the chip where a waveguide runs with (d) height profile of the two indicated lines. (e) Stylus profilometer profile of a series of adjacent waveguides and (f) zoom on the indicated region.

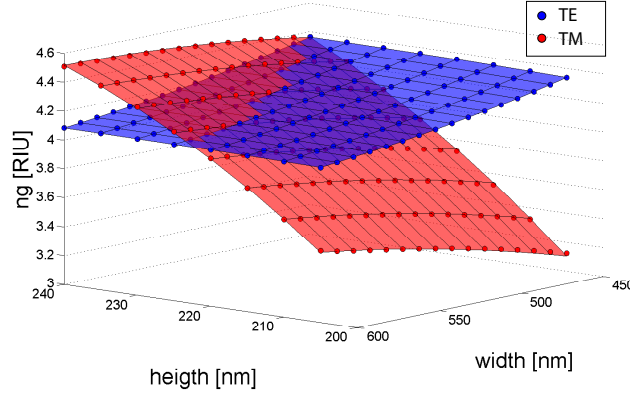


Figure 3.9: Simulated group indices of a rectangular waveguide, showing a high dependency on one of the spatial coordinates for both modes.

chip coming from the right-end. This gives a wider spread on the characteristics of the circuits, offering more data for the designer, which is beneficial in early-stage development of new structures.

Calibrating the microring sensors with these techniques poses thus a few problems. Most obvious is the practical aspect. The FIB-SEM technique is a destructive one and therefore not usable for pre-experimental calibration. Measuring the ring after the experiment is possible but quite cumbersome and means removing the PDMS microchannels from the SOI chip. Some PDMS debris that remains on the chip can be detrimental for the FIB-SEM vacuum chamber. To avoid the sectioning, effort has been put in relating the width of the microring as measured by the SEM top view (without sectioning the waveguides) to the width measured of the cross section after bombardment with ions. Measurements showed however that the SEM top view measurements were not accurate enough. Second, the accuracy offered by these techniques is sub-par for the retrieval of t and n , as the sensitivity of the resolved thickness to the width and height of the waveguide is too high.

3.5.2 In-line self-calibration

To alleviate these problems we can determine the width and height of the cross section by using the microring resonator itself, in-line with the experiment. These can be determined by measuring the FSR of the TE and TM mode [3]. To stay as close as possible to experimental conditions, this is done when water is covering the microring sensor. The refractive index of water is well-researched and was determined to be 1.316 at 1550 nm in [7]. The following equation is used to obtain

the group index (n_g) of both modes from the measured FSR:

$$FSR = \frac{\lambda^2}{n_g L} \quad (3.20)$$

Here, L is the length of the microring cavity. Using Fimmwave, we construct surfaces $n_{g,TE}(W, H)$ and $n_{g,TM}(W, H)$ of the cross section on Figure 3.3 with n_b equaling the refractive index of water and fit these to a second-order model in (W, H) . Since we are using the same simulation method as will be used in a later stage to obtain t and n , we are effectively calibrating the system instead of determining the exact width and height of the cross section. For a parameter space spanning 25 nm for H and 100 nm for W , we obtained a goodness-of-fit of 0.99997 for TE and 0.99991 for TM. This high goodness-of-fit is explained by the high linearity of the group index of the TE mode in W , while the group index of the TM mode is highly linear in H . This can be observed in Figure 3.9. Physically, these high linearities to either W or H originate from the orthogonality of both modes.

When these curves are obtained, the measured FSR of both modes can be used to determine W and H . In this way the width and height of the cross section of the same microring that was measured by FIB, AFM and profilometer in the previous section, are determined to be 443.8 nm and 209.6 nm. Both differ about 10 nm with the measured values by the FIB-SEM, which is also the accuracy of this tool. Note that W and H are set by the calibration procedure in such a way so as to get accurate results for t and n , and are only abstractions of the true geometry (which could e.g. exhibit slanted sidewalls). The deviation in waveguide height with the measured height for example, shows that the simulation software needs to make a small correction so as to adapt the measured group index to the simulated one and make the simulations respond in the same way as the real microring will.

The resolution of the calibration is determined by how accurate n_g , or equivalently, the FSR can be determined. The noise that is present in the measured wavelength positions will propagate to the determination of W and H . Figure 3.10 illustrates this noise by plotting the width and height during a 10 minute streaming of water over the microring used in the BSA experiment of section 5.2. It shows a mean width and height of the ring waveguide of $W = 491.7$ and $H = 210.7$. The 3σ deviations during the 10 minutes where water is flown over the sensor amount to 98 pm for W and 26 pm for H . These uncertainties on the simulation parameters imply an uncertainty on the determination of the thickness and refractive index of the protein layer. Both 3σ deviations for W and H were used to calculate a maximum error on thickness of 20 pm and a maximum error on refractive index of 0.62 mRIU.

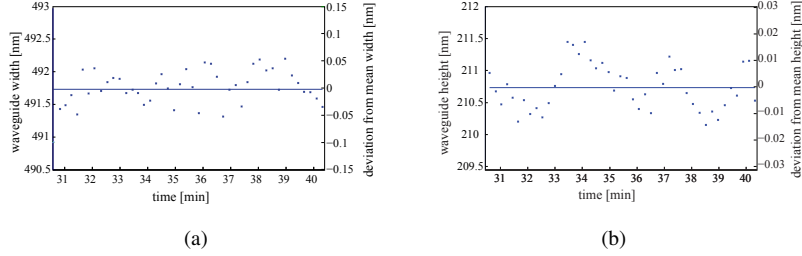


Figure 3.10: By measuring the FSR of both modes during a water phase prior to the following BSA experiment, the (a) width of the ring waveguide was determined with a mean value of 491.7 nm. (b) The height was calculated to be 210.7 nm.

After the calibration of the waveguide cross section, the index of the bulk fluid n_b also needs to be determined. This is done by measuring the shift of the TE mode during a change from water to the unknown bulk fluid. A simulation with the just-determined cross section can be done to estimate the sensitivity of the TE mode to changes in the refractive index of a bulk fluid. An example is given for the waveguide dimensions as calibrated for in the BSA experiment of section 5.2 in Figure 3.11(a), where the resonance wavelength shift due to a change in buffer refractive index with respect to water is shown. The high linearity for small changes is visible and amounts to a sensitivity of $\frac{\partial \lambda}{\partial n_{buffer}} = 57 \frac{nm}{RIU}$. This is similar to the experimentally verified sensitivity in [8]. The bulk shift from water to buffer (PBS) is 25 pm, as shown on Fig. 3.11(b). The value of n_b is then calculated using the following formula and amounts to 1.3163.

$$n_b = n_{water} + \frac{\Delta \lambda_{TE,b}}{\frac{\partial \lambda_{TE}}{\partial n_b}} \quad (3.21)$$

We conclude by illustrating the calibration protocol schematically in Figure 3.12. After the chip has been installed in the measurement setup, the calibration protocol starts with a three-step sequence of deionized (DI) water, running buffer and DI water. When water is flowing over the sensor, the free spectral range (FSR) of both modes is extracted from the spectra, to determine the dimensions of the cross section. Next, the shift of a resonance wavelength of the TE mode when the fluid is switched from water to buffer provides the refractive index of the buffer. Directly afterwards, the actual experiment can start.

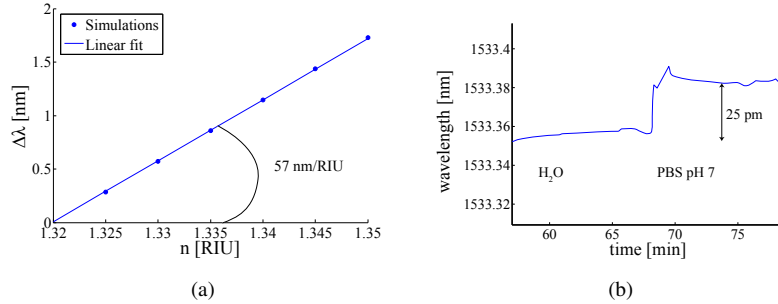


Figure 3.11: (a) Simulation of the wavelength shift of the TE mode in function of the refractive index of a cladding layer with waveguide dimensions of $W = 491$ nm and $H = 210$ nm. The wavelength shift is simulated with respect to a buffer with $n_{buf} = 1.32$. (b) Shift of the TE resonance when switching from water to buffer (PBS in this case), as measured in the BSA experiment.

3.6 System performance

In the discussion on detection limits and system performance we will often traverse the system from the sensor end, where the analytes effectively bind to the microring, to the user end, where a signal is produced in the form of a binding curve. Everything in between can be called the system and the terms sensor end and user end will often be used to facilitate the discussion.

3.6.1 Detection limit

The most indicative metric to evaluate biosensing systems is the limit of detection (LOD). It is defined as the smallest change which can accurately be detected by the system. Contrary to the sensitivity, which is often used in literature as a defining metric of the system, it also takes the noise of the system into account. Only signals which can be distinguished from the noise are accounted for, reflecting a practical measurement. The detection limit is in this sense a relative metric, while the sensitivity is an absolute one: the sensitivity merely tells us the size of the signal transduction. The preferred way to determine the LOD is at the user end of the system. For a single polarization system, this can be done by means of a dose-response curve of the molecules that need to be detected. This is largely influenced by conditions other than optics: affinity of the chemical probes, quality of the surface coverage by these chemical probes, biological matrix in which the analytes are suspended, diffusion properties of the analyte to the chip surface, etc. An overview of label-free detection technologies by Qavi et al. [9] shows that these detection limits are also not reported in a standard way in scientific literature. They are expressed in molarity (pM), surface coverage (pg mm^{-2}), concentration

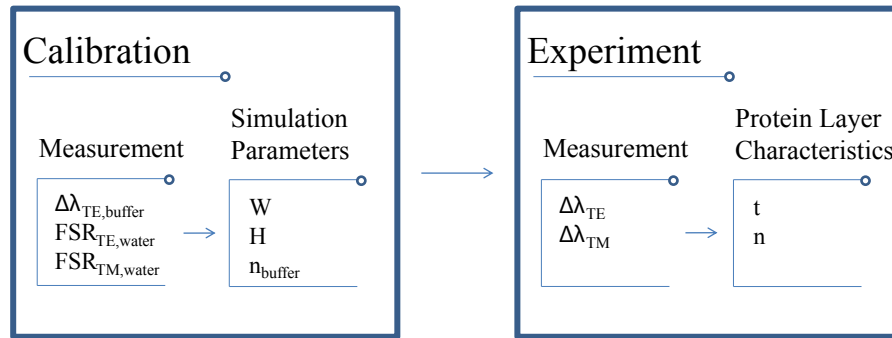


Figure 3.12: Schematic diagram of the calibration and the actual experiment. The calibration measurements are done before the measurements for the actual experiment start. They are used to obtain the simulation parameters. These simulations finally determine the model to solve the experimental measurements to the characteristics of the protein layer.

(ng mL^{-1}), mass (fg), etc.

In this section we will try to evaluate the detection limit of the system independent of these chemical and biological conditions. The simulations that will be performed will make abstraction of the biology and chemistry by representing the layer as a uniform layer with a certain thickness and refractive index. Although this does not quantify the amount of analytes that can actually be detected, it does provide a metric which contains the contributions of the sensor and the system to the user-end detection limit and as such sets up a way to compare sensors and systems in a fair and complete way.

3.6.1.1 Detection limit of a single polarization microring system

By virtue of calibration, the system can be represented by the transduction proportionality constant S that relates the measured wavelength shift $\Delta\lambda$ with a change in a single parameter. This single unknown parameter can e.g. be the concentration or the thickness t of a bound layer, at which point we must assume the refractive index n :

$$\Delta\lambda_{TE} = S \cdot t \quad (3.22)$$

This proportionality constant is also called the sensitivity. The limit of detection relates the readily-measurable minimal detectable shift at the user end of the system to the physical property this shift represents at the sensor end of the system. This means that it traverses the system in reverse direction. In this system view, we

see that equation 3.22 tells us that the system is completely represented by a single scalar S . The definition of LOD is hence trivial since the action of reversing is a simple division:

$$LOD = \frac{\Delta\lambda_{min}}{S} \quad (3.23)$$

We define $\Delta\lambda_{min}$ via the standard deviation of the wavelength noise on a binding curve $\sigma_{\Delta\lambda}$. There are various contributions to this wavelength noise from different elements in the measurement setup, such as temperature fluctuations, laser instability while sweeping the wavelength, thermal noise and shot noise from the camera capturing the light. To quantify the noise of our system, we have streamed phosphate buffered saline (PBS) at 30 $\mu\text{l}/\text{min}$ over the sensor array for 11 minutes, gathering 47 resonant wavelengths per mode. We have quantified the noise as the standard deviation on a linear curve through these measurements, to correct for time-dependent linear drift. We have experimentally obtained this noise as 220 fm for the TM mode and 246 fm for the TE mode. This is in good agreement with the noise determined in [10] for a TE mode, where a similar microring and lithographic fabrication process is used. For ease of calculation, we will use 220 fm noise on both modes in the following.

3.6.1.2 Detection limit of a system with two unknowns

The limit of detection for a system with two unknowns (t and n) is less straightforwardly defined as for a system with one unknown. We chose to define the system by using Maxwell's equations to obtain the non-linear analytical functions f and g , linking the measurable quantities ($\Delta\lambda_{TE}$ and $\Delta\lambda_{TM}$) with the unknown quantities t and n . Instead of linearizing this system such that an inverse can be determined, providing us with a similar LOD procedure as for the system defined by a single unknown, we chose a different approach which does not give rise to linearization errors. We determine the limit of detection on t and n by adding and subtracting the uncertainties on the measured wavelengths to the exact calculated shifts and checking what the influence is on the solved t and n :

$$\Delta\lambda_{TE} \pm \sigma_{\Delta\lambda} = f(n, t) \quad (3.24)$$

$$\Delta\lambda_{TM} \pm \sigma_{\Delta\lambda} = g(n, t) \quad (3.25)$$

These 4 sets of 2 equations provide 4 unique solutions in the (t, n) -space that delineate the error area as indicated in Figure 3.13. Mind that the curves in this figure are rotated with respect to their real orientation for illustrative purposes. They do not represent the real slope of f and g , as opposed to the curves in Figure 3.7. We define the limit of detection on thickness $LOD_t(t, n)$ and the limit of detection on refractive index $LOD_n(t, n)$ as the maximum error both on t and n that rolls out of this procedure.

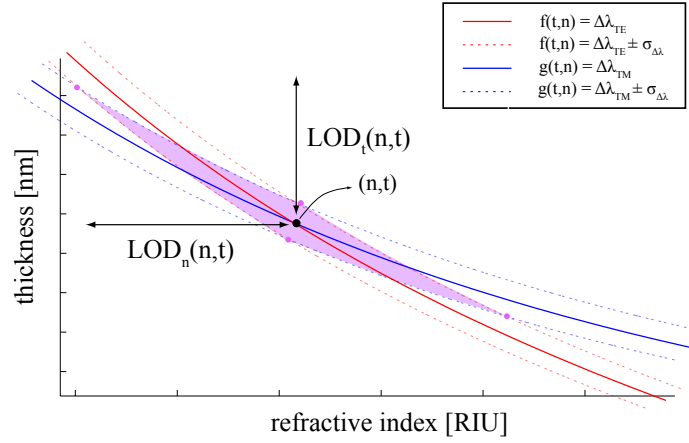


Figure 3.13: Visualization of the limit of detection in thickness and refractive index. The solid red and blue lines represent the curves that intersect in the solution (t,n) . The dotted curves represent these curves as measured under the influence of noise such that the purple area delineates possible solutions in a noisy measurement. The maximum error on t and n obtained from this collection of solutions is defined as the limit of detection on t and n .

Mind that the slope of the f and g curves is changed for illustrative purposes.

Due to the nonlinearity of the system, this limit of detection is dependent on the specific layer, as is illustrated by the spreads in Figure 3.14. To obtain this figure, a certain (t,n) -couple is fed into the calibrated model, which returns a $(\Delta\lambda_{TE}, \Delta\lambda_{TM})$ -couple. After adding noise on both shifts, sampled from an equidistant 2D space of $[-220 \text{ fm}, 220 \text{ fm}] \times [-220 \text{ fm}, 220 \text{ fm}]$, the noisy shifts are calculated back to (t,n) -couples which are all plotted, rendering the spreads. This procedure is done for 12 different initial (t,n) -values, with $t \leq 10 \text{ nm}$. It is observed that the spread increases if the refractive index of the layer approaches the refractive index of the bulk fluid and if the layer thickness decreases. In a realistic measurement however, the refractive index of a biomolecule is substantially higher (1.45) than the one of aqueous bulk fluids (close to 1.316, the refractive index of water), such that for a reasonable amount of deposited molecules, the refractive index of the layer will be higher as well. To provide a limit of detection metric which is valid for the system and not for a single point, we hence average out $LOD(t,n)$ over a range of realistic layers. Averaging out the maximum spread for layers in the 2D-space of $n = 1.41 - 1.46 \text{ RIU}$ and $t = 2 - 9 \text{ nm}$ gives a limit of detection of 41 pm on thickness and 1.1 mRIU on refractive index.

The resolution on t and n of the system can also be estimated experimentally.

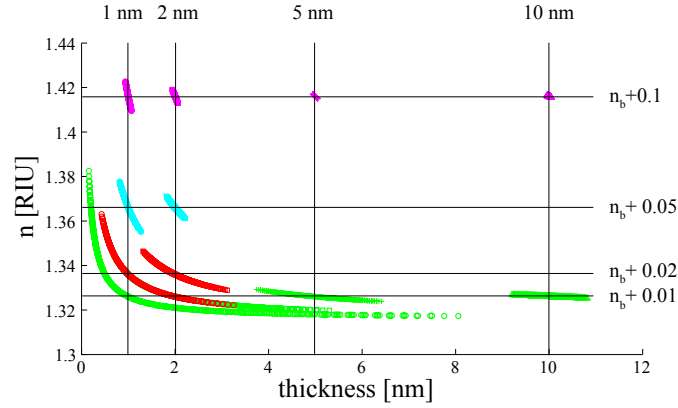


Figure 3.14: Simulated spread on solved thickness and refractive index, due to noise on TE and TM wavelength positions. A certain (t,n) -couple is fed into the calibrated model, which gives a $(\Delta\lambda_{TE}, \Delta\lambda_{TM})$ -couple. The (t,n) -couples are indicated by the intersections of the solid vertical and horizontal lines. n_b is the refractive index of water, 1.316. After adding noise on both shifts, sampled from an equidistant 2D space of $[-220 \text{ fm}, 220 \text{ fm}] \times [-220 \text{ fm}, 220 \text{ fm}]$, the noisy shifts are calculated back to (t,n) couples which are all plotted, rendering the spreads. The limits of this sampling space (220 fm) represent the experimentally determined standard deviation on the resonance wavelengths. Different colors and markers represent different clusters.

To do so, we have used the t and n profiles as generated by the polymer experiment presented in chapter 6. The standard deviation on the thickness, refractive index and mass after the last cycle of polymer adsorption have been determined. At this point, a thickness of 7.5 nm and a refractive index of 1.45 is measured. The thickness and the refractive index of the stack when water was flowing over the chip had a 3σ value over time of 67 pm and 0.0011 RIU over 24 points. This is illustrated on Figure 3.15. When a (t,n) -couple of (7.5,1.45) is inserted in the simulation routine presented in Figure 3.14, we compute a spread of 30 pm on t and 0.5 mRIU on n . As such, the measured σ and the simulated spread correspond very well. Since the resolution on thickness is lower than 1 Å, subtle conformational changes are detectable [11].

The spreads of the solutions in Figure 3.14 show that the limit of detection is heavily determined by the fact that these spreads are organized along a line, meaning that the thickness and refractive index variations are correlated. This cripples the accuracy as opposed to uncorrelated noise, represented by a disk. Most optical detection principles face this problem concerning the disentanglement of t and n , since the evanescent fields respond to the optical thickness $t \cdot n$. Therefore, it can be instrumental to have a look at the uncertainties on the deposited mass,

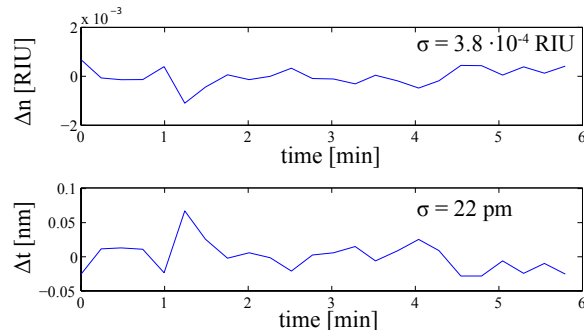


Figure 3.15: Experimentally determined noise as the standard deviation on thickness and density during the last 5 minutes of the polymer experiment in chapter 6. At this point, 5 bilayers were adsorbed to the silicon surface, which had a total thickness of 7.5 nm and a refractive index of 1.45

as this scales with the product of t and n and is depicted on Figure 3.16 (a). The standard deviation of the mass is determined as 0.6 pg/mm^2 for the same 7.5 nm-thick stack, while for a stack comprising of just a single layer of only 1.84 nm thick, the standard deviation only increases slightly to 1.3 pg/mm^2 , as can be seen on Figure 3.16 (b). The fact that the measurement does not drown in noise for a stack smaller than 2 nm is quite remarkable and a unique feature of this technology. In comparison, Ramos et al. analyzed the same polymer bilayer system as we have (PAH/PSS) with ellipsometry and an experimental noise of 10 pg/mm^2 is reported [12].

3.6.2 Thinnest detectable layer

Where the limit of detection informs us about the smallest change in a layer that can be observed for bilayers within a certain range of dimensions, it does not inform us about the thinnest layer in absolute sense that can be detected. This metric can prove valuable to assess what the minimum size of molecules is that can be studied by this technology or if it is possible to study interface layers close to the substrate when a material is deposited on top of the silicon. From the spreads we have seen that, as a layer decreases in size, it is progressively harder to determine its size or refractive index. We define a metric for this as the thickness of the layer for which the maximum relative error is less than 10 percent. This maximum error is $LOD_t(n, t)$ as defined via Figure 3.13. Plotting a contourplot of $LOD_t(n, t)/t$ in logscale for a 2D grid of refractive indices and thicknesses renders Figure 3.17. Here, the “-1”-contour indicates the (t, n) -couples for which the relative error is exactly 10 %. The y-axis is the refractive index increase of the layer compared to water. Thus, we have determined the thinnest layer which is reasonably dense

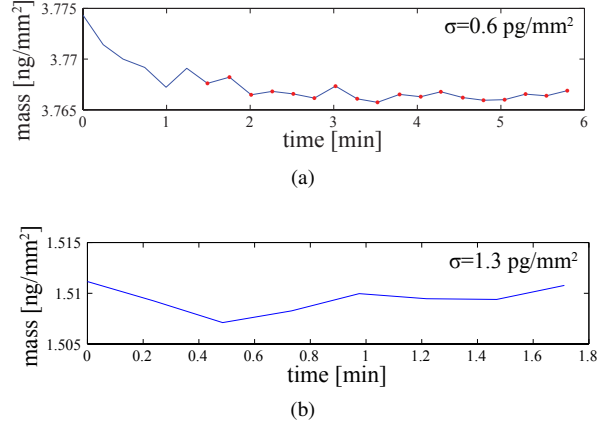


Figure 3.16: (a) Experimentally determined noise as the standard deviation on deposited mass during the last 5 minutes (red dots) of the polymer experiment of chapter 6 while water was streaming over the sensor. At this point, 5 bilayers were adsorbed to the silicon surface, which had a total thickness of 7.5 nm and a refractive index of 1.45. (b) Experimentally determined noise from the same experiment but when only the first layer (PEI layer) had adsorbed to the stack, with a thickness of 1.84 nm and a refractive index of 1.465. The standard deviation is determined on 8 measurement points, during 2 minutes.

($n = n_w + 0.1 = 1.416$) and can be detected with a relative error on thickness smaller than 10% to be only 0.75 nm thick. In comparison, Tiberg et al. have determined that a surfactant layer of 4 nm can be determined with a relative error of 10% on t and n with ellipsometry [13]. This is however the most accurate measurement we have found in literature. More recent studies consistently state that layers smaller than 10 nm can not be resolved adequately by ellipsometry [12, 14–16].

3.6.3 Paths to improvement

Figure 3.13 provides a visual way to gain insight in improving the limit of detection by reducing the error zone. There are two distinct ways to achieve this. Either we reduce the noise and leave the system, represented by the shape of the curves, intact, or we tackle the system and try to adjust the shape or orientation of the TE and TM curves in the (t, n) solution plane.

We will try to assess to what degree the LOD can be influenced via the second method. If the curves can be rotated with respect to one another such that the angle in between the curves at the intersection point grows, simple geometry shows that the error zone would reduce in size. Since the angle is small it can be approximated

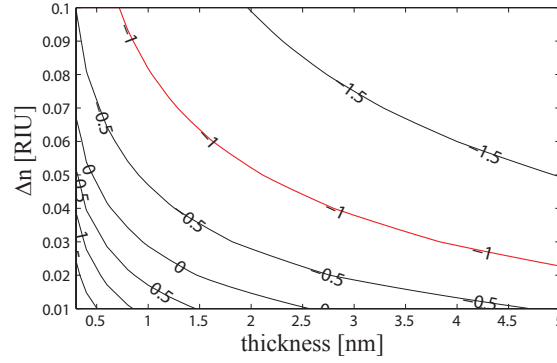


Figure 3.17: Contour plot in log scale of the relative maximum error on thickness. It can be seen that the “-1”-contour intersects with the $\Delta n = 0.1$ -line for $t = 0.75$. This means that a layer thinner than 0.75 nm can no longer be determined with a relative error smaller than 10 %

by:

$$\alpha = \left. \frac{dn}{dt} \right|_{TE} - \left. \frac{dn}{dt} \right|_{TM} \quad (3.26)$$

However, we do not have an explicit defined expression for n in function of t to easily perform this derivative on. The implicit function theorem provides a way out. It states that if a function F is defined on an open disk containing (a,b) such that $F(a,b) = 0$, $F(x,y)$ defines y as a function of x near (a,b) and:

$$\frac{dy}{dx} = - \frac{\frac{\partial F}{\partial x}}{\frac{\partial F}{\partial y}} \quad (3.27)$$

We define functions F_{TE} and G_{TM} as

$$F_{TE}(t,n) = f_{TE}(t,n) - \Delta\lambda_{TE} \quad (3.28)$$

$$G_{TM}(t,n) = f_{TM}(t,n) - \Delta\lambda_{TM} \quad (3.29)$$

such that F and G are equal to zero at the solution (t,n) . Thus we obtain for α

$$\alpha = \frac{\frac{\partial f_{TE}}{\partial t}}{\frac{\partial f_{TE}}{\partial n}} - \frac{\frac{\partial g_{TM}}{\partial t}}{\frac{\partial g_{TM}}{\partial n}} \quad (3.30)$$

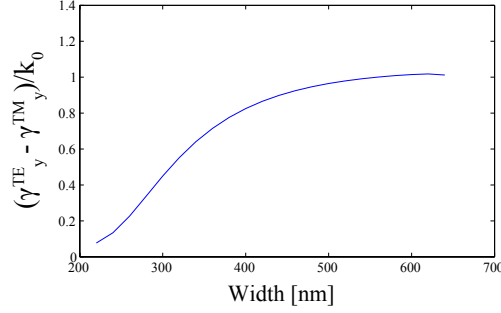


Figure 3.18: Plot of Equation 3.33 for a planarized waveguide with rectangular cross section with a height of 220 nm

As an example, we can evaluate this for the case of a planarized waveguide which thus only has a layer at the top of the waveguide. The functions f_{TE} and g_{TE} are given by equation 3.11. In the planarized case, only one term in $f_p(t, n)$ remains and for small perturbations, we can approximate the denominator in f and g by a constant. In this small signal case, we adhere to the strict perturbation theory such that the field amplitudes are those of the unperturbed waveguide and hence disappear in the following fraction:

$$\frac{\frac{\partial f_{TE}}{\partial t}}{\frac{\partial f_{TE}}{\partial n}} = \frac{n(n - n_b)e^{-2\gamma_y^{TE}t}}{(2n - n_b)(1 - e^{-2\gamma_y^{TE}t})/(2\gamma_y^{TE})} \quad (3.31)$$

Approximating the exponentials by their first order Taylor expansion around $t=0$, we obtain the following simplified expression for α :

$$\alpha \approx \frac{n(n - n_b)}{(2n - n_b)} \cdot (\gamma_y^{TE} - \gamma_y^{TM}) \quad (3.32)$$

The part which is dependent on the waveguide structure boils down to, with $k_x = 0$:

$$\sqrt{n_{eff,TE}^2 - n_w^2} - \sqrt{n_{eff,TM}^2 - n_w^2} \quad (3.33)$$

Plotting this in function of the width of the waveguide cross section for a height of 220 nm results in Figure 3.18. We see that for this simplified example for small thicknesses, that for waveguides with a width in the region of interest $361 \text{ nm} < W < 586 \text{ nm}$, the slope is very flat and so not much improvement can be expected by changing the waveguide dimensions. However, looking at equation 3.31, where

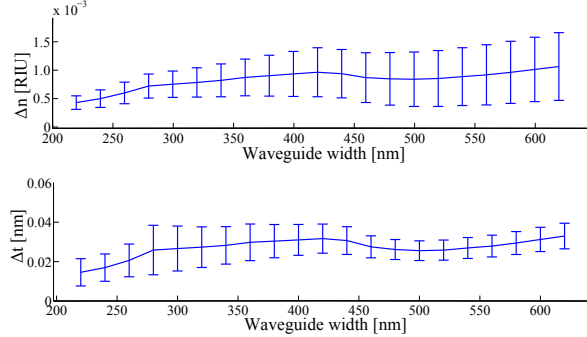


Figure 3.19: Limit of detection on determination of t and n for various widths of the waveguide, with a fixed height of 220 nm.

the exponentials are left intact, we see that if γ^{TM} would approach to 0, this expression would grow infinitely large. If at the same time γ^{TE} remains limited, α would change considerably. For the SOI wire waveguide geometry, the TE mode always has a higher n_{eff} than the TM mode, such that for decreasing width the TM mode approaches cut-off, while the TE mode remains guided. Unfortunately, for γ to approach 0, the refractive index of the substrate (oxide in this case) would have to be lower than the refractive index of the upper cladding, which is water. Furthermore, one can expect that in this case, the gain from the increase in α would be counteracted by the increase in noise on the wavelength determination since this weakly guided mode will be very lossy in water.

Since it was necessary to simplify the model and make some approximations to arrive at an expression which can be readily analyzed, we put the above analysis in perspective by doing full simulations. This is done by plotting LOD_t and LOD_n as previously defined for a wire waveguide which is not planarized. We do this as a function of width and by averaging out $n = 1.41 - 1.45$ RIU and $t = 2 - 9$ nm. Mind that the noise was taken as a constant at 220 fm, as before. Thus, only the influence of changing α is studied by these simulations. The result can be seen in Figure 3.19. We see a similar result in the sense that the LOD 's are not very dependent on the waveguide width and furthermore we see a large variance, indicated by the error bars, signifying the high dependence on the actual layer parameters.

In the following chapter we will look into a new sensor design and use these two leads as an analysis tool to verify whether the limit of detection improves or not: either by increasing α or reducing the noise.

References

- [1] Adam L Washburn, Matthew S Luchansky, Adrienne L Bowman, and Ryan C Bailey. *Label-Free Detection of Five Protein Biomarkers Using Multiplexed Arrays of Silicon Photonic Microring Resonators*. *Analytical Chemistry*, 82(1):69–72, 2010.
- [2] Graham H Cross, Andrew Reeves, Stuart Brand, Marcus J Swann, Louise L Peel, Neville J Freeman, and Jian R Lu. *The metrics of surface adsorbed small molecules on the Young's fringe dual-slab waveguide interferometer*. *Journal of Physics D: Applied Physics*, 37(1):74–80, January 2004.
- [3] Yuki Atsumi, Dan-Xia Xu, André Delâge, Jens H. Schmid, Martin Vachon, Pavel Cheben, Siegfried Janz, Nobuhiko Nishiyama, and Shigehisa Arai. *Simultaneous retrieval of fluidic refractive index and surface adsorbed molecular film thickness using silicon wire waveguide biosensors*. *Opt. Express*, 20(24):26969–26977, November 2012.
- [4] Tom Claes. *Labelvrije biosensoren op basis van geavanceerde fotonische ringresonatoren in silicium*. PhD thesis, UGent, 2012.
- [5] PhotonD. <http://www.photond.com/products/fimmwave.htm>.
- [6] K. Okamoto. *Fundamentals of optical waveguides*. Elsevier, 2006.
- [7] P. Schiebener, J. Straub, J. M. H. Levelt Sengers, and J. S. Gallagher. *Refractive index of water and steam as function of wavelength, temperature and density*. *Journal of Physical and Chemical Reference Data*, 19(3):677–717, 1990.
- [8] Katrien De Vos, Irene Bartolozzi, Etienne Schacht, Peter Bienstman, and Roel Baets. *Silicon-on-Insulator microring resonator for sensitive and label-free biosensing*. *Optics express*, 15(12):7610–5, June 2007.
- [9] Abraham J Qavi, Adam L Washburn, Ji-Yeon Byeon, and Ryan C Bailey. *Label-free technologies for quantitative multiparameter biological analysis*. *Analytical and bioanalytical chemistry*, 394(1):121–35, 2009.
- [10] Muzammil Iqbal, Martin A Gleeson, Bradley Spaugh, Frank Tybor, William G Gunn, Michael Hochberg, Tom Baehr-jones, Ryan C Bailey, and L Cary Gunn. *Label-Free Biosensor Arrays Based on Silicon Scanning Instrumentation*. *IEEE Journal of Selected Topics in Quantum Electronics*, 16(3):654–661, 2010.

- [11] Kristin E D Coan, Marcus J Swann, and Johannes Ottl. *Measurement and differentiation of ligand-induced calmodulin conformations by dual polarization interferometry*. *Analytical chemistry*, 84(3):1586–91, February 2012.
- [12] Jagoba J. Iturri Ramos, Stefan Stahl, Ralf P. Richter, and Sergio E. Moya. *Water Content and Buildup of Poly(diallyldimethylammonium chloride)/Poly(sodium 4-styrenesulfonate) and Poly(allylamine hydrochloride)/Poly(sodium 4-styrenesulfonate) Polyelectrolyte Multilayers Studied by an in Situ Combination of a Quartz Crystal Microb*. *Macromolecules*, 43(21):9063–9070, November 2010.
- [13] Fredrik Tiberg and Mikael Landgren. *Characterization of Thin Nonionic Surfactant Films at the Silica / Water Interface by Means of Ellipsometry*. *Langmuir*, 9:927–932, 1993.
- [14] Peter Nestler, Stephan Block, and Christiane A Helm. *Temperature-Induced Transition from Odd-Even to Even-Odd Effect in Polyelectrolyte Multilayers Due to Interpolyelectrolyte Interactions*. *J Phys Chem A*, 116:1234–1243, 2012.
- [15] J Ruths, F Essler, G Decher, and H Riegler. *Polyelectrolytes I : Polyanion / Polycation Multilayers at the Air / Monolayer / Water Interface as Elements for Quantitative Polymer Adsorption Studies and Preparation of Hetero-superlattices on Solid Surfaces*. *Langmuir*, 37(4):8871–8878, 2000.
- [16] John E Wong, Florian Rehfeldt, Peter Ha, Motomu Tanaka, and Regine Klitzing. *Swelling Behavior of Polyelectrolyte Multilayers in Saturated Water Vapor*. *Macromolecules*, 32:7285–7289, 2004.

4

Dual Polarization Vernier Cascade

4.1 Introduction

In the previous chapters the necessary components to build a dual polarization microring sensor have been discussed, as well as the top level system which describes how to measure thickness and refractive index simultaneously. The core element in this system is a single SOI microring capable of supporting two polarizations. A resolution of 0.1 nm on thickness and 1 mRIU on refractive index have been obtained. At the end of the previous chapter two main threads are suggested to improve the system **limit of detection** based on the essential system visualisation of Figure 3.13: reducing the surface of the detection limit rectangle by a noise reduction or by pulling the TE and TM curves in the (t, n) solution plane apart. In this chapter we swap the single microring by a combination of three microring resonators in a dual polarization Vernier cascade configuration and evaluate how it can improve the limit of detection based on these two threads. The Vernier cascade system has three main assets which are promising to achieve this goal. First, the microrings are organized in such a way that the sensitivities of both the TE and the TM mode to a change in the biolayer are enhanced due to the Vernier effect. Second, the system as a whole is made more robust and less susceptible to noise due to the introduction of a self-referencing system. Third, we have adopted a parallel read-out system based on a broadband LED and an integrated arrayed waveguide grating (AWG), suggested by Claes et al. [1], to replace the standard yet expensive serial read-out system based on a tunable laser. The last asset does not target an

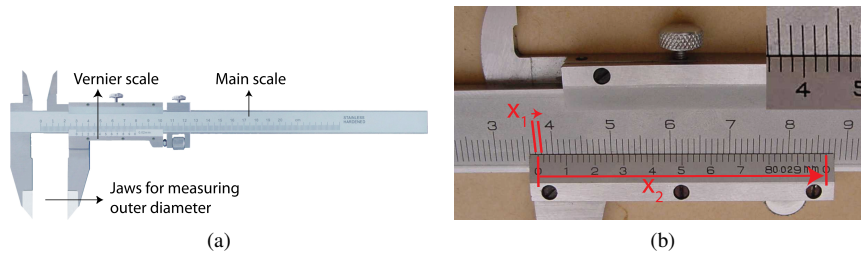


Figure 4.1: (a) Illustration of a modern Vernier caliper [?]. (b) Close-up of both measuring scales (not related to (a)), with a second close-up at the top right corner indicating the region where the two scales align [?]. The single scale reads 3.7 cm, while the addition of the second scale improves the measurement resolution such that a size of 3.746 cm is measured

improved LOD per se, but allows us to create a system which is orders of magnitude cheaper and which is capable of measuring at a higher temporal rate such that fast conformational changes can be quantified. However, we will see that this higher temporal rate can be used to improve the limit of detection as well.

Therefore, a theoretical framework is given in order to quantify these advantages numerically and in a comparative manner. A practical design is proposed, fabricated and characterized. A theoretical measurement framework is built in order to extract the thickness and density of a thin layer out of the compound spectra of the dual polarization Vernier cascade. Finally the limit of detection improvement is determined via a theoretical method.

4.2 Vernier principle

The Vernier principle is by no means an optical phenomenon as might be expected from its use in this context. It dates back to 1631 when French mathematician Pierre Vernier invented the Vernier caliper, which uses a secondary scale that increases the measuring resolution. An illustration of a modern incarnation of this caliper is shown on Figure 4.1(a). On Figure 4.1(b), a close-up of the scales (not related to 4.1(a)) is shown. Without the Vernier scale the position of the jaws indicating the size is only represented by the "0" on the Vernier scale. In this case, the apparatus would measure a size in between 3.7 and 3.8 cm. By adding a secondary scale which has a spacing that relates to the first spacing by a constant fraction (in this case the ratio of both spacings equals $49/50$), a more accurate result can be read by determining the point where both scales align. The inset shows this is where the secondary Vernier scale reads 46, such that the measured length equals 3.746. The Vernier caliper leverages the use of a reference since it is much easier

to determine a relative distance on sight as opposed to an absolute distance. The Vernier caliper also shows us how a small increase of the length of the object of one period on the main scale (indicated by x_1 on Figure 4.1), or 1 mm, corresponds to finding the aligned marks a distance x_2 further on the Vernier scale, or 5 cm further. In essence the signal x_1 has been amplified to the signal x_2 . While the main caliper has an accuracy of 0.1 cm, the addition of a the Vernier scale boosts the accuracy to 0.002 cm. Quite impressive for a slider.

4.3 Single polarization microring Vernier cascade

Moving from Pierre Vernier to state-of-the-art integrated photonics goes via recognizing the caliper scale in the repeating pattern of a comb of peaks in the transmission spectrum at the drop port of a microring resonator. The distance between two peaks in such a spectrum is the FSR. When two spectra with a slightly different FSR are multiplied with one another, a maximum arises in the compound spectrum only when two peaks are perfectly aligned along the wavelength axis. One immediately realizes that the period of this compound spectrum must be much larger than the period of the individual spectra, much like how the period of the combination of lines originating from the main scale and the Vernier scale in Figure 4.1(b) is much larger than the period of the main scale (or the Vernier scale) itself. This amplification of the period also manifests itself as the signal amplification we saw on Figure 4.1(b). It can be intuitively understood that the smaller the difference between the two scales, or the two FSR's, the larger the period of the compound spectrum will be, and thus the larger the signal amplification.

The physical interpretation of this multiplication of both spectra is achieved by connecting the drop port of one ring resonator to the input port of another ring resonator as illustrated in Figure 4.2: when light with a certain wavelength is transmitted by both ring resonators with a minimal drop in power it must have been at a resonance peak of both sensors. Since the FSR is directly determined by the optical path, a Vernier cascade is easily achieved by connecting a ring with a slightly smaller radius to a ring with a slightly bigger radius. This configuration of a single Vernier amplification has been covered in detail in [2]. In order for this Vernier cascade to be a biosensor, only one ring is functionalized with receptor molecules. This ring is the sensing ring, while the ring without probes is the reference ring. These microring resonators are in close proximity in the fluidic path thus we assume they are subjective to the same collection of fluidic parameters (a.o. geometrical flow conditions, flow rate, temperature, buffer variations, etc). In this configuration an amplified response is generated for a differential shift between both rings. Ideally this only occurs during a binding event. This is illustrated in Figure 4.3, where the top two figures show the output spectra of the individual

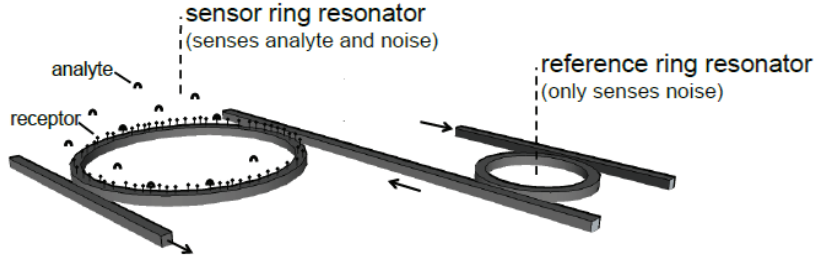


Figure 4.2: Traditional Vernier configuration for a single polarization [3]

rings before and after a binding event and the bottom two figures show the corresponding output of the Vernier cascade. We see that the output of the Vernier cascade is maximal when the overlap of the spectra of the two ring resonators is maximal as well. A small shift of the sensing ring $\Delta\lambda_1$ is then transduced to a larger shift $\Delta\lambda_2$ of the Vernier cascade. Just as with the Vernier caliper, where a small shift in length on the main scale x_1 is transduced to a larger shift in length x_2 on the Vernier scale (Figure 4.1).

This signal amplification is the first advantage of the Vernier cascade and in order to exploit this fully, we formulate two design guidelines for the single polarization case, which we will have to adhere to for both polarizations in the case of a dual polarization Vernier cascade. The first comes from the fact that Claes et al. [2] have shown that the limit of detection can be greatly improved by moving to a regime where the Vernier output spectrum does not consist of single isolated peaks (as in Figure 4.3) but out of a comb of peaks, whose peak amplitude varies smoothly. The Vernier spectral position is then determined by fitting an envelope to the maxima of the constituent peaks, which is in good approximation given by the square of a Lorentzian function [2]. A Vernier cascade spectrum consisting of a comb of peaks together with its envelope function is displayed in Figure 4.4. In order to obtain this comb, we require as a first design guideline that the difference in free spectral range (FSR) between the two rings is small compared to the full width half maximum (FWHM) of the resonance peaks of the individual rings (equation 4.1). As a second design guideline we strive to maximize the shift amplification of the Vernier cascade (V). This scales with the envelope period of the Vernier cascade ($P_{envelope}$), which in turn is limited by the bandwidth of the grating couplers which couple the light in and out of the SOI chip. Equations

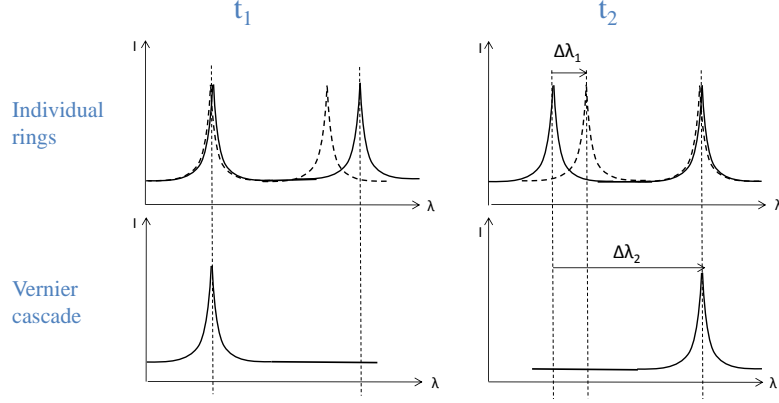


Figure 4.3: Vernier principle: top row shows the spectra of the individual sensing and reference rings in solid and dashed lines before and after a binding event, while the bottom row shows the corresponding Vernier cascade spectrum. At a time t_2 a differential shift $\Delta\lambda_1$ of the individual rings is amplified to a shift $\Delta\lambda_2$ of the Vernier cascade.

4.2-4.4 are the necessary equations to maximize V [2]. Here, λ is the resonance wavelength of the fundamental mode of the microring resonator, L is the length of the resonator and n_g is the group index of the resonator.

$$\Delta FSR < FWHM \quad (4.1)$$

$$V = \frac{P_{envelope}}{FSR_{sensor}} \quad (4.2)$$

$$P_{envelope} = \frac{FSR_{sensor} \cdot FSR_{ref}}{|FSR_{sensor} - FSR_{ref}|} \quad (4.3)$$

$$FSR = \frac{\lambda^2}{n_g \cdot L} \quad (4.4)$$

Notice how these equations formulate the concepts which arose from the Vernier caliper itself: the signal amplification V is equal to the amplification of the period from the spectrum of the single microring element FSR_{sensor} to the period of the compound spectrum $P_{envelope}$. Second, the period of the compound spectrum scales inversely with the absolute difference between the period of the two scales, or the FSR of the two individual spectra.

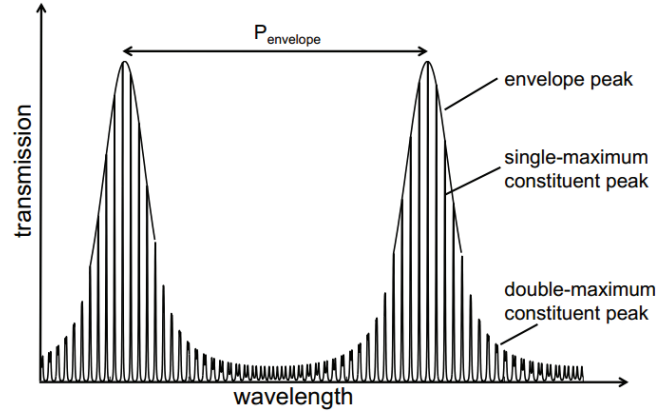


Figure 4.4: Vernier cascade adhering to inequality 4.1 to obtain a comb of peaks with a smoothly varying peak amplitude. The peak amplitudes can be fit to a squared Lorentzian in order to obtain the peak position and hence the shift of the Vernier cascade [3].

4.4 Exploiting the Vernier cascade in a dual polarization setting

We have seen in section 3.6.3 that there are two main strategies in order to improve the limit of detection of a system based on two unknowns. Both strategies can be interpreted visually from Figure 3.13. Either the system is changed such that the TE- and TM-curves defining the solution in the (t, n) -plane are rotated and become more orthogonal, or the perturbations on these curves, induced by measurement noise, are reduced.

4.4.1 Thread 1: Leveraging a differential amplification?

Changing the shape of the TE- and TM-curves is equivalent to changing the surfaces $\Delta\lambda_{TE}(t, n)$ and $\Delta\lambda_{TM}(t, n)$, which are defined in chapter 3. These surfaces need to be changed in a relative manner: the change of the TE-surface has to be different than the change of the TM-surface in order for the curves in the (t, n) -plane to enlarge their angle. We can expect this might be possible by using a different Vernier amplification for the TE as for the TM mode, which can be adjusted independently through design. On the other hand, the mathematical description of the surfaces is intrinsically governed by the light-matter interaction at the surface of the waveguide. Using a Vernier cascade is an alteration of the system at a higher signal level: the signal is merely amplified, but the interaction at the waveguide

level is unaltered.

Via the implicit function theorem a mathematical expression was given for the slope of the curve for a single polarization by means of equation 3.28. In the case of a Vernier cascade the function $F^{TE}(t, n)$ becomes:

$$F_{Vernier}^{TE}(t, n) = f_{Vernier}^{TE}(t, n) - \Delta\lambda_{exp, Vernier}^{TE} = 0 \quad (4.5)$$

$$F_{Vernier}^{TE}(t, n) = V^{TE} \cdot f^{TE}(t, n) - \Delta\lambda_{exp, Vernier}^{TE} = 0 \quad (4.6)$$

With $f^{TE}(t, n)$ equaling $\Delta\lambda_{TE}(t, n)$, but differing from $\Delta\lambda_{exp, Vernier}^{TE}$, which is the experimentally obtained shift. The amplification for the TE mode is V^{TE} , which is tunable by design. The slope around the locus of the solution (t, n) is then defined by

$$\left. \frac{dn}{dt} \right|_{Vernier} = \frac{\frac{\partial F_{Vernier}^{TE}}{\partial t}}{\frac{\partial F_{Vernier}^{TE}}{\partial n}} \quad (4.7)$$

Since the amplification factor V_{TE} is not dependent on t nor n , it gets canceled out in this ratio such that the slope of a Vernier cascade equals the slope of the single sensing ring of the Vernier cascade:

$$\left. \frac{dn}{dt} \right|_{Vernier} = \frac{\frac{\partial f^{TE}}{\partial t}}{\frac{\partial f^{TE}}{\partial n}} = \left. \frac{dn}{dt} \right|_{single\ ring} \quad (4.8)$$

And mutatis mutandis for TM. This shows that a Vernier amplification can't change the angle between the two curves in the (t, n) -plane.

4.4.2 Thread 2: Single ring equivalent noise reduction

We will check in the following sections whether or not the detection limit can be improved by a reduction of the noise which causes a displacement of the curves for TE and TM governed by the implicit functions defined in equation 3.3 and 3.4. To achieve this we will make abstraction of the specific sensor system design of the Vernier cascade and use the concept of an **equivalent ring resonator**. The Vernier cascade will be reduced to a single ring resonator and its improvements will be encoded in physical quantities on the level of a single ring resonator, such as noise, wavelength shift or limit of detection. This is necessary because not only the sensor system changes, but so does the measurement system, as will become clear in future sections. Therefore we can keep all the changes centralized and a straightforward comparison between two very different systems is possible. These equivalent quantities will be indicated by the superscript *. From a technical point

of view, we want to keep the solving protocol to determine t and n of an unknown layer, devised in section 3.2, in place. The Vernier spectra hence need to be calculated back to the equivalent shifts of the single ring resonators. This means that to calculate the limit of detection, we simply replace $\sigma_{\Delta\lambda}$ in Figure 3.13 by the newly determined $\sigma_{\Delta\lambda,V}^*$ and proceed as usual.

Moreover, this paradigm will immediately show another advantage of the Vernier cascade: the suppression of common noise due to self-referencing. To illustrate, we split up the measured wavelength shift of a single ring and of a Vernier cascade in its signal and noise contributions. The noise contributions are in turn split up in optical contributions (alignment, detector noise, noise due to fitting of the spectrum) and buffer contributions (temperature and buffer noise). The subscript V signifies the shift of the envelope of a Vernier cascade, while *ring* stands for the shift of a single ring resonator.

$$\Delta\lambda_{ring} = \Delta\lambda_{ring}^{signal} + \Delta\lambda_{ring}^{noise,opt} + \Delta\lambda_{ring}^{noise,buf} \quad (4.9)$$

$$\Delta\lambda_V = \Delta\lambda_V^{signal} + \Delta\lambda_V^{noise,opt} + \Delta\lambda_{ring}^{noise,buf} \quad (4.10)$$

In equation 4.10, we see that the noise contribution due to buffer noise to the envelope shift of a Vernier cascade equals the one to a resonance peak of a single ring resonator. This complies with the fact that for e.g. a temperature fluctuation, both sensing and reference ring are expected to have an equal shift, and hence the Vernier cascade does not amplify this signal but simply shifts with the same amount. The noise contribution to the Vernier shift due to optical noise however, is much larger than the one to a single ring due to the fact that we track an envelope 10-40 nm wide in case of a Vernier cascade, while a single ring has a sharp peak which is only 200 pm wide. For the signal contribution in equation 4.10 we know that $\Delta\lambda_V^{signal} = V \cdot \Delta\lambda_{ring}^{signal}$. We obtain

$$\Delta\lambda_{ring}^* = \frac{\Delta\lambda_V}{V}. \quad (4.11)$$

$$\Delta\lambda_{ring}^* = \Delta\lambda_{ring}^{signal} + \frac{\Delta\lambda_V^{noise,opt}}{V} + \frac{\Delta\lambda_{ring}^{noise,buf}}{V} \quad (4.12)$$

Comparing Eq. 4.9 with Eq. 4.12, it is clear that the buffer noise is suppressed by a factor V and the total noise contribution depends on the size of the optical noise of the Vernier sensor, which will be addressed further.

To compute the limit of detection we need to determine $\sigma_{\Delta\lambda,V}^*$. Therefore we assume Gaussian noise on the level of the ring resonator and by using equation 4.9, we find

$$\sigma_{\Delta\lambda,ring}^2 = \sigma_{\Delta\lambda,ring,opt}^2 + \sigma_{\Delta\lambda,ring,buf}^2 \quad (4.13)$$

and with equation 4.12, the equivalent ring noise of a Vernier cascade equals

$$\sigma_{\Delta\lambda,V}^{*2} = \frac{\sigma_{\Delta\lambda,V,opt}^2}{V^2} + \frac{\sigma_{\Delta\lambda,ring,buf}^2}{V^2} \quad (4.14)$$

From equation 4.13, we know that $\sigma_{\Delta\lambda,ring,buf}$ is limited by $\sigma_{\Delta\lambda,ring}$. This variance on the total noise on a binding curve was determined experimentally in section 3.6.1 to be 220 fm. This means that $\sigma_{\Delta\lambda,ring,buf}$ is smaller than 220 fm and hence negligible towards $\sigma_{\Delta\lambda,V,opt}$ in equation 4.14, which is in the order of 20 pm. Hence, we can approximate the single ring equivalent noise of a Vernier cascade as

$$\sigma_{\Delta\lambda,V}^* \approx \frac{\sigma_{\Delta\lambda,V,opt}}{V} \quad (4.15)$$

In what follows $\sigma_{\Delta\lambda,V}^*$ will be determined numerically such that the limit of detection for the dual polarization Vernier cascade can be determined. In case of a single polarization Vernier cascade system, we can replace the single ring total noise in equation 3.23 by the Vernier equivalent one to obtain the single ring equivalent limit of detection of a Vernier cascade:

$$LOD_V^* \approx \frac{\sigma_{\Delta\lambda,V,opt}/V}{S_{ring}} \quad (4.16)$$

Mind that the subscript *ring* has been added to the transduction sensitivity S from equation 3.23 to emphasize the fact that the limit of detection is a single ring equivalent value.

4.5 Dual polarization vernier cascade

4.5.1 Photonic integrated design

When moving from a single polarization to a dual polarization Vernier sensor, we must adhere to the two design guidelines stated in section 4.3 for each polarization: complying with inequality 4.1 and maximizing V . Furthermore, we followed three additional guidelines. First, we have chosen for a design in which as many structures and waveguides are shared as possible, as opposed to duplicating the single mode design for both modes. Indeed, each time a structure is duplicated, this might introduce extra noise due to fabrication variations on both nominally identical structures. Due to the high index contrast of the SOI platform, small variations in design can have a large impact on system characteristics. We did choose for a separate TE and TM sensing ring so as to relax the complexity of coupling and of the signal processing. This allows the Vernier amplification to be tuned for each mode individually as well. Although we have shown in section 4.4.1 that this does not provide the necessary mechanisms to boost the differential behavior leading to an improved limit of detection, it is required in order to maximize the amplification

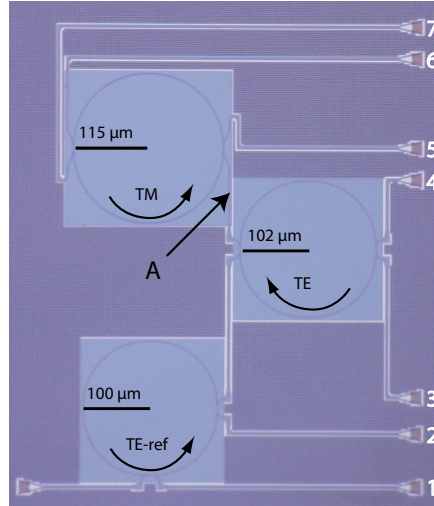


Figure 4.5: SEM picture of a dual polarization Vernier design consisting of three SOI microrings. The point annotated by "A" indicates the pass port of the TE ring.

for both modes to an equal value since this is governed by the optical path and not the length of the resonator alone. Second, and analogous to the dual polarization microring design, we strive to couple the light in and out of the chip and do all the routing using strictly the TE mode. Finally, we tried to avoid splitters. Our experience is that splitters might introduce unwanted reflections which can create extra complexity in the output spectra, making the evaluation of a proof-of-concept design ambiguous. This does complicate the design on the level of signal analysis, since it is more difficult to isolate certain signals. In a second stage the use of optimized splitters is advised however.

As a proof-of-concept we designed a dual polarization Vernier cascade which adheres to these five guidelines while maintaining a ring radius of $\sim 100 \mu\text{m}$ to limit the footprint of the sensor. This stems from purely practical considerations as more sensors can be printed on a single photonic chip for testing purposes this way. It does limit the amplification via equation 4.2. Longer sensors with reduced footprint can be designed however using folded cavities [4]. The design was fabricated and a section of a photonic chip containing the sensor is pictured with SEM and shown on Figure 4.5. The reference (TE) sensor resides at the bottom and the two sensing rings at the top, one for TE and one for TM polarization. Since all routing and in- and out-coupling is done in TE mode, we use an asymmetrical coupling section in the TM sensing ring, as before. The width of the waveguide cross section in the TM ring waveguide is designed to be 600 nm, while the width of the waveguide cross section in the access waveguide is 320 nm. The reference ring,

the TE sensor ring and the routing waveguides are all designed to have a width of 450 nm. Finally, the radii of the three rings are designed to keep the footprint reasonable and maximize V_{TE} , which is governed by the reference ring and the TE sensing ring, and V_{TM} , governed by the reference ring and the TM sensing ring. This is done in a way prescribed by equations 4.2-4.4, while obeying to inequality 4.1 for both polarizations. The group index of the waveguide cross section of the reference ring and the TE sensing ring amounts to 4.36. With a coupling length of the ring of $1 \mu\text{m}$ and a radius of $100 \mu\text{m}$ and $102 \mu\text{m}$ for the reference ring and TE ring respectively, we obtain a ΔFSR of 15 pm. The FWHM of these rings is about 150-200 pm, such that inequality 4.1 is fulfilled. Second, the $P_{envelope}$ amounts to 44 nm. With a bandwidth of the grating couplers of 40 nm, the complete envelope can be read out without significant loss of power of the outer spectral bands relative to the inner ones. Finally, we design the TM sensing ring to have the same FSR as the TE sensing ring. Similar to the above, this implies a ring radius of $115 \mu\text{m}$.

4.5.2 Experimental and theoretical spectra

In order to facilitate the discussion in this section, the measured and theoretical transmission spectra at the various ports of the Vernier cascade will be henceforth indicated with T_x , with x the port number. Apart from ports 1-7, the spectrum at the pass port of the TE ring, indicated in Figure 4.5 with the letter "A" will also be referenced in this manner. This spectrum is however not measurable with this specific design. The measured spectra to retrieve the thickness and refractive index of the bilayer are T_3 and T_7 and are related to the ring spectra as follows:

$$T_3 = T_{ref,drop} \cdot T_{TE,drop} \quad (4.17)$$

$$T_7 = T_{ref,drop} \cdot T_{TE,pass} \cdot T_{TM,drop} \quad (4.18)$$

To characterize the Vernier cascade sensor, light is coupled through the single input port on the left with an Agilent tunable laser through a fiber. Output ports 1, 3 and 7 are read out one by one by sweeping the wavelength of the laser and collecting the light through an optical fiber which is connected to an HP power meter. During the characterization the SOI chip is covered with deionized water to mimic a bio-experiment in which proteins are dissolved in an aqueous buffer and flown over the chip surface. The measured spectra T_1 , T_3 and T_7 are shown on Figure 4.6 (a,c,e). In order to verify the experimentally obtained spectra, the sensor is simulated through a combination of the commercially available packages Fimmwave [5] and Caphe [6]. Fimmwave is used to solve the 2D cross section, providing us with n_{eff} and n_g of the TE and TM mode. This data is fed into Caphe which is a novel photonic circuit modeler, designed by Luceda. It allows

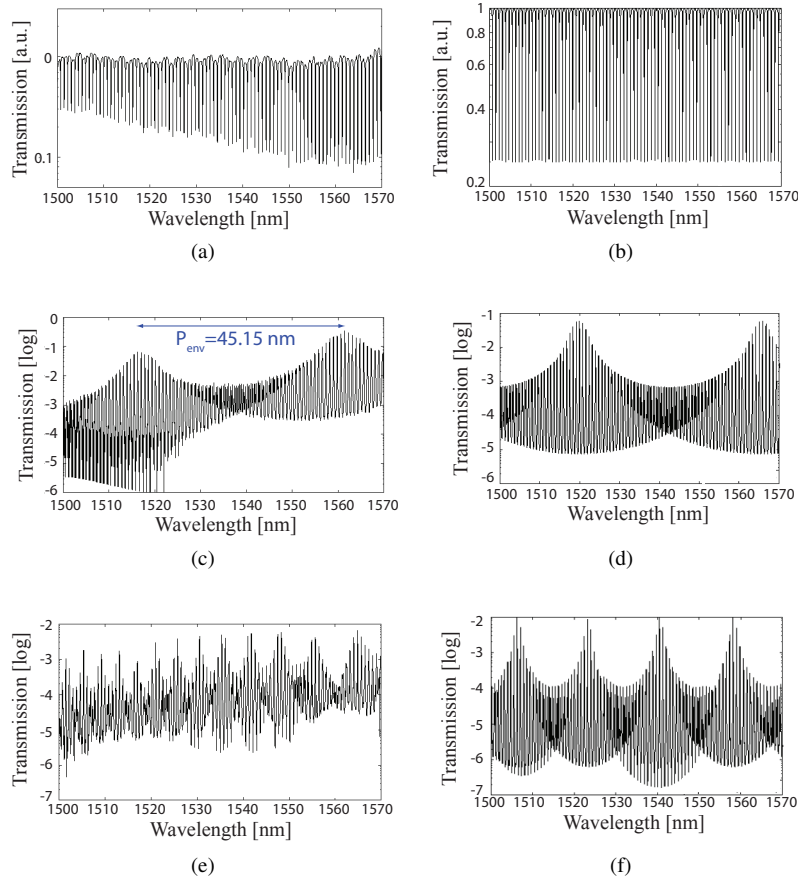


Figure 4.6: Simulated and measured spectra of the output ports of the Vernier cascade, with the port numbers shown on figure 4.5. (a) Measured spectrum of port 1, (b) simulated spectrum of port 1. (c) Measured spectrum of port 3, (d) simulated spectrum of port 3. (e) Measured spectrum of port 7, (f) simulated spectrum of port 7. The measured spectra are compensated for the transmission spectrum of the grating coupler.

to connect the rings and generate the output spectra at the three output ports. The simulated output spectra are shown in Figure 4.6 (b,d,f) for respectively port 1, 3 and 7.

We can see that the measured T_3 agrees to the simulated T_3 very well. The measured period amounts to 45.15 nm, close to the designed period of 44 nm. Although the period of the simulated T_7 differs from the one in the measured spectrum, the shape bears close resemblance. This is due to the fact that the fabrication tolerances will only have a small influence on T_3 compared to T_7 , since the

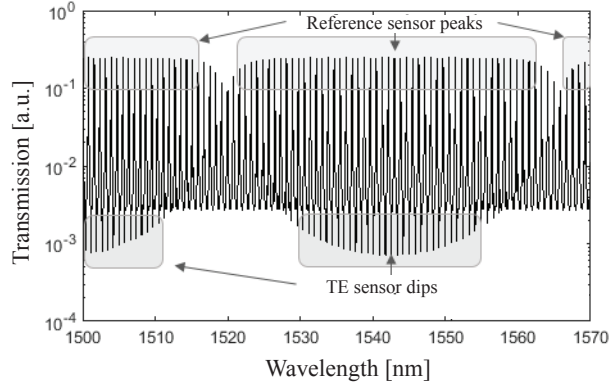


Figure 4.7: Simulated Vernier spectrum at point A, indicated in Figure 4.5, obtained by transmission through the drop port of the reference ring and consequently transmission through the pass port of the TE ring.

cross sections of the reference ring and the TE sensing ring are equal. A bias will hence have a minor effect due to the relative nature of the Vernier cascade. On the contrary, T_7 is a combination of spectra originating from rings with 2 different cross sections, as well as 2 orthogonal polarizations. While the TE mode is more sensitive to changes in the width, the TM mode is more sensitive to changes to the height. Due to the relative flatness of the waveguide, the TM mode is more sensitive to fabrication tolerances and thus T_7 is expected to differ more from simulations than T_3 .

The spectrum which is measured at port 3 is the compound Vernier spectrum of the reference ring and the TE ring. The shift of the envelope $\Delta\lambda_{env,TE}$ can hence be extracted in a straightforward way by fitting the envelope to a squared Lorentzian. The extraction of $\Delta\lambda_{env,TM}$ is more complex because T_7 is influenced by all three rings (equation 4.18): reference ring, TE ring and TM ring. To examine how the TE ring influences T_7 , we will simulate the signal which is being fed into the TM ring: the spectrum at the pass port of the TE ring, T_A . This can be seen on Figure 4.7, for which the same parameters were used as for the simulated spectra on Figure 4.6. We observe that the interaction between the reference ring and the TE ring is much smaller at T_A (Figure 4.7) than at T_3 (Figure 4.6 (c)), while the only difference is that in T_3 the drop port of the TE ring is used as output, while in T_A the output is read at the pass port. In Figure 4.7 we see that the peaks of the reference ring are visible in wide spectral ranges at the top of the spectrum, while the dips are visible at the bottom of the spectrum. Furthermore, the minor influence of the TE ring is also visible in the compound spectrum at T_7 ,

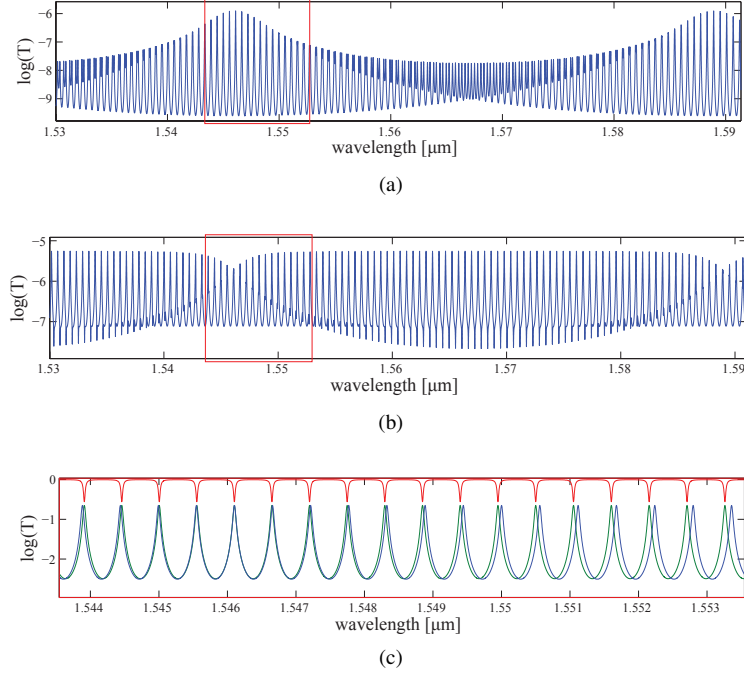


Figure 4.8: Simulated spectra of (a) $T_3 = T_{ref,drop} \cdot T_{TE,drop}$ and (b) $T_A = T_{ref,drop} \cdot T_{TE,pass}$. The individual ring spectra that make up these Vernier cascades for the area in (a) and (b) which is marked by a red rectangle, are pictured in (c): $T_{ref,drop}$ in blue, $T_{TE,drop}$ in green and $T_{TE,pass}$ in red.

shown in Figure 4.6 (f): the periodicity here corresponds to the periodicity of the reference ring and the TM ring. This shows that the TM peaks and the peaks of the reference ring can interact without much interference from the dips of the TE ring, but a local perturbation where the TE ring and the reference ring are in perfect phase is inevitable. To look into the reason why we observe a higher level of interaction of the TE ring and the reference ring at T_3 , as opposed to at T_7 , Figure 4.8 shows simulations of both the spectra T_3 and T_A , together with the individual ring spectra that make up these Vernier cascades. Around 1.546 μm , all the spectra are in phase and we see a dip in T_A and a peak in T_3 . It is clear that the overlap of the peaks which make up T_3 is larger than the overlap of the dip of $T_{TE,pass}$ and the peak of $T_{ref,drop}$ because the rings are not critically coupled.

We conclude that it is perfectly feasible with this design to extract the necessary envelope shifts, but a design with a signal splitter which connects the output of the reference ring to the TE ring at one side and the TM ring at the other side will have a better limit of detection. In this case $\Delta\lambda_{env,TE}$ and $\Delta\lambda_{env,TM}$ can be

measured independently, without one signal perturbing the other. To determine the theoretical limit of detection in the future sections, we will assume this best-case scenario.

4.5.3 Including an AWG to improve the limit of detection

From sequential to parallel read-out

As mentioned in the introduction, the rationale of exploring the presented sensor is improving the limit of detection due to an increase in sensitivity and a decrease of the contribution of noise on the measured signal. The amplification of the resonance shift due to the Vernier effect has a third advantage however: it allows to discard the expensive tunable laser in the measurement system and swap it for a cheap broadband LED.

In order to track the shift of a resonance feature of any cavity sensor, the spectral resolution of the measurement system needs to be fine enough to resolve the resonance feature. For a single microring resonator, this means the system needs to cope with the stringent spectral requirements of a 100-200 pm wide resonance peak. The standard way of doing this is by leveraging the fine spectral sampling of a tunable laser source (~ 5 pm), combined with a spectrally blind power meter [7, 8]. Equation 4.2 shows that the resonance feature of a Vernier cascade that needs to be tracked (P_{env}) scales with the amplification factor V , implying that the spectral resolution of the measurement system can be increased by V as well. In practice, the envelope is 10-40 nm wide, such that the width of the feature we track increases over a hundred-fold, compared to a single ring. By increasing the spectral resolution of the measurement system by the same amount to 0.5 nm, we should thus not experience any deterioration of the limit of detection of the sensor due to undersampling. This spectral feature is in the ballpark of an integrated AWG, which can have a channel width down to 0.5 nm [9]. This leads to the conclusion that we can flip the measurement system around, with regards to where the spectral filter is located: a spectrally blind broadband LED as input, and an integrated spectral filter (AWG) with off-chip detectors on a camera as output. Every wavelength channel in an AWG has its own output waveguide running to an output coupler which is imaged on a dedicated pixel on the pixel array of the camera. As such, this system captures the whole spectrum in one camera frame. On Figure 4.9 we see how a Vernier spectrum is sampled by an AWG and subsequently an envelope is fit through these sampled points to determine the central position. For the fitting of this envelope, a squared Lorentzian is used [1].

One major advantage of this scheme is that the full spectrum can now be captured at the rate of the camera, while for the sequential system with a tunable laser

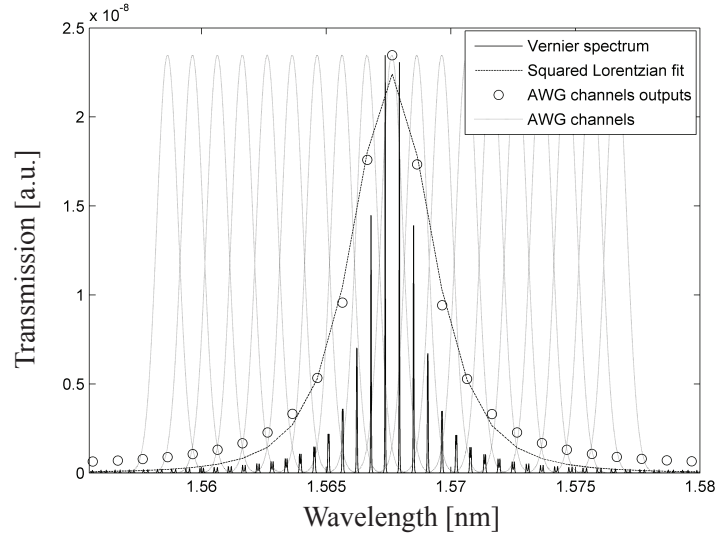


Figure 4.9: Vernier spectrum convolved with a Gaussian AWG channel of 0.5 nm wide. Through the sampled discrete points, a squared Lorentzian is fit to determine the peak position.

that is swept, a single camera frame is used for a single wavelength. For a span of 10 nm with a 5 pm resolution, the new system is therefore 2000 times faster. In absolute terms, a 1D line camera can have a framerate surpassing 20 kHz, paving the way for a very high temporal resolution system, which is beneficial for noise averaging. Furthermore, a broadband LED costs a fraction of a tunable laser, which is by far the dominant cost factor in the whole system.

Optimizing the AWG

To benchmark the influence of the parameters of an AWG, such as number of channels and channel spacing, we shall use the limit of detection as determined in equation 4.16. Since S_{ring} is not influenced by the addition of an AWG, only the determining fraction $\sigma_{\Delta\lambda, V, opt}/V$ is plotted in function of the length of the sensor ring for a single polarization Vernier cascade on Figure 4.10. Several AWG designs with varying number of channels and channel spacings are included. We have set the envelope period of the Vernier spectrum equal to the number of channels multiplied by the channel spacing. The noise on the binding curve which

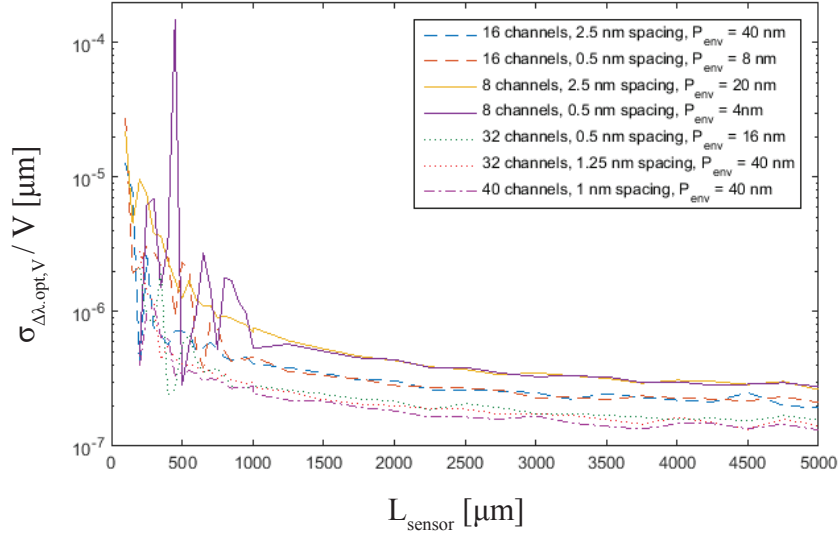


Figure 4.10: Classical limit of detection in function of the length of the sensor ring in a single polarization Vernier cascade for several AWG designs.

determines the LOD is computed via Monte Carlo simulations. For each value of L_{sensor} , the corresponding L_{ref} is determined via equation 4.3. Next, the theoretical Vernier spectrum is obtained via its two theoretical microring spectra [10]. This Vernier spectrum is then convolved with the AWG channel profile, as shown in Figure 4.9. Additionally, relative intensity noise with a 0.01 standard deviation and a fixed noise floor with a 0.01 standard deviation is added in an uncorrelated way to each of the discrete points of this spectrum to represent noise in the optical alignment and detector noise. These parameters correspond to measured noise values. Finally, this discrete noisy spectrum is fit to a squared Lorentzian [2] to determine the peak position. For each value of L_{sensor} , this is repeated 500 times with the normally distributed noise quantified above. The standard deviation on these 500 peak positions can be regarded as the optical noise $\sigma_{\Delta\lambda, opt, V}$. This noise is divided by the sensitivity enhancement V (eq. 4.2) to obtain a metric that scales with the LOD .

From Figure 4.10 we can conclude first that the LOD improves when the sensor gets longer. This is to be expected since the amplification scales with the length of the sensor, for a constant envelope period. The improvement in LOD saturates however, which is due to the broadening of the Vernier cascade for longer sensors. Furthermore, as the single sensor peaks get closer together they can start over-

lapping which causes the Vernier spectrum to diminish in contrast. Both spectral broadening as well as a loss in contrast have a negative impact on $\sigma_{\Delta\lambda,opt,V}$. Since the LOD does not decrease significantly for sensors longer than 4 mm and since the dynamical range also decreases when the sensor length increases, a microring with sensor length of 4 mm is proposed. With a maximal P_{env} of 40 nm, this corresponds to a maximal V of 288 (equation 4.2). Second, an increase in the number of channels clearly has a positive influence on the LOD. This causes a better sampling of the Vernier cascade and a reduction of $\sigma_{\Delta\lambda,opt,V}$. Third, for a given sensor length and number of channels, increasing the envelope period does not have an influence. The sensitivity increase accompanied by an increase in P_{env} is canceled out by an equal increase of $\sigma_{\Delta\lambda,opt,V}$ due to an increase in channel spacing.

4.6 Measurement framework

Ideally, we can use the protocol to extract the thickness and the refractive index of a bound biolayer outlined for a single ring dual polarization ring resonator, in this Vernier cascade context. In order to do so we must obtain the effective indices, or equivalently, the resonance wavelength shifts of the TE and TM ring resonator that make up the dual polarization Vernier cascade. However, we only have access to the compound Vernier cascade spectra at the different output ports, so a measurement framework that extracts the single ring shifts from these Vernier spectra is necessary. First we will construct this framework from a sequential flow based on three equations, which we will link to certain measurements later.

These equations are given below in their logical order, with the unknown quantity expressed in bold, for which the next equation provides an expression. Mind that these equations need to be solved for both TE and TM Vernier cascades. The derivation of the FWHM of the envelope is given in detail in [2].

$$\Delta\lambda_{ring}^* = \frac{\Delta\lambda_V}{V} \quad (4.19)$$

$$V = \frac{FSR_{ref}}{|\mathbf{FSR}_{sensor} - FSR_{ref}|} \quad (4.20)$$

$$FWHM^{env} = 2 \cdot \sqrt{\sqrt{2} - 1} \cdot \frac{FWHM_{ring} \cdot FSR_{min}}{|\mathbf{FSR}_{ref} - FSR_{sensor}|} \quad (4.21)$$

In these equations, FSR_{sensor} denotes the FSR of the individual TE or TM rings, while FSR_{ref} denotes the FSR of the reference ring. In case the envelope consists of the TE ring and the reference ring, $FWHM_{ring}$ equals the FWHM of the TE ring. In case the envelope consists of the TM ring and the reference ring and the difference between the widths of their constituent peaks is small, $FWHM_{ring}$

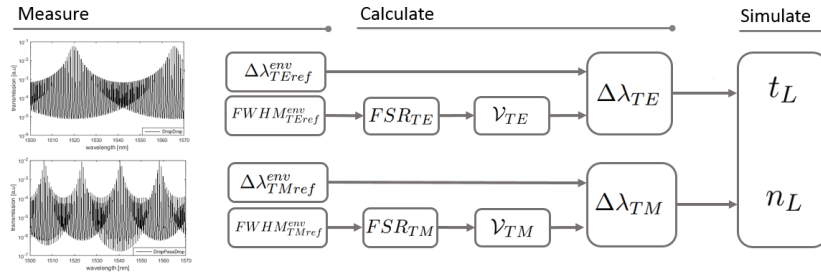


Figure 4.11: Measurement framework to determine the thickness and refractive index of a bound molecular layer to the surface of the microrings making up the dual polarization Vernier cascade.

equals in close approximation to the geometrical mean of the FWHM of the reference ring and the TM ring. This follows from the derivations made in [2]. Although for critically coupled rings, the reference ring, which is a TE ring, will have a higher Q in water than the TM ring, they can be made equal by e.g. overcoupling the reference ring to increase its FWHM. $FWHM_{ring}$ can be considered constant during the experiment, as well as FSR_{ref} for small noise factors in a certain bulk fluid.

The first equation is a straightforward relation between the measured shift of the Vernier envelope and the unknown equivalent ring shift. The shift of the Vernier envelope is obtained by continuously collecting the spectra at port 3 (TE) and port 7 (TM) as indicated on Figure 4.5, after the signal has passed through a dedicated AWG. Fitting the outputs of the AWG channels to a squared Lorentzian determines the peak of the envelope and hence the shift of the Vernier envelope $\Delta\lambda_V$. Next, the amplification factor is determined solely by FSR_{sensor} , for which it suffices to measure the full width half maximum of the Vernier cascade envelope $FWHM^{env}$ via equation 4.21 [2]. This quantity is determined simultaneously with the shift of the envelope since it is a parameter of the squared Lorentzian to which the measured spectrum has been fit. However, looking at Figure 4.9 we see that the envelope of the Vernier spectrum convolved with the AWG channel is broader than the envelope of the Vernier spectrum itself.

In order to check the magnitude of this broadening over a wide range of Vernier cascade designs, P_{env} was swept from 5 to 50 nm, with a fixed optimal sensor length of 4 mm and AWG channel width of 1 nm. The FWHM of the Vernier cascade filtered by the AWG is plot in function of the FWHM of the Vernier cascade in Figure 4.12 and a linear trend is observed. The slope of the linear fit is 1.8014. Using this constant, the FWHM of the Vernier cascade can be obtained

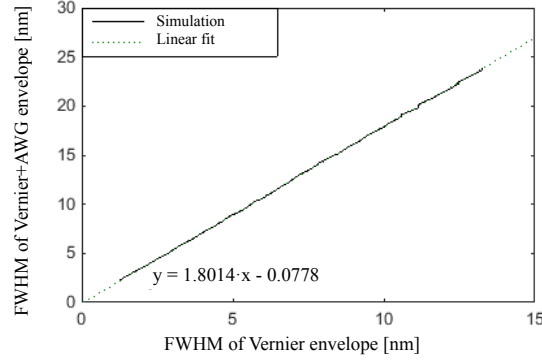


Figure 4.12: Relation between the FWHM of the envelope of a Vernier cascade and the FWHM of the envelope obtained by filtering this Vernier through an AWG with channel width of 1 nm. The sensor ring has a length of 4 mm. The envelope of the Vernier cascade is swept from 5 to 50 nm.

from the AWG channels. The complete measurement and calculation framework is presented schematically in Figure 4.11. The final step is solving the acquired ring equivalent shifts back to a thickness and density profile of the layer-under-test.

4.7 Sensor Performance

4.7.1 Detection limit of a Vernier cascade

In order to assess the limit of detection for both t and n for the dual polarization Vernier cascade, we will use the same protocol as in section 3.6.1, but we replace $\sigma_{\Delta\lambda,ring}$ by the ring equivalent noise factor of the Vernier cascade $\sigma_{\Delta\lambda,V}^*$ as determined in equation 4.15. This allows us to preserve the ring resonator equations $f(t, n)$ and $g(t, n)$. Equation 4.15 shows that this requires us to determine the optical noise of a Vernier cascade sensor $\sigma_{\Delta\lambda,V,opt}$ and divide it by the Vernier amplification factor V . This is done by performing Monte Carlo simulations similar to the one in section 4.5.3, but with a sensor length of 4 mm, as we found (in section 4.5.3) that this is the optimal sensor length. We have set the envelope period to 32 nm, while choosing an AWG spectrum which is 40 nm wide, with a channel spacing of 1 nm. This is to prevent the peak of the Vernier envelope to just coincide with the edge of the AWG width, rendering the fitting impossible. The envelope period and sensor length fix the sensitivity enhancement to 231. Different than the previous Monte Carlo simulation is that the design of the Vernier and AWG is fixed, but the position of the Vernier, relative to the AWG is shifted for every iteration, corresponding to a realistic sensing experiment. The noise param-

eters are equal to those in section 4.5.3. The standard deviation is now determined on the error of the peak position for 5000 iterations. For the optimum Vernier cascade and AWG design we find an optical noise $\sigma_{\Delta\lambda,V,opt}$ of 37.2 pm. Dividing this by V , we obtain that $\sigma_{\Delta\lambda,V}^*$ equals 161 fm. Since this is smaller than the $\sigma_{\Delta\lambda,ring}$ of 220 fm, we expect the limit of detection to improve. This ring equivalent noise can be used to compute LOD_t and LOD_n as shown in Figure 3.13. We repeat this procedure for a 2D space of (t,n) -couples in the domain $[2\text{ nm}; 10\text{ nm}] \times [1.43; 1.47]$, representing realistic layers of proteins. The average LOD_t amounts to 28.9 pm and the average LOD_n amounts to 0.84 mRIU. When the same procedure is done with the measured 220 fm for a single ring, we have found an average LOD_t of 39.6 pm and an average LOD_n of 1.1 mRIU. in section 3.6.1.

This shows that a small improvement in LOD is made over a single dual polarization ring. However, the system has become orders of magnitude cheaper, and the time resolution has increased by 2000 times. This increased time resolution can be beneficial to observe fast conformational changes, but it can also be used to improve the limit of detection even further by averaging. A signal with uncorrelated gaussian noise with variance σ can be downsampled by a factor M by replacing M samples by its average. This downsampled signal has a reduced variance of σ/\sqrt{M} . If we reduce the time resolution of the Vernier cascade to the time resolution of a single ring resonator via downsampling, we can now rewrite equation 4.16 as follows, with downsampling factor M equaling to the ratio of the temporal rates $R_V/R_{ring} = 2000$:

$$LOD_V^* \approx \frac{\sigma_{\Delta\lambda,V}^*}{\sqrt{R_V/R_{ring}}} \cdot \frac{1}{S_{ring}} \quad (4.22)$$

The first factor on the right-hand side equals 3.6 fm, such that with a similar routine as in Figure 3.13, the average LOD_t amounts to 0.6 pm and LOD_n amounts to $17.9\ \mu\text{m}$. These numbers are unrealistic however since for fast enough rates, the noise will no longer be Gaussian nor uncorrelated and hence the σ will no longer decrease by averaging. As such, these numbers are a strict theoretical limit. This last section does show that an improvement in the limit of detection is possible by using a system with a higher acquisition rate. The size of this increase is however subject to a detailed noise analysis and measurements, which is beyond the scope of this thesis.

4.8 Conclusion

We have designed a Vernier cascade dual polarization sensor that enhances the performance compared to a single ring dual polarization sensor. The functionality

remains the conformational analysis of proteins through simultaneous determination of thickness and refractive index of a thin molecular layer which binds to the sensor surface. However, by using a compound sensor consisting of three rings, three main advantages were found: an increased sensitivity due to the Vernier amplification, a reduction of common noise factors due to self-referencing and the possibility to employ a measurement system comprising of a cheap LED and an on-chip AWG as a spectral filter. This last advantage allows to measure conformational changes at a rate which is increased by a factor of 2000 and at a cost which is orders of magnitude smaller compared to the standard way of measuring ring resonators by sweeping an expensive tunable laser. We have fabricated a proof-of-concept of the sensor and were able to match the measured spectra at the several output ports to simulated spectra. We have used these theoretical spectra to propose a measurement and computational framework to obtain the thickness and density of the bound molecular layer based on the measured compound spectra. Furthermore, we have proposed an optimal design, both with respect to the micro-ring parameters of the Vernier cascade as to the parameters of the AWG. The limit of detection of the Vernier cascade + AWG has been determined theoretically in a way that allows direct comparison to the dual polarization single ring resonator. As such an improved limit of detection of 28.9 pm on thickness and of 0.84 mRIU on refractive index has been obtained. Finally, it has been shown that the limit of detection can be further improved compared to a single ring resonator by leveraging the increased temporal rate due to the parallel read-out of the spectrum.

References

- [1] Tom Claes, Wim Bogaerts, and Peter Bienstman. *Vernier-cascade label-free biosensor with integrated arrayed waveguide grating for wavelength interrogation with low-cost broadband source*. Optics letters, 36(17):3320–2, September 2011.
- [2] Tom Claes, Wim Bogaerts, and Peter Bienstman. *Experimental characterization of a silicon photonic biosensor consisting of two cascaded ring resonators based on the Vernier-effect and introduction of a curve fitting method for an improved detection limit Abstract* .: Optics Express, 18(22):22747–22761, 2010.
- [3] Tom Claes. *Labelvrije biosensoren op basis van geavanceerde fotonische ringresonatoren in silicium*. PhD thesis, UGent, 2012.
- [4] D X Xu, a Densmore, a Delâge, P Waldron, R McKinnon, S Janz, J Lapointe, G Lopinski, T Mischki, E Post, P Cheben, and J H Schmid. *Folded cavity SOI microring sensors for high sensitivity and real time measurement of biomolecular binding*. Optics express, 16(19):15137–48, September 2008.
- [5] PhotonD. <http://www.photond.com/products/fimmwave.htm>.
- [6] Lucedaphotonics. *Caphe*. <http://www.lucedaphotonics.com>.
- [7] Katrien De Vos, Irene Bartolozzi, Etienne Schacht, Peter Bienstman, and Roel Baets. *Silicon-on-Insulator microring resonator for sensitive and label-free biosensing*. Optics express, 15(12):7610–5, June 2007.
- [8] Muzammil Iqbal, Martin A Gleeson, Bradley Spaugh, Frank Tybor, William G Gunn, Michael Hochberg, Tom Baehr-jones, Ryan C Bailey, and L Cary Gunn. *Label-Free Biosensor Arrays Based on Silicon Scanning Instrumentation*. IEEE Journal of Selected Topics in Quantum Electronics, 16(3):654–661, 2010.
- [9] Shibnath Pathak, Dries Van Thourhout, and Wim Bogaerts. *Design trade-offs for silicon-on-insulator-based AWGs for (de) multiplexer applications*. Optics Letters, 38(16):2961–2964, 2013.
- [10] Wim Bogaerts, Peter De Heyn, Thomas Van Vaerenbergh, Katrien De Vos, Shankar Kumar, Tom Claes, Pieter Dumon, Peter Bienstman, Dries Van Thourhout, and Roel Baets. *Silicon Microring Resonators*. Laser Photonics Rev., 6:1–28, 2011.

5

Measuring the conformation of biological molecules

5.1 Introduction

In the introductory chapter we underlined the importance of the conformation of biomolecules with respect to the decisive role it plays in regulating the functional behavior of these key agents of life. The intricate traversing through cells, the availability for activation and the compatibility with other molecules are highly determined by the actual state of conformation. It comes as no surprise that knowledge of these conformational pathways, as well as the possibility to actively interfere with these conformations and manipulate them would be highly desired for proteomics, genomics and the pharmaceutical industry. This is even more true since certain degenerative diseases have a direct relation to the conformational state of its key protein.

In this chapter we will verify whether the dual polarization microring system presented in the previous chapters, can help in unveiling the conformations of biomolecules such as proteins and DNA. We will do this in a two-step approach. First we will attempt to detect the change of shape of a known system: bovine serum albumin (BSA) molecules as they reconfom under the influence of a change in pH value of the buffer fluid. This system has been documented before by means of dual polarization interferometry (DPI) and hence we know there should be a conformational change and we can verify whether our system can detect it.

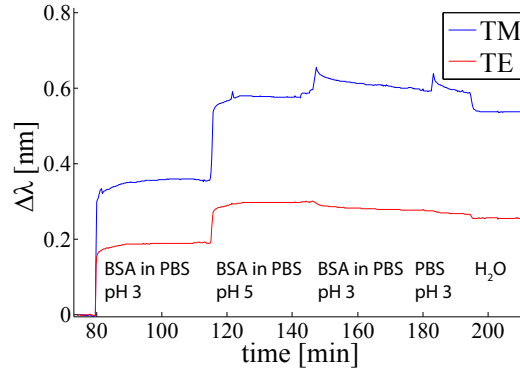
In a second stage we will use the dual polarization system to optimize the hybridization of DNA to the silicon surface. We will describe a DNA hybridization experiment in which a DNA probe is attached to the sensing surface, followed by streaming the complementary DNA strand over the chip surface. When the DNA strand hybridizes with the DNA probe, a sensor signal is generated. The functionalization of the silicon surface and the orientation of the DNA probes is determining for the subsequent hybridization. However, this orientation and the geometry of the layers in general are often not well understood, due to a lack in high-resolution tools. By using dual polarization microrings, we will attempt to provide more information on these thin layers consisting of DNA probes as to improve the performance of DNA detection sensors. This work is done in collaboration with the polymer chemistry and biomaterials research group at UGent. The contribution of Anabelle Van Eeghem to correctly functionalize the chip surface and optimize the DNA hybridization parameters was crucial to obtain successful hybridization. This work is in final stage before publication in an international journal.

5.2 Conformational analysis of BSA molecules

A BSA molecule can be characterised as a prolate ellipsoid with dimensions $14 \text{ nm} \times 4 \text{ nm}$ [1]. It is often used as a blocking agent in an immunoassay to prevent non-specific binding and adsorption to the surface [2]. The adsorption behavior of BSA on the silicon surface of the microring is thus crucial to avoid measuring false positives. It is a soft protein, meaning that it can easily change structure and shape depending on the chemical context. In [3] it is shown that it forms reversible conformational isomers in a bulk solution with changing pH. Previous experiments have studied this behavior in the context of adsorption on a silicon nitride surface with the DPI technique [4] by dissolving the BSA molecules in a PBS buffer and streaming this solution over the sensor. They have shown that the adsorption is reduced at pH 3 with respect to pH 5 [4]. As a proof-of-concept we repeat this experiment and record the (t,n) profile of the adsorption of BSA molecules to the silicon surface of the microring sensor, while changing the pH value of the buffer. This way, we show that the dual polarisation microring sensor is capable of recording conformational changes and we can benchmark our results to literature.

5.2.1 Capturing the TE and TM shifts

A 2mM phosphate buffer solution (PBS) was prepared with pH 5 and 3, to which BSA molecules were added until a concentration of 0.1 mg/ml was attained. Some



(a)

Figure 5.1: Resonance wavelength shift of the fundamental TE mode and fundamental TM mode of the BSA experiment in function of time.

PBS with pH 3 was left as running buffer. The laser was swept continuously from 1529 nm to 1543 nm, at a sweep rate of 2 nm/sec. The captured spectrum consisted of 4 fundamental TE modes and 3 fundamental TM modes. All the reagents were streamed over the chip at a rate of 30 $\mu\text{l}/\text{min}$. After streaming the calibration fluids as described in section 3.5, the experiment started by streaming PBS for 10 min. The flow was switched from running buffer to BSA in PBS at pH 3 for 10 minutes, followed by a 20 min incubation time. Then, we switched the flow to BSA in PBS at pH 5 for 10 minutes, after which an incubation time of 20 min followed. Eventually the flow was switched back to BSA in PBS at pH 3 for 10 minutes, followed by a 20 min incubation time, before the flow was switched to running buffer and eventually water. The captured resonance wavelengths of a TE and a TM mode are shown on Fig. 5.1.

5.2.2 Retrieving thickness, refractive index and bound mass

To calculate the thickness and refractive index based on the measured shifts, we perform the calibration protocol as outlined in section 3.5. After the SOI chip has been bound to the PDSM microfluidic cell and just before the experiment outlined above took place, water was flown over the chip surface and the FSR of both TE and TM modes were measured to obtain the width and the height of the cross section of the rectangular waveguide. The width is determined to be 491.7 nm, while the height is determined to be 210.7 nm. Next, we calibrated for the bulk fluid with unknown n_b , which is either PBS with pH 5 or PBS with pH 3. The wavelength shift of the TE mode when the bulk fluid was switched from water to

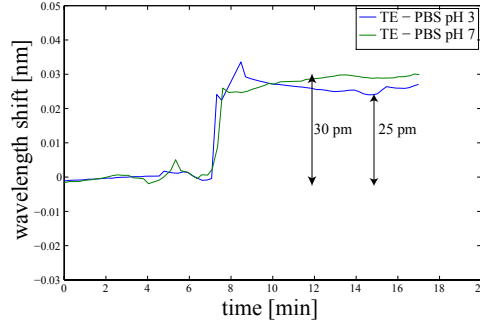


Figure 5.2: Shift of a TE mode in a microring resonator from water to PBS with pH 3 and pH 7. The graph shows that the acidity has a small influence on the resonance wavelength of the cavity.

PBS with pH 3 amounts to 25 pm. Fimmwave simulations show that a waveguide with the measured dimensions has a sensitivity to changes in bulk fluid from water of $\frac{\partial\lambda}{\partial\lambda_{buff}} = 57 \frac{nm}{RIU}$. We use the formula derived in [5] to calculate the refractive index of water as 1.3159 at 1532 nm, the average wavelength of the TE and TM mode. The value of n_b is then calculated using equation 3.21 and amounts to 1.3163. Since also PBS with a pH of 5 is used as buffer fluid in this experiment, we check what the influence is of the acidity on the refractive index of the bulk fluid. In Figure 5.2 we see that the difference between the TE shift from water to PBS with pH 3 and to PBS with pH 7 is less than 5 pm. A 5 pm shift corresponds to a change in buffer index of 0.08 mRIU, which has a negligible influence on the solving protocol to determine t and n of the BSA layer. Therefore we conclude that the acidity of the PBS buffer has negligible influence on the solved thickness and refractive index. The refractive index increment dn/dc of the BSA molecules in PBS is determined to be 0.186 per g/ml [6], such that the influence of the BSA molecules to the refractive index of the buffer fluid is negligible as well at the used concentration of 0.1 mg/ml .

With these three calibrated parameters (W , H , and n_b) the necessary simulations are performed and a thickness and refractive index profile is obtained, which is illustrated on Figure 5.3. Using equation 2.52 and the commonly used density of proteins of $\rho_{mol} = 1.35 \text{ g/cm}^3$ and a refractive index of 1.45, valid for a wide class of proteins, we obtain the adsorbed mass, plotted in Figure 5.4.

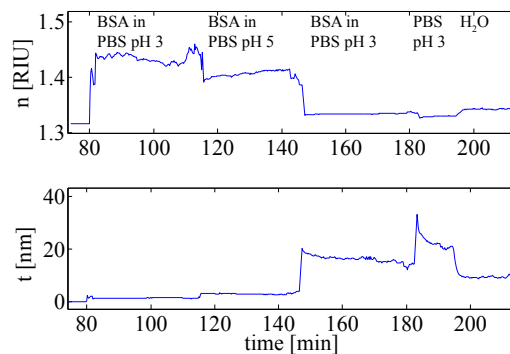


Figure 5.3: Thickness and refractive index profile of the layer consisting of adsorbed BSA molecules.

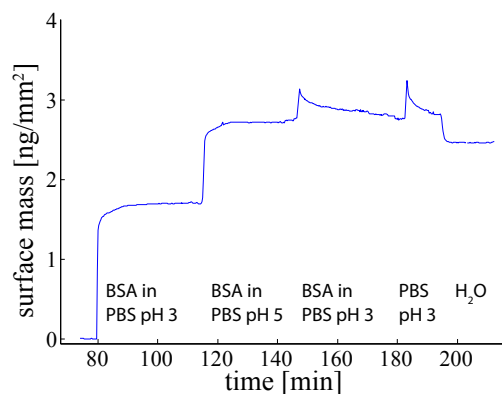


Figure 5.4: Adsorbed mass of BSA molecules to the silicon surface.

5.2.3 Structural response of the BSA molecules to the pH change

Of primal importance for the adsorption behavior and the geometry of the BSA molecules are the electrostatic conditions under which they conform. These electrostatics are influenced by the acidity of the bulk fluid by means of the isoelectric point of both BSA and silicon dioxide. The isoelectric point is the pH value of the buffer in which the BSA molecules are mixed, at which there is no net charge present on the molecules. And likewise for the silicon dioxide surface. Prior to the experiment the silicon has been oxidized by an oxygen plasma treatment and since for silicon dioxide this value equals 2-2.5 [7], the silica surface has a net negative charge for all pH values used in this experiment. The BSA molecule has an iso-

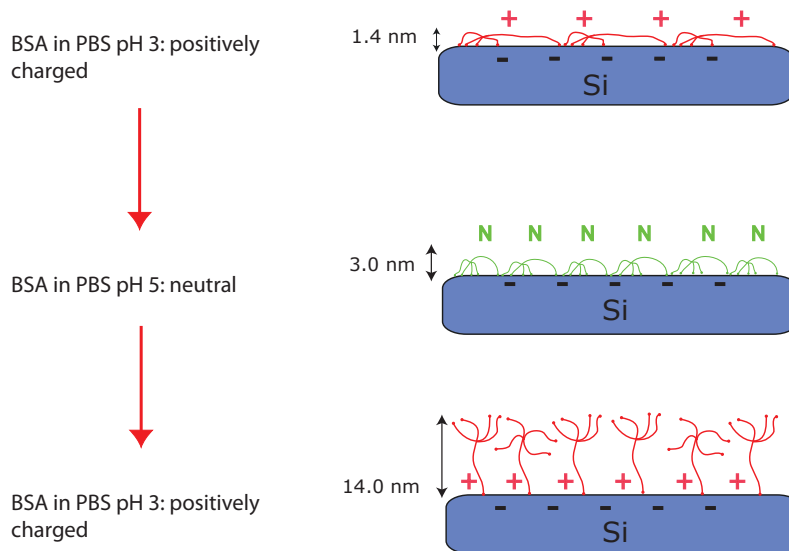


Figure 5.5: Evolution of the conformation of the BSA molecules as they adsorb to the silicon surface under influence of a change in pH value of the PBS buffer in which they are suspended.

electric point of 5, such that at pH 3, the BSA molecules have a positive charge, while at a pH 5, they are neutral. Furthermore, the oxygen plasma treatment of the silicon surface gives rise to an extremely hydrophilic surface [8]. In comparison, the silicon nitride surface of the DPI technique we compare our measurements to is more hydrophobic.

These considerations are reflected in both the adsorbed mass as in the thickness and the density profile. For a pH of 3, the BSA molecules are positively charged and the surface is negatively charged such that strong electrostatic interactions drive the adsorption. In this situation, the BSA molecules form a very dense and thin layer since it can connect to the surface via many points of positive charge. The mass of the BSA molecule is thus represented in a thin layer such that the surface which is covered by one molecule is high. This, and the fact that the BSA molecules are repelling each other gives rise to an intermediate amount of adsorbed mass. Switching the pH from 3 to 5 gives rise to an increase of the adsorbed mass. Since the BSA molecules are now in a neutral state, the mutual electrostatic repulsion between BSA molecules is relaxed such that the BSA molecules

on the surface can change their shape which allows more BSA molecules to adsorb. Furthermore, the electrostatic attraction between BSA and silicon dioxide is also reduced such that the layer becomes a bit thicker and sparser. Finally we see the non-reversible nature of the experiment when the pH value is switched back to pH 3: the adsorbed mass profile shows that there is no desorption of the proteins from the surface, while the (t,n) profile shows a complete reshaping of the BSA molecular layer. This observation was not made with the DPI technique on silicon nitride, which might be attributed to the difference in hydrophilicity between the two surfaces, since the authors of [9] describe the inability to wash off adsorbed BSA molecules on a hydrophilic surface, such as silicon dioxide. When the pH is switched from 5 to 3, the BSA molecules acquire a positive charge, such that they feel the electrostatic repulsion of neighbouring molecules again, yet they can not desorb easily. Furthermore, they can't return to the situation at the beginning of the experiment due to the increased steric hindrance, since more molecules are adsorbed at this stage than in the beginning. The layer of BSA molecules responds with a drop in refractive index to 1.335, accompanied by an increase in thickness to 19 nm, which relaxes to 14 nm, which is exactly the long side of the BSA molecules in bulk solution. This suggests that the BSA molecules turn upright due to the increased repulsion, such that they are dangling in the buffer, explaining the very thick and sparse layer. Since the BSA molecules have a pronounced denaturation during adsorption to hydrophilic surfaces, they can be longer than in a bulk solution. The experimental observation of the inability to wash off the BSA molecules on a plasma-treated silicon surface under various conditions is important in an immunoassay as it prevents the blocking step to degrade during the washing steps of the immunoassay itself. The various steps of the change in conformation as measured by the microring are illustrated in Figure 5.5

A comparison of the results made with DPI on silicon nitride [4] with the SOI microring as described here, is presented in Table 5.1. The values for pH 3 are referring to the first streaming of BSA in PBS at pH 3. For the thickness of the protein layer we see a difference smaller than 1 nm for pH 3 and about 2 nm for pH 5. For the refractive indices there is a difference of 0.02 RIU. The general trend of an increased adsorbed mass at pH 5 compared to pH 3 is confirmed, albeit with a higher adsorbed mass on silicon compared to silicon nitride. Although it is clear that the trends of the adsorption behavior are the same for both techniques, there are small differences in t , n and M of the adsorbed BSA layer as seen in Table 5.1. The difference in hydrophilicity of the silicon nitride and the plasma-treated silicon can explain these: Jeyechandran et al. have found that a difference in hydrophilicity has a great influence on the conformation of BSA molecules adsorbing to a surface [9]. Another observation that these authors make is that the adsorption of BSA saturates at only 50% surface coverage for hydrophobic surfaces, while

	t pH 3 [nm]	n pH 3 [RIU]	M pH 3 [ng/mm ²]	t pH 5 [nm]	n pH 5 [RIU]	M pH 5 [ng/mm ²]
Microring	1.4	1.433	1.70	3.0	1.407	2.72
DPI	0.8	1.445	0.48	4.8	1.425	2.11

Table 5.1: Comparison of the thickness, refractive index and adsorbed mass between the technique described in this paper (SOI Microring) and the silicon nitride dual polarisation interferometric (DPI) technique used in [4].

it can amount to 95% for hydrophilic surfaces. This is confirmed by the higher adsorbed mass with the SOI microring technique compared to the adsorbed mass with the silicon nitride DPI technique.

5.3 DNA experiment

Specific DNA/RNA detection assays can be used to determine e.g. the viral RNA of a specific infection in a medical diagnostics environment. The fast and correct pinpointing of an infection can lead to a reduced intake of unnecessary antibiotics, contrary to what is often the case today. In cancer therapy, an assay of several biomarkers on the nucleotide level can help the clinician assess whether or not a patient will be susceptible towards a certain treatment. This so-called personalized medicine is a recent trend which is expanding to other fields of diagnostics as well. A rapid and cheap detection instrument of specific nucleotides is hence a much-wanted medical and research tool. Many of these surface-based assays require the immobilization of a known single-stranded DNA marker, which can bind to its complementary strand in the test fluid. Due to the elongated and flexible nature of single-stranded DNA, it is crucial for the efficiency of the assay that this probe is oriented in the correct way and therefore easily accessible for binding. However, the in-situ analysis of the orientation of these probes is a notoriously difficult task. In this section we will present a DNA assay and show how the dual polarization microring can help in tackling exactly these conformational issues of the DNA probe.

This assay is first verified on an array of single polarization microring resonators, on which the impact of hybridization conditions, buffers, temperature and backfilling prior to hybridization is investigated. Immobilization of a capture DNA probe onto the SOI surface was done following the strategy developed by Byeon et al. using the commercially available reagents HyNic Silane and S-4FB [10, 11]. After the immobilization of a DNA capture probe to the surface, a complementary DNA sequence, the target, was hybridized and detected. To re-

duce the influence of non-specific adsorption to the silicon surface of the microring resonator, several blocking agents are reported in literature, such as bovine serum albumin (BSA) [9] or polymers [12]. The use of poly(ethylene glycol) (PEG) derivatives is widespread in non-fouling applications [13, 14]. For this reason, a short PEG chain, hexa(ethylene glycol) (HEG), was chosen in order to allow the polymer chains to adsorb to the surface in between the previously immobilized DNA probes. We have observed a positive influence of this HEG blocking on the subsequent hybridization. To study the orientation of these probes and the influence of the HEG layer we used a silicon chip which has the dual polarization functionality.

The development of the DNA assay was done in close collaboration with the polymer chemistry and biomaterials group of UGent. Primarily, the contributions of Anabelle van Eeghem, Sam Werquin, Arne Goes and Prof. Dubruel were instrumental in this development.

5.3.1 Hybridization protocol

DNA probe 1 which was used for the experiment was (5-CTCTCTCTCTCTCTCTCTCATGAGTCGTGAGTACGCTT-3) and DNA probe 2 was the same probe, but with a hexaethylene glycol spacer between the 5-end and the DNA sequence. Both were amino-modified at the 5-end. The complementary DNA (5'-CTCCTCAGTAATAGTGTCTTACAAGCGTACTCACGACTCATGAAATCGCCGGACTGCCGGTGGTTCGACAGGTCGGTGTATGCAG-3') was prepared by rolling circle amplification [15] by SciLifeLab.

- Silicon chips

The hybridization experiments are performed on SOI chips which have a matrix of 64 single polarization ring resonators. These are used to assess if the silane, DNA probe and complementary DNA probe bind successfully to the sensors and to research the influence of experimental parameters on the hybridization. The number of sensors with a valid signal differs from experiment to experiment. A chip with dual polarization functionality is used to examine the influence of the HEG adsorption on the orientation of the DNA probes.

The fabrication of the dual polarization chip is done by a planarization process. This is different from the single polarization chips used in these DNA experiments, as well as from the dual polarization chips used in the BSA experiments in section 5.2 and the polymer experiments in the next chapter.

Planarized waveguides only have their top surface accessible for the analytes. The sidewalls of the waveguide are covered with silicon dioxide. This causes the response of the TE mode to reduce in size. It does simplify the solving to thickness and density and from viewpoint of surface chemistry, a planar surface is advantageous as well.

The SOI surface of both chips was coated with a silicon nitride layer to ensure the reproducibility of the experiments. Indeed, previous studies have shown that in some cases, surface modifications such as silanization, can be more efficient on the area next to optical waveguides than on the waveguides itself [16]. This could be due to the use of different etchants during the production process of the silicon wafers. The silicon nitride layer excludes the influence of these etchants. It was characterized as an 8 nm thick layer with refractive index of 1.9348 at 1565 nm by ellipsometry.

- Silanization

The single polarization sensor chip was activated by plasma treatment with oxygen during 5 minutes. The dual polarization chip was activated for 0.4 minutes in air, to not create a significant oxide layer of unknown thickness and refractive index, as this troubles solving the shifts to thickness and density. Next, the surface was rinsed with ethanol (EtOH) to obtain a stable binding curve. A solution of 2 v/v % 3-N-((6-(N-Isopropylidene-hydrazino))nicotinamide)propyltriethoxysilane (HyNic Silane) in 95 % EtOH and 5 % Dimethylformamide (DMF), was flown over the ring resonators. After 20 minutes reaction, the surface was rinsed with EtOH again.

- DNA probe attachment

Prior to coupling, the DNA recognition probe was modified with sulfo-S-4FB via the amino group at the 5-end. This approach has been described in literature for the modification of antibodies [10] and single-stranded DNA [11] with an aldehyde. After modification, the DNA solution was stored at -20C before coupling to the silicon surface. After the silanization step, the surface was rinsed with PBS pH 6 containing 100 mM aniline. A 1 M solution of DNA probe 1 or DNA probe 2 was flown over the sensors during 40 minutes, followed by rinsing with the buffer.

- HEG adsorption

When the DNA probe was attached to the surface, a solution of HEG, with concentrations varying from 0.01 to 10 mg/ml in PBS pH 6, was flown over the sensors during 40 minutes.

- Hybridization

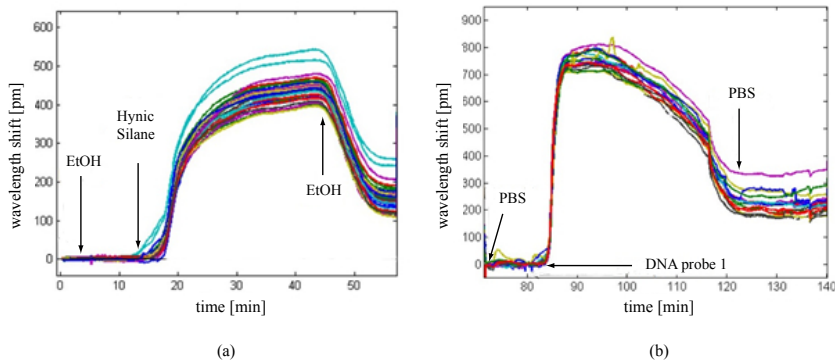


Figure 5.6: Wavelength shifts of a TE mode during the attachment of (a) hynic silane to the silicon surface and (b) during the attachment of DNA probe 1 to the hynic silane.

A 10 nM solution of complementary DNA in hybridization buffer was flown over the ring resonators. The hybridization buffer was composed of PBS pH 7.4 and 25 v/v % or 50 v/v % of formamide. Hybridization experiments were performed both at room temperature and at 35°C. The surface was rinsed with hybridization buffer after 40 minutes of hybridization.

5.3.2 Single polarization analysis

Optimizing the hybridization conditions

Figure 5.6(a) shows the shift of a TE mode due to the attachment of a hynic silane. The resulting net wavelength shift ranges from 100 to 300 pm, for the various sensors, indicating a successful silanization step. In Figure 5.6(b), the binding curve for DNA probe 1 is shown, with a net wavelength shift ranging from 200 to 400 pm. Both the hynic silane as the attachment of DNA probe 1 show a steady flat line after streaming, signifying a robust coverage of the surface with the respective biomolecule.

The hybridization protocol applied in these experiments is based on a procedure described by Qavi and Bailey [17], where a hybridization buffer containing 50 v/v % formamide in PBS pH 7.4 is used for detection of miRNAs. The concentration of formamide in the hybridization buffer was varied, both 25 v/v % and 50 v/v % were tested. To investigate the effect of hybridization close to physiological temperature, experiments were performed both at room temperature and at 35°C. At room temperature, no hybridization was observed when using both hybridization buffers (data not shown). When working at 35°C, hybridization was observed in some experiments with the hybridization buffer containing 25 v/v%

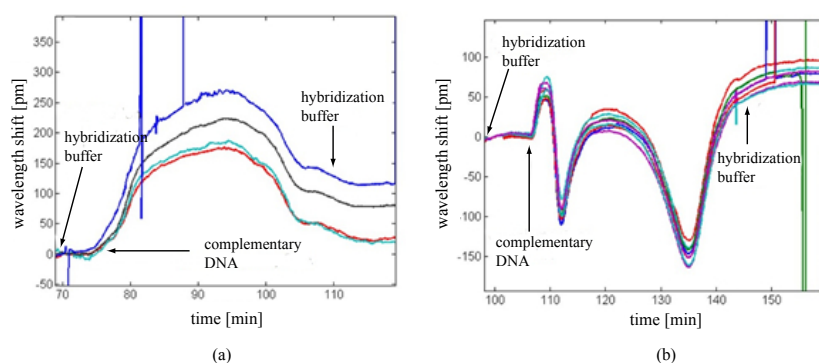


Figure 5.7: Binding curves of hybridization in a PBS buffer containing (a) 25 v/v% and (b) 50 v/v% of formamide at 35°C

formamide, although the results were not reproducible. Moreover, a negative drift of the wavelength was observed when washing the surface with buffer, indicating that the hybridization was either not successful or not permanent. A binding curve of a hybridization experiment at these conditions is shown in Figure 5.7(a). On the other hand, when using the hybridization buffer containing 50 v/v % formamide, reproducible results were obtained and an average resonance wavelength shift of 70 pm was obtained after hybridization, as can be seen in Figure 5.7(b). The presence of formamide in the hybridization buffer increases specificity, avoiding hybridization of sequences with single-base differences [17]. Moreover, it is well-known that formamide reduces the melting temperature of DNA in solution via the formation of H-bonds competing with the H-bonds between base pairs [18]. Although this would reduce the hybridization efficiency in a solution, it also reduces the formation of self-folded hairpin structures (secondary structures) of the single-stranded DNA-probes on the surface, as well as the interaction between different surface probes amongst each other [19]. Both effects increase the availability of the probes for hybridization. The obtained results show that the use of 50 v/v% of formamide in the hybridization buffer and a temperature close to physiological temperature (35°C) play a pivotal role in the hybridization process.

Adsorption of HEG polymer

In the previous section, the optimization of hybridization conditions was discussed. These conditions were applied to a new series of experiments, where a DNA probe with an immobilized HEG spacer (DNA probe 2) was introduced. In a next step, a HEG layer was adsorbed to the surface (i.e. backfilling [20]) with the purpose of

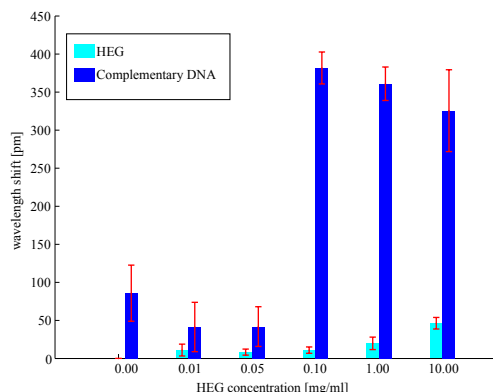


Figure 5.8: Shifts of the adsorption of HEG for different concentrations, together with the shifts of the subsequent complementary DNA-strand. Adsorption of HEG at sufficient concentration has a positive influence on the hybridization.

avoiding non-specific binding of the complementary DNA. The HEG spacer of the DNA probe makes sure that there is enough space in between the surface and the DNA probe for the HEG chains to adsorb to the surface. After adsorption of the HEG polymers, a solution of 10 nM complementary DNA was flown over the ring resonators. In Figure 5.8 the influence of the HEG polymers on the subsequent hybridization is shown in function of the HEG concentration. Both the shifts due to the HEG polymers as well as the shifts due to the complementary DNA strands are shown. For small HEG concentrations, the hybridization shift decreases compared to hybridization without a previous HEG step. This agrees with the expected non-fouling behavior of the HEG polymer: less complementary DNA molecules can find their way to the surface and adsorb, only those who bind to the DNA probe generate a response of the sensor. When higher concentrations of HEG were applied, a large increase of the wavelength shift after hybridization was observed, showing an secondary effect which promotes hybridization. For SPR applications, this behavior was observed as well and attributed to a more favourable orientation of the DNA probes on the surface [20, 21]. Without the addition of HEG polymers, it is reasonable to suppose that the covalently bound DNA probe will fold towards the silicon nitride surface and adsorb to it. This leads to an unfavorable orientation of the DNA probe and inefficient hybridization. This phenomenon has already been investigated on gold surfaces by Herne and Tarlov [22]. Since DNA can also adsorb to silicon surfaces [13, 23], a similar effect is likely to happen in this case. If the orientation of the DNA probes is improved, more single-stranded DNA will be available for hybridization with the complementary DNA, explaining the large increase in wavelength shift at higher HEG concentrations. Additionally, the shape

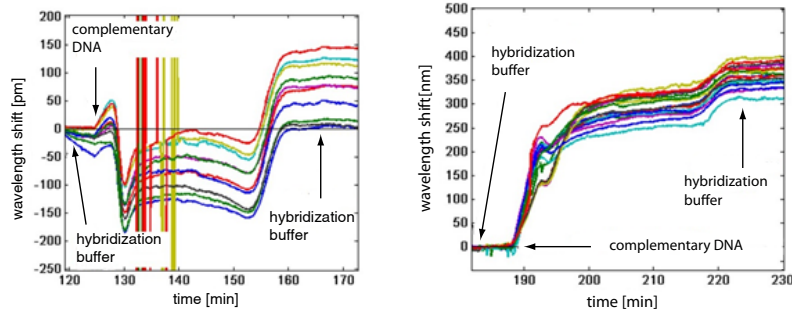


Figure 5.9: Binding curves of complementary DNA in 50 v/v % formamide in PBS pH 7.4 at 35°C (a) without the prior adsorption of HEG and (b) with a prior adsorption step of 1 mg/ml HEG

of the hybridization binding curves, presented in Figure 5.9, changes in comparison to the binding curve of hybridization without backfilling. The binding curve of the complementary DNA in the absence of a HEG backfilling step, shown in Figure 5.9 (a) is quite complex, possibly owing to continuous re-orientation of the DNA probes during the hybridization process. Due to the adsorption of the HEG polymers on the surface, this complex transient behavior is no longer present and the DNA probes seem to have adopted a stable conformation, which is reflected in the hybridization binding curve in Figure 5.9 (b).

5.3.3 Analysis with a dual polarization microring

The hypothesis that the HEG polymers re-orient the DNA strands can be verified with the dual polarization technique. On Figure 5.10 the resonant wavelength shifts of a TE and a TM mode, which are tracked simultaneously in a single ring, are shown. The sensorgram starts with a buffer switch from ethanol to PBS after the linking of the Hynic silane. Afterwards, a clear positive net shift is observable for the DNA probe, amounting to 87 pm for TE and 475 pm for TM mode. The net shift due to the HEG probe amounts to 13 pm for TE and 103 pm for TM mode. These positive shifts indicate that mass is deposited in both cases. Comparing these numbers to the measured shifts of the DNA probe and the HEG polymer of the TE polarization in the single polarization microring resonators mentioned in previous sections, we see that the shift of the TE mode is lower. As mentioned in section 5.3.1, this can be attributed to the planarization process. On the other hand, the shift of the TM mode is substantially higher, as expected.

These shifts can now be solved to a thickness and density profile, shown in Figure 5.11. The thickness and refractive indices of the complete stack after silaniza-

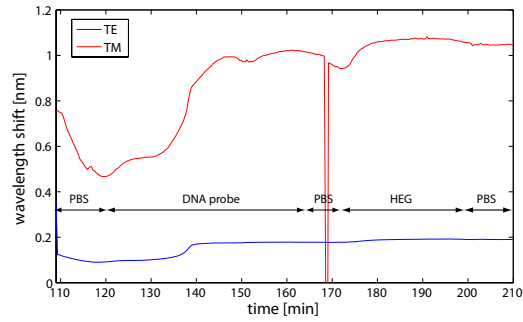
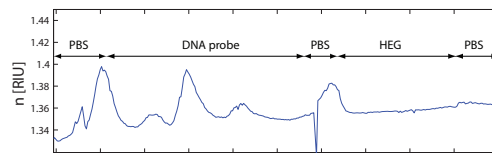
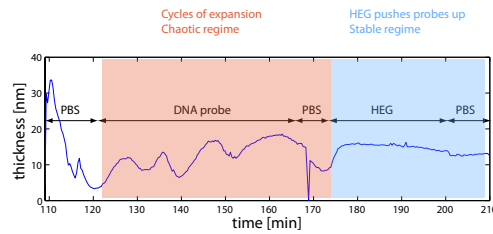


Figure 5.10: Shifts of a dual polarization measurement on a planarized SOI chip. Both the TE and the TM mode are plotted.



(a)



(b)

Figure 5.11: (a) Refractive index and (b) thickness profile during coupling of DNA probes to the surface and adsorption of 1 mg/ml HEG polymer

tion, attachment of the DNA probe and adsorption of HEG are given in table 5.2. The characteristics of the stack are measured during the streaming of PBS after a specific analyte is injected. Therefore, we need the refractive index of the PBS bulk fluid, which is measured to be 1.316 using the wavelength shift of the micro-ring resonator when switching from water to PBS. The mass fraction of the DNA probe in the stack can be obtained with equation 2.51. A value for the refractive index of DNA was reported as 1.465 at a wavelength of 632.8 nm. We assume

	t	n
Hynic Silane	3.57 nm	1.393
DNA probe	8.71 nm	1.380
HEG	12.96 nm	1.364

Table 5.2: Thickness and refractive indices of the complete stack after silanization, attachment of DNA probe and adsorption of HEG.

that the refractive index of the silane coupling has an equal refractive index, which is reasonable, but might introduce small numerical errors [24]. Correcting this term for dispersion [25], we obtain a value of 1.452. With a measured refractive index after attachment of the DNA probe of 1.380, we obtain a mass fraction of silane+probe of 47 %.

Looking at the thickness evolution, we observe an increase from 8.71 nm to 12.96 nm due to addition of the HEG polymer. Since DNA probe 2 has a HEG spacer attached to it as well, the size of the HEG polymer is smaller than the size of the stack after attaching the DNA probe. Since the HEG polymer is expected to adsorb to the surface [20], the increase of the thickness of the stack must be attributed to a reconfiguration of the DNA probe in a more upright position. At the same time we observe a decrease of the refractive index, which implies a decrease of the mass concentration in the stack as shown by equation 2.52. Although the addition of HEG should increase the mass in the stack, the unfolding of the DNA molecules is such that it overcompensates this and the mass concentration in this thicker stack decreases. A second observation is that the thickness of the stack is much more stable during the streaming of the HEG molecules than during the streaming of the DNA probe, implying that the HEG molecules indeed have a stabilizing function on the DNA probe layer. The hybridization protocol with HEG backfilling is illustrated in Figure 5.12

The thickness profile during the DNA-probe attachment shows the level of complexity that is associated with the attachment of DNA probes as several cycles of extension and densification are observed. Consulting literature for an indication of the thickness of a DNA probe layer results in a wide range in the reported thickness. A layer thinner than 1 nm is reported in [24, 26] for a 19-mer and a 26-mer strand, where it is concluded that the DNA molecules attach to the surface with its long axis parallel via multiple points. On the contrary, an almost fully extended probe layer of 16.6 nm for a 25-mer strand is reported in [27]. Therefore, we conclude that the 40-mer probe layer is in (partially) upright position, facilitating hybridization.

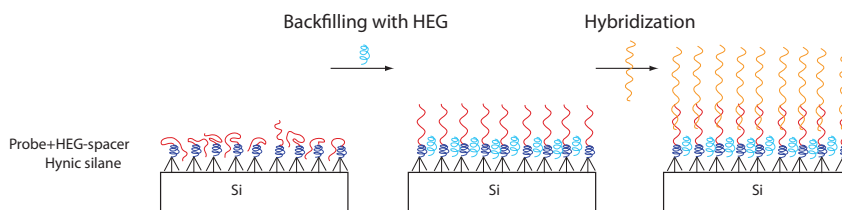


Figure 5.12: Illustration of the sequences of the DNA detection assay. The silicon surface is silanized with a Hynic silane which can bind to a modified DNA probe containing a HEG spacer. In a second step, a HEG polymer adsorbs to the surface and reorients the DNA probes. Finally, hybridization takes place by means of a complementary DNA strand.

5.4 Conclusion

We conclude that by using a dual polarization microring system we were able to calculate the thickness, the refractive index and the adsorbed mass of a thin BSA layer, bound to the SOI surface. The adsorption mechanisms of bovine serum albumin molecules on a silicon surface have been investigated and different conformational states of the BSA proteins have been observed, under influence of a changing pH value of the buffer solution. Since the BSA system is a well-known system, these observations show the validity of the sensor as a tool for conformational analysis. We have compared our results directly to the results obtained with a DPI technique on the same biological system, which correlated well.

In a second stage we have used this technique as a tool to improve the detection of single-stranded DNA. Many DNA recognition methods use the immobilization of a known DNA probe on the surface, as a receptor for its complementary strand. The orientation of these probes determines in an important way the possibility to hybridize. First, a DNA hybridization protocol using a hynic silane was established, showing that efficient hybridization occurs on the silicon microring surface by using a hybridization buffer containing 50 v/v % formamide at 35°C. In a second step the adsorption of HEG polymers after the attachment of the DNA probe was shown to increase the hybridization efficiency by 3 to 4 times of the following complementary probe. Switching to a dual polarization microring, we could repeat this backfilling experiment and it was shown that the DNA probe re-oriented in a more upright position while the stability of the layers was improved. This way we have shown the value of this technique as an in-situ tool to improve the efficiency of DNA detection techniques, which can be of great value to research in life science and pharmaceuticals. Furthermore, the prospect of a DNA detection

assay with built-in verification of the DNA probes, without the need for additional inspection tools is promising indeed.

References

- [1] T. Peters. *Serum Albumin*. Adv. Protein Chem., pages 161–245, 1985.
- [2] S.H. Brorson. *Bovine serum albumin (BSA) as a reagent against non-specific immunogold labeling on LR-White and epoxy resin*. Micron, pages 189–195, 1997.
- [3] D. C. Carter and J. X. Ho. *Structure of serum albumin*. Adv. Protein Chem., pages 153–203, 1994.
- [4] Neville J Freeman, Louise L Peel, Marcus J Swann, Graham H Cross, Andrew Reeves, Stuart Brand, and Jian R Lu. *Real time, high resolution studies of protein adsorption and structure at the solidliquid interface using dual polarization interferometry*. Journal of Physics: Condensed Matter, 16(26):S2493–S2496, July 2004.
- [5] P. Schiebener, J. Straub, J. M. H. Levelt Sengers, and J. S. Gallagher. *Refractive index of water and steam as function of wavelength, temperature and density*. Journal of Physical and Chemical Reference Data, 19(3):677–717, 1990.
- [6] J. a. De Feijter, J. Benjamins, and F. a. Veer. *Ellipsometry as a tool to study the adsorption behavior of synthetic and biopolymers at the air-water interface*. Biopolymers, 17(7):1759–1772, July 1978.
- [7] C. Krug and I. J. R. Baumvol. *Ultrathin Gate Dielectric Films for Si-Based Microelectronic Devices*. 2002.
- [8] Sara B Habib, Eleazar Gonzalez Ii, and Robert F Hicks. *Atmospheric oxygen plasma activation of silicon (100) surfaces*. Journal of Vacuum Science & Technology A, 28(100), 2013.
- [9] Y.L. Jeyachandran. *Efficiency of blocking of non-specific interaction of different proteins by BSA adsorbed on hydrophobic and hydrophilic surfaces*. Journal of Colloid and Interface Science, pages 136–142, 2010.
- [10] Ji-Yeon Byeon, F T Limpoco, and Ryan C Bailey. *Efficient bioconjugation of protein capture agents to biosensor surfaces using aniline-catalyzed hydrazone ligation*. Langmuir : the ACS journal of surfaces and colloids, 26(19):15430–15435, October 2010.
- [11] Abraham Qavi, Jared T Kindt, and Ryan C. Bailey. *Anti-DNA:RNA Antibodies and Silicon Photonic Microring Resonator Arrays Enable the Ultrasensitive, Multiplexed Detection of microRNAs*. 83(15):5949–5956, 2012.

- [12] S. Chen. *Surface hydration: Principles and applications toward low-fouling/nonfouling biomaterials*. Polymer, pages 5283–5293, 2010.
- [13] A. Cattani-Scholz. *PNA-PEG Modified Silicon Platforms as Functional Bio-Interfaces for Applications in DNA Microarrays and Biosensors*. Biomacromolecules, 10:489–496, 2009.
- [14] Arcot R Lokanathan, Shuai Zhang, Viduthalai R Regina, Martin a Cole, Ryosuke Ogaki, Mingdong Dong, Flemming Besenbacher, Rikke L Meyer, and Peter Kingshott. *Mixed poly (ethylene glycol) and oligo (ethylene glycol) layers on gold as nonfouling surfaces created by backfilling*. Biointerphases, 6(4):180–8, December 2011.
- [15] Fredrik Dahl, Johan Baner, Mats Gullberg, Maritha Mendel-hartvig, Ulf Landegren, and Mats Nilsson. *Circle-to-circle amplification for precise and sensitive DNA analysis*. Proceedings of the National Academy of Sciences of the United States of America, 101(13):4548–4553, 2004.
- [16] Bradley W Biggs, Heather K Hunt, and Andrea M Armani. *Selective patterning of Si-based biosensor surfaces using isotropic silicon etchants*. Journal of colloid and interface science, 369(1):477–81, March 2012.
- [17] Abraham J Qavi and Ryan C Bailey. *Multiplexed detection and label-free quantitation of microRNAs using arrays of silicon photonic microring resonators*. Angewandte Chemie (International ed. in English), 49(27):4608–11, June 2010.
- [18] R D Blake and Scott G Delcourt. *Thermodynamic effects of formamide on DNA stability*. Nucleic Acids research, 24(11):2095–2103, 1996.
- [19] Julia Fuchs, Daniela Dell’Atti, Arnaud Buhot, Roberto Calemczuk, Marco Mascini, and Thierry Livache. *Effects of formamide on the thermal stability of DNA duplexes on biochips*. Analytical biochemistry, 397(1):132–4, February 2010.
- [20] K P F Janssen, K Knez, L Vanysacker, J Schrooten, D Spasic, and J Lamertyn. *Enabling fiber optic serotyping of pathogenic bacteria through improved anti-fouling functional surfaces*. Nanotechnology, 23(23):235503, June 2012.
- [21] C. Boozer, S. Chen, and S. Jiang. *Controlling DNA Orientation on Mixed ssDNA/OEG SAMs*. Langmuir, 22:4694–4698, 2006.
- [22] T.M Herne and M.J. Tarlov. *Characterization of DNA Probes Immobilized on Gold Surfaces*. Journal of the American Chemical Society, pages 8916–8920, 1997.

- [23] V. Dugas, G Depret, Y. Chevalier, X. Nesme, and E. Souteyrand. *Immobilization of single-stranded DNA fragments to solid surfaces and their repeatable specific hybridization: covalent binding or adsorption?* Sensors and Actuators B, pages 112–121, 2004.
- [24] B. Lillis, M. Manning, H. Berney, E. Hurley, A. Mathewson, and M. M. Sheehan. *Dual polarisation interferometry characterisation of DNA immobilisation and hybridisation detection on a silanised support.* Biosens. Bioelectron., 21(8):1459–1467, February 2006.
- [25] Anna Samoc, Andrzej Miniewicz, Marek Samoc, and James G. Grote. *Refractive-index anisotropy and optical dispersion in films of deoxyribonucleic acid.* Journal of Applied Polymer Science, 105(1):236–245, July 2007.
- [26] José Luis López-Paz, Miguel Ángel González-Martínez, Jorge Escorihuela, María-José Bañuls, Rosa Puchades, and Ángel Maquieira. *Direct and label-free monitoring oligonucleotide immobilization, non-specific binding and DNA biorecognition.* Sensors and Actuators B: Chemical, 192:221–228, March 2014.
- [27] Kevin A Peterlinz, Rosina M Georgiadis, Tonya M Herne, and Michael J Tarlov. *Observation of Hybridization and Dehybridization of Thiol-Tethered DNA Using Two-Color Surface Plasmon Resonance Spectroscopy.* 7863(16):3401–3402, 1997.

=

6

Analysis of the interface layers of a bilayer system

6.1 Introduction

In the previous chapters, the microring surface analysis technique was used to study biological systems and their biochemical interactions, benefiting from the ability to directly measure physical quantities of layers which are smaller than 10 nm in a wet environment. *Directly* is key here, as many sensing systems require prior information on the specific system in the form of a calibration curve in order to determine concentration, thickness or other quantities. This is of little importance in detection schemes, where the interaction itself is known, but not to which extent or to which quantitative amount. In some domains of research such as surface chemistry, surface physics or biochemical physics, it is the interaction itself that is the subject of research, such as the conformations we have studied in the previous chapters. In this setting a calibration curve is pointless, just as assuming that only one physical quantity will change at a time, is hopeful at best. In order to study these kinds of dynamical systems with more than 1 independent unknown (multidimensional), the analyzing tool preferably has sufficient resolution to study the system in its native, natural state and sufficient functionality to be able to measure several physical quantities at once. Since biological agents typically have a size ranging from 1-6 nm, it is an application domain that naturally aligns with the microring sensor.

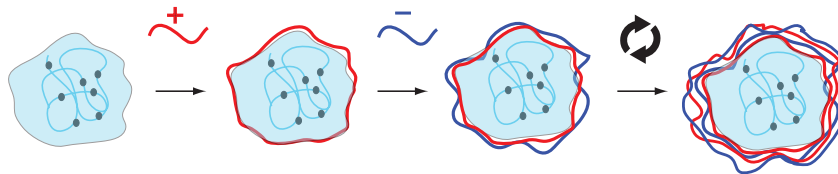


Figure 6.1: Schematic representation of the assembly with layer-by-layer technology of a microcapsule loaded with a drug component, by using a porous template. The drug is first inserted into a porous template, after which a bilayer polymer system is consequently wrapped around this template by the alternating coating with a positive polyelectrolyte and a negative polyelectrolyte.

There are however different fields of research where acquiring structural information for systems with a total size less than 10 nm thick is crucial. One of those is the analysis of heterogeneous material systems, with a heterogeneity which is above the resolution of the system. Ideally, the material is readily deposited from a solution which can be flown over the sensor surface as this provides a direct measurement of how the material builds up. While the bulk properties of these materials are often well-understood, the interaction with the surface they interact with or grow upon is difficult to research. Furthermore, the interaction with a surface or with other materials or molecules is often a decisive feature in the performance of this material. Heterogeneous engineerable systems that attracts a lot of research activity are polymeric multilayer thin films, especially in the domain of novel drug encapsulations to aid in the delivery of drugs to reach its intracellular target.

6.2 One layer after another

A recent review article [1] on the advances in polymeric multilayer capsules for drug delivery highlights the layer-by-layer (LbL) technology as a strong candidate for the fabrication of capsules. One promising way to load the drugs is to insert them in a porous template around which the layers are formed, as illustrated in Figure 6.1. This porous template can for example come in the form of a microgel [2]. The main assets of the LbL technology are an extreme control over capsule properties such as size and permeability while offering the possibility to modify the polymers with various molecular cross-linkers, which can provide a wide spectrum of biochemical functionalities [2, 3]. Furthermore, these LbL systems find applications in many other domains as well, including fiber sensors [4], separation membranes [5] and optical coatings [6].

A LbL system is formed by alternating the deposition of a polyanion and a polycation. An often used LbL system is the polyelectrolyte pair poly(allylamine) hydrochloride (PAH) and poly(sodium-4-styrene sulfonate) (PSS). To promote the adhesion of this system to a substrate, a poly(ethyleneimine) layer (PEI layer) is often used. The LbL systems were introduced in the early nineties and has been researched extensively ever since [7–14]. Despite the research attention this domain has experienced over the past two decades, the PAH/PSS bilayer system, and by extension all bilayer systems, are not yet completely understood. We have isolated two distinct domains where research results are rare due to technological reasons.

The first aspect of the bilayer domain of research that remains elusive is the nature of the properties of the first few bilayers close to the substrate. Ladam et al. subdivided the adsorption of the PAH/PSS system in a precursor zone, a core zone and an outer zone and have shown that the precursor zone consists of about 3 bilayers and shows different behaviour than the core zone, which is characterized by a linear increase in thickness [13]. The authors acknowledge that the analysis of this first zone is problematic due to two reasons. First, the change in signal of the reflectometric technique for the first adhesive PEI layer is not observable and very small for the subsequent first few bilayers. Second, by analyzing the thickness of thicker layers, they show that although the thickness increase in the linear bulk regime is reproducible, the total thickness is not. This shows that the first few layers themselves are not formed in a reproducible way and are highly dependent on initial conditions such as cleaning procedures. Many other studies have analyzed the PAH/PSS system with ellipsometry, but have reported similar difficulties to resolve the first few layers [7, 9, 11, 15, 16]. This limit on the operational range of ellipsometry has been circumvented [16] by measuring the refractive index of PSS and PAH layers on a thicker stack and using this value to determine the thickness of stacks thinner than 5 nm. In the light of the earlier mentioned zone model, it is clear that the properties of an individual layer in the bulk zone are different from those in the precursor zone, such that this assumption can very well introduce large errors on the measured thickness of the first few layers. Other techniques that have been used to study the PAH/PSS system, or LbL systems in general, include QCM-D [7], neutron reflectivity [8], AFM [10] or XPS [12]. These techniques often do not allow to measure in a wet environment (XPS, AFM, neutron reflectivity) however, or have a high SNR ratio for layers smaller than 10 nm (XPS).

A second domain which remains challenging is that of bilayers deposited from solutions with near-to-zero ionic strength. Several studies have shown that the thickness of the deposited layers decreases with decreasing ionic strength of the

solution [8, 13]. As a consequence, layers deposited from a solution with near-to-zero ionic strength are rare because of the same technological reason: it is challenging for standard techniques to measure the change in signal for layers this thin.

Since the research in the precursor zone and in bilayers deposited from near-to-zero ionic strength is rare by itself, research results in the overlap of these two domains are to our knowledge non-existent. The reason is that the size of the total stack is only a few nanometers big and hence not measurable in wet conditions. In this chapter we will pick up the challenge and verify whether this new sensing technique can go deeper than standard techniques.

6.3 Experimental section

6.3.1 Properties of the polymer solutions

Branched poly(ethyleneimine)(PEI, 25 kDa), poly(allylamine) hydrochloride (PAH; 58 kDa) and poly(sodium-4-styrene sulfonate) (PSS; 70 kDa) were purchased from Sigma-Aldrich. The density of PEI is 1.030 g/mL while the refractive index is also provided by the manufacturer as 1.5290 at 589.3 nm. This off-the-shelf, dry, bulk polymer refractive index is required to calculate the mass concentration of the deposited polymer in the thin layer during the measured experiment with equation 2.52. Using the dispersion of similar polymers [17], we calculate the refractive index to be 1.504 at 1550 nm. The refractive indices of PAH and PSS are not provided, but the refractive index of a polyelectrolyte stack consisting of alternating PAH and PSS layers is measured to be 1.550 with ellipsometry at 531 nm [12]. We assumed a similar dispersion as for PEI and thus a refractive index of 1.525 at a wavelength of 1550 nm is obtained for a multilayer stack of PAH and PSS layers. All polyelectrolytes were mixed with deionized water with a refractive index of 1.316 obtaining 2mg/ml solutions. The pH-value of these three solutions were measured as 8.5 for the PSS solution, 4.3 for the PAH solution and 10.3 for the PEI solution. With pKa-values of 3.5 for PSS, 8.5 for PAH, and 9.7 for PEI [14], this means that the PAH-molecules and the PSS-molecules are almost completely charged, while the PEI-molecules are weakly charged in the watery solution. The same batch of DI-water was also used as running fluid to obtain a steady baseline in between the different polyelectrolyte stages.

6.3.2 Outline of the experiment

To guide the discussion in the following sections some terminology needs to be defined. A *layer* signifies an isolated polymeric layer, either PEI, PSS or PAH. A *bilayer* is a combination of two layers: a PAH and a PSS layer. The *stack* is

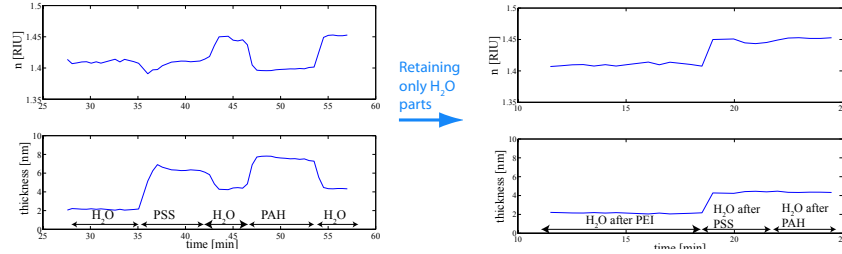


Figure 6.2: On the left one cycle of the polymer experiment is shown as calculated from the shifts of the TE and the TM modes. Since the calculation is only correct when there is a water cladding above the waveguide and polymer layer, only these parts are retained in the final figure on the right. All following figures will be shown in this final form.

the combination of all the layers that have been deposited on top of the microring resonator. The thickness and refractive index that is determined via the dual polarization technique is always that of the complete stack.

The experiment is carried out twice on a different photonic chip, on which a single microring sensor is read out per experiment. The specific sensor is nominally identical for both experiments, with a rectangular cross section of the waveguide with a height of 220 nm and a width of 520 nm. In reality the microrings do differ in the dimensions of the cross section of the waveguide due to wafer-scale variations in the lithographic fabrication process. The calibration protocol compensates for this however. These two experiments are referred to in the following as E1 and E2. A second difference between experiments E1 and E2 is the treatment of the surface. Both surfaces were activated with an oxygen plasma step as part of the bonding protocol with the PDMS microfluidic cell. However, the time between the experiment and the bonding was less than 1 hour for experiment E2 and about 1 day for E1. Habib et al. have shown that it takes about ten hours before the surface is reverted back to its original state [18]. The activation introduces silanol groups which are quite acidic. In an aqueous solution, they will deprotonate, giving rise to a negatively charged surface. Therefore it is likely that the surface of E1 is more negatively charged than the surface of E2.

In these experiments the t and n profile which the measured shifts are solved to, are only correct when the running fluid is water, because we do not know the refractive index increase of the water due to the addition of the polymers. Hence, we have reduced the data of the experiment to the sections where water is flowing over the sensors. This process is illustrated on Figure 6.2. Henceforth, whenever a thickness, refractive index, mass concentration, density, mass or similar quantity is given for a specific layer, this is at the stage of water streaming after the injection

in question.

The experiment is initiated by installing the SOI sensing chip with microfluidic channels in the measurement setup and flowing deionized water over the chip at a rate of $30 \mu\text{l}/\text{min}$. This flow is maintained over the chip until a steady baseline is reached. The waveguide dimensions of the ring are calibrated according to the protocol outlined in section 3.5 during these initial 10 minutes streaming of water. The waveguide of E1 is calculated to have a width of 469.7 nm and a height of 209.7 nm. For E2, the width equals 470.7 and the height equals 208.3 nm. Afterwards, the PEI solution is injected over the chip during 8 minutes, after which the flow is stopped and the solution is left to incubate for another 3 minutes, before switching back to water. After water was flowed over the chip for 4 minutes, the cycling of PSS and PAH was started. First PSS was flowed over the chip for 4 minutes, followed by an incubation time of 3 minutes. The flow was switched back to water which flowed over the chip for 4 minutes, followed by a 4 minute injection of PAH and an incubation time of 3 minutes. This cycle is repeated 5 times while recording the resonance wavelengths of both optical modes.

6.4 Results & Discussion

The resonance shifts of both TE and TM modes of both E1 and E2 are shown for the complete experiment in Figure 6.3(a) and Figure 6.3(b). These figures show that the shifts are very similar, only during the initial PEI stage the experiments seem to differ. This polymer layer is in direct contact with the sensor surface and thus is the most difficult to control, while also the most challenging to resolve adequately due to the small size of the total stack. A close-up of the PEI section of the experiment is shown in Figure 6.3(c) for E1 and in Figure 6.3(d) for E2. We see a similar trend in the evolution of the shifts for both experiments with a net shift of 345 pm for TE and 616 pm for TM in E1 and a net shift of 272 pm for TE and 483 pm for TM in E2. The deposited PEI layer is then determined to have a thickness equal to 1.84 nm for E1, with a refractive index of 1.465, while the thickness for E2 amounts to 1.08 nm, with a refractive index of 1.518. Using the refractive index and volume density of PEI as mentioned in section 6.3.1, we calculate the mass concentration of the polyelectrolytes within the layer and the adsorbed mass via equations 2.52 and 2.53: $0.816 \text{ g}/\text{cm}^3$ and $1.51 \text{ ng}/\text{mm}^2$ for E1 and $1.11 \text{ g}/\text{cm}^3$ and $1.19 \text{ ng}/\text{mm}^2$ for E2. All the characteristics of the adsorption of the PEI layer are displayed in Table 6.1.

We can't compare this measured thickness to the thickness of deposited PEI layers as measured by other in-situ tools such as reflectometry as these were not

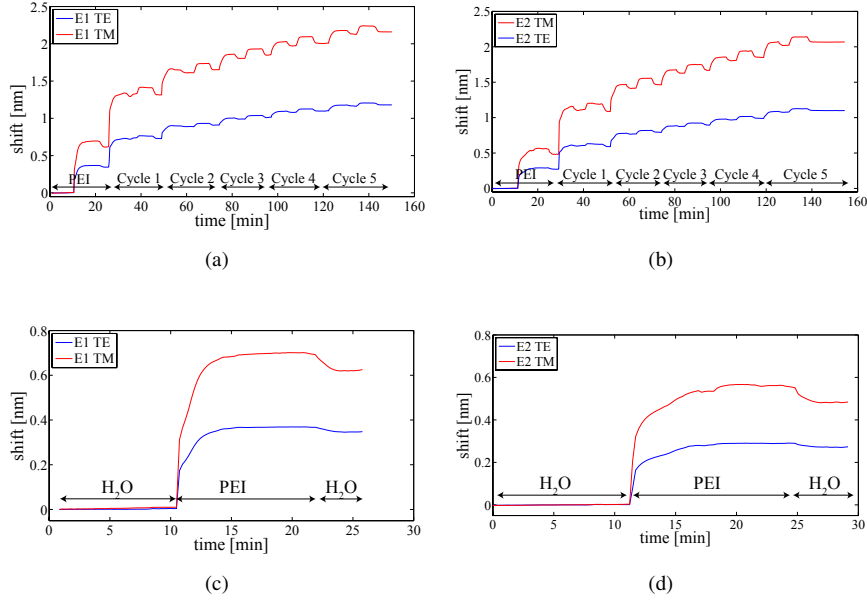


Figure 6.3: Recording of the wavelength shifts of a TE and TM mode during the whole bilayer experiment for (a) E1 and (b) E2: adsorption of a PEI layer, followed by 5 cycles of PSS/PAH bilayers. Zoom of the wavelength shifts during adsorption of the initial PEI layer for (c) E1 and (d) E2.

	$\Delta\lambda_{TE}$ [pm]	$\Delta\lambda_{TM}$ [pm]	t [nm]	n [RIU]	ρ_p [g/cm ³]	M [ng/mm ²]
E1	345	616	1.84	1.465	0.816	1.51
E2	272	483	1.08	1.518	1.11	1.19

Table 6.1: Comparison of the characteristics of the adsorbed PEI layers, as recorded by the dual polarization microring for different experiments E1 and E2.

able to detect a change in reflection for this first interface layer [13]. The standard ellipsometry also does not produce a signal which is larger than the experimental noise for a layer of only 2 nm thick [15]. This is in sheer contrast with the step size and the smoothness of the experimental curves in Figure 6.3 (c) and (d), where the signal is about 1000 times above the noise level, illustrating the resolving power of the microring technology. We can get an estimate of the thickness of a PEI layer by referring to the thickness as measured by XPS, but this technique is limited to dry samples. A PEI layer of 1.93 nm has been measured by XPS on a dry silicon sample [19]. This PEI layer was deposited from a buffered solution with a non-zero ionic strength, as opposed to the presented experiment where PEI is dissolved

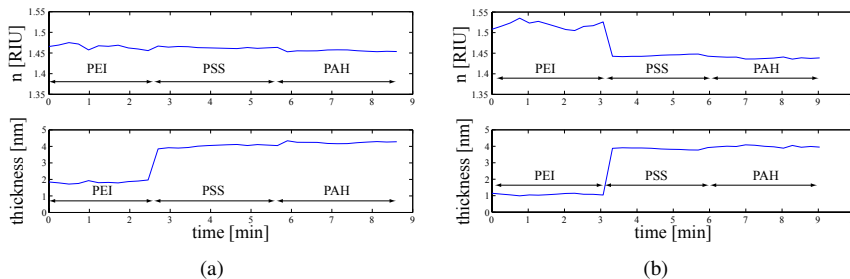


Figure 6.4: Refractive index and thickness profile during the first cycle of PSS/PAH for (a) E1 and (b) E2.

in deionized water. Although we expect the layer to swell as compared to a dry layer, the thickness of dry polyelectrolytes is reported to increase with increasing salt concentration of the solution from which it was deposited [20]. Since the PEI in this experiment is dissolved in deionized water, which exhibits a close-to-zero ionic strength [20], we can expect a minimum thickness.

Furthermore, we find that the branched polymers adsorbed in a very thin and very dense network for E2, more so than for E1 where the adsorbance gave rise to a thicker and less dense layer, accompanied by a higher adsorbed mass. The fact that the difference in shifts between the two experiments amounts to about 130 pm, while the noise is in the order of 0.2 pm, shows that the measured characteristics are well above noise levels and imply a clearly measured different layer and not an experimental deviation. Elsewhere, it has been stated that the precursor layers are not very reproducible in nature and are highly dependent on the condition and the charge of the surface they are adsorbing to [13]. In section 6.3.2, it was mentioned that it is likely that the surface of E2 is more negatively charged than the surface of E1, while the PEI molecules on the other hand are positively charged. It has been reported that when the polymers are dissolved in a solution with close-to-zero ionic strength, the charges are not efficiently shielded such that electrostatic attractions are the dominant force [9]. Consequently, if the surface of E2 is more negatively charged than E1, it should give rise to a higher electrostatic attraction, and by consequence a thinner and more dense layer, which is what we have measured. In the case of E1, the polymers form a layer which is less dense and thicker, such that each polymer chain occupies a smaller projected surface on the silicon and more polymers can adsorb, explaining the increase in adsorbed mass. Resolving the PEI layer shows that this technique can obtain a resolution lower than 1 Å for layers which are themselves only a few nanometers thick. To our knowledge, no tool has been able to do so in a wet environment and maintaining multiplexing capabilities.

	t_{PSS} [nm]	n_{PSS} [RIU]	t_{PAH} [nm]	n_{PAH} [RIU]
E1	4.02	1.463	4.24	1.455
E2	3.87	1.444	3.99	1.438

Table 6.2: Comparison of the characteristics of the total stack consisting of PEI/PAH or PEI/PAH/PSS (the terminating layer is indicated by the subscript), as recorded by the dual polarization microring for different experiments E1 and E2.

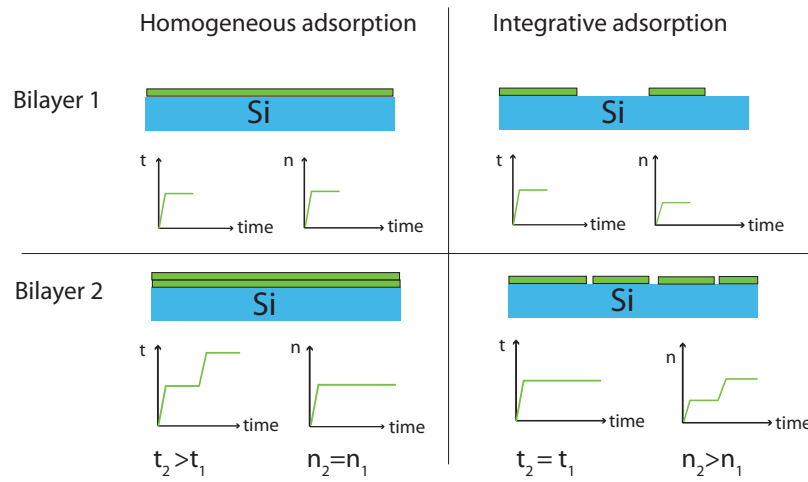


Figure 6.5: Illustration of homogeneous and integrative adsorption, two extreme cases of adsorption behavior, accompanied by their thickness and density profiles. Dual polarization sensing allows us to distinguish between these two. Bilayer 1 is characterized by t_1 and n_1 , while bilayer 2 is characterized by t_2 and n_2

After binding of an adhesive PEI layer, the first cycle of the polyelectrolyte bilayer system (PSS/PAH) is streamed over the chip. The resolved thickness and refractive index profiles are shown in Figure 6.4. The characteristics of the first cycle are given in Table 6.2. The difference in t and n between the stack of E1 and E2 decreased from 0.76 nm and 0.053 RIU for the stack consisting of just the PEI layer, to 0.25 nm and 0.018 for the PEI/PSS/PAH stack. It shows that the influence of the surface diminished and the PEI layer reconforms and increases in thickness due to the adsorption of the first bilayer.

As a last step, we study the behavior of the adsorption of this bilayer system as it evolves from an interface system to a stable bulk system. In general, two extreme cases of adsorption behavior can be distinguished when studying multilayer adsorption by means of thickness and density: homogeneous adsorption and inte-

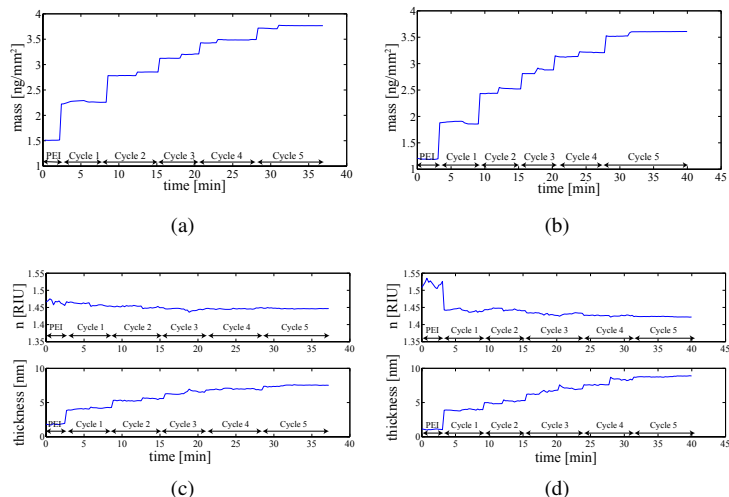


Figure 6.6: Total mass of the multilayer stack during cyclic adsorption of PSS-PAH for (a) E1 and (b) E2. Thickness and refractive index for respectively (c) E1 and (d) E2.

grative adsorption. These are illustrated in Figure 6.5 alongside their response in t and n . Homogeneous adsorption is characterized by a refractive index of the total stack that remains constant when a bilayer adsorbs, as opposed to the thickness which shows a stepwise increase as the layers adsorb on top of each other. Integrative adsorption is characterized by the opposite behavior: the thickness remains constant while the refractive index increases. This signifies that the molecules adsorb in a porous way, such that the next bilayer is integrated in the previous one, without increasing the thickness. The size of these pores can be small or rather large, as illustrated in Figure 6.5 where that the layers adsorb in isolated patches which are filled up in a next cycle.

The experimentally obtained refractive index and thickness evolution of the bilayer stack is plotted on Figure 6.6(c) and (d). A stepwise increase in thickness per cycle and a rather constant refractive index for both E1 and E2, show that the bilayers adsorb in homogeneous fashion: every layer is added on top of the stack, while the inner organization of the stack remains rather constant. This analysis portrays the added value of the dual polarization technique as opposed to the conventional technique with a single polarization, in an experimental way. A single polarization microring would only have access to the profile of one of the shifts in Figure 6.3 (a) or (b). This would merely imply that mass is added in a consistent way to the stack, but the structural details leading to insights in the adsorption mechanics would be obscured. The adsorbed mass is shown in Figure 6.6 (a) for

E1 and in Figure 6.6 (b) for E2, and is obtained by using equation 2.53 with the refractive index of a PAH/PSS bilayer as mentioned in the materials section. For the mass concentration, ρ_b is set equal to ρ_{PSS} in equation 2.52 which might introduce small numerical errors.

The mass increments and thickness increments per polyelectrolyte layer are shown on respectively Figure 6.7 (a) and (b) for both E1 and E2. The mass increments of Figure 6.7 (b) show a clear transition to a regime that settles in after 2 cycles. For the last 3 cycles the average deposited mass per bilayer (PAH and PSS combined) amounts to 0.31 ng/mm^2 with a standard deviation of 0.04 ng/mm^2 for E1 and 0.36 ng/mm^2 with a standard deviation of 0.04 ng/mm^2 for E2. It has been shown that a linear regime indeed is entered after 3-5 bilayers have been deposited [9, 13]. Comparing the amount of deposited mass to what was reported before, we find that for a 0 M NaCl solution a slightly higher mass of $0.5\text{-}1 \text{ ng/mm}^2$ is reported [13]. However, the solutions are prepared in a buffer (containing ions) with an adjusted pH of 7.4. It is stated elsewhere [9] that for a decreasing amount of ionic strength of the solution, the electrostatic forces gain in importance. Since we operate in water at near-zero ionic strength and the PSS and PAH molecules are fully charged at the measured pH we expect the molecules to be very stiff due to electrostatic repulsion [14], which can explain the slight decrease in adsorbed mass.

Also the thickness increase in the linear regime for E1, illustrated in Figure 6.7 (a) is slightly lower at 0.65 nm per bilayer and a standard deviation of 0.36 nm , as compared to the 0.8 nm per bilayer reported [8, 13]. We observe that the thickness increase in the first layer is much higher, compared to the increase accompanied with later cycles. This confirms previous results, where it is shown that the outer layer is more swollen than the inner layers [13]. The bilayers which are added starting from cycle 2 are as such expected to increase the thickness as a layer in the interior of the stack, and thus with reduced thickness compared to the first layer. Also, there is a clear trend that the thickness increase of the stack during the adsorption of a PSS layer is higher than during the adsorption of a PAH layer. This corresponds well with research results on thicker stacks in the bulk zone [8, 9, 11].

In this final section we have shown that the dual polarization microrring technique has adequate resolution to analyze bilayer systems of only a few layers thick when deposited from deionized water. This has proven to be almost impossible for other techniques due to the stringent requirements on resolution of the system since the bilayers under these conditions are usually thinner than 1 nm .

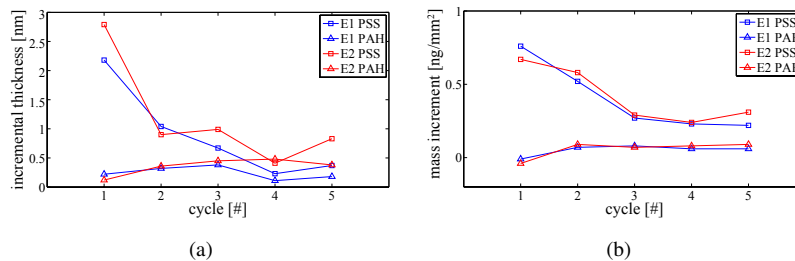


Figure 6.7: (a) Incremental mass per cycle referenced to the total mass of the stack on which the layer in question adsorbs. (b) Incremental thickness per cycle referenced to the total thickness of the stack on which the layer in question adsorbs.

6.5 Conclusion

In this chapter we have evaluated the use of the dual polarization technique to study multilayer polyelectrolyte systems, which are used to create drug vessels for the controlled release of their content. More specifically, the adsorption behavior of the interface layers of a polyelectrolyte bilayer system when deposited from deionized water was studied. It was shown in literature that analyzing a bilayer system under these conditions, which generate a sub-10 nm interface stack consisting of layers which are themselves only 1 nm thick, has been almost impossible to analyze with ellipsometry, reflectometry or other standard techniques. By using a dual polarization technique however, the thickness, refractive index and deposited mass of the first 5 bilayers of a PAH/PSS system could be measured

The experiment was performed twice. After the adsorption of an initial PEI layer which was influenced by the different treatment of the silicon surface, a three-layer stack consisting of PEI/PSS/PAH produced similar characteristics for both experiments. The first PEI layer has also been resolved adequately: in E2 the thickness has been measured to be as low as 1.08 nm with clear resonance shifts which are about 1000 higher in size than the noise level. It shows the great sensitivity to changes close to the surface and low transduction noise of the microring technique. Furthermore, the results show that by analyzing the thickness as well as the refractive index of the bilayer system during the full 5 cycles, we can determine that the adsorption occurred in a homogeneous way. For both experiments, a regime is reached after 2 cycles in terms of adsorbed mass.

References

- [1] Stefaan De Koker, Richard Hoogenboom, and Bruno G De Geest. *Polymeric multilayer capsules for drug delivery*. Chem Soc Rev, 41(7):2867–2884, April 2012.
- [2] Bruno G De Geest, Wim Van Camp, Filip E Du Prez, Stefaan C De Smedt, Jo Demeester, and Wim E Hennink. *Biodegradable microcapsules designed via 'click' chemistry*. Chem. Commun. (Cambridge, U. K.), (2):190–2, January 2008.
- [3] Francesca Cavaliere, Sher Leen Ng, Claudia Mazzuca, Zhongfan Jia, Volga Bulmus, Thomas P Davis, and Frank Caruso. *Thin multilayer films and microcapsules containing DNA quadruplex motifs*. Small, 7(1):101–111, January 2011.
- [4] Nahid Raoufi, Frederic Surre, Muttukrishnan Rajarajan, Tong Sun, and Kenneth T V Grattan. *Fiber Optic pH Sensor Using Optimized Layer-by-Layer Coating Approach*. IEEE Sens J, 14(1):47–54, 2014.
- [5] Nithya Joseph, Pejman Ahmadiannamini, and Ivo F J Vankelecom. *Polymer Chemistry Layer-by-layer preparation of polyelectrolyte multilayer membranes for separation*. Polym. Chem, 5:1817–1831, 2014.
- [6] Kiyofumi Katagiri, Shin-ichiro Yamazaki, Kei Inumaru, and Kunihiro Koumoto. *Anti-reflective coatings prepared via layer-by-layer assembly of mesoporous silica nanoparticles and polyelectrolytes*. Polym J, 47(2):190–194, November 2014.
- [7] Jagoba J. Iturri Ramos, Stefan Stahl, Ralf P. Richter, and Sergio E. Moya. *Water Content and Buildup of Poly(diallyldimethylammonium chloride)/Poly(sodium 4-styrenesulfonate) and Poly(allylamine hydrochloride)/Poly(sodium 4-styrenesulfonate) Polyelectrolyte Multilayers Studied by an in Situ Combination of a Quartz Crystal Microb.* Macromolecules, 43(21):9063–9070, November 2010.
- [8] Mathias Losche, Johannes Schmitt, Gero Decher, Wim G Bouwman, and Kristian Kjaer. *Detailed Structure of Molecularly Thin Polyelectrolyte Multilayer Films on Solid Substrates as Revealed by Neutron Reflectometry*. Macromolecules, 31:8893–8906, 1998.
- [9] Peter Nestler, Stephan Block, and Christiane A Helm. *Temperature-Induced Transition from Odd-Even to Even-Odd Effect in Polyelectrolyte Multilayers Due to Interpolyelectrolyte Interactions*. J Phys Chem A, 116:1234–1243, 2012.

- [10] J. Dejeu, L. Buisson, M.C. Guth, C. Roidor, F. Membrey, D. Charrat, and A. Foissy. *Early steps of the film growth mechanism in self-assembled multilayers of PAH and PSS on silica*. *Colloids Surf A*, 288(1-3):26–35, October 2006.
- [11] John E Wong, Florian Rehfeldt, Peter Ha, Motomu Tanaka, and Regine Klitzing. *Swelling Behavior of Polyelectrolyte Multilayers in Saturated Water Vapor*. *Macromolecules*, 32:7285–7289, 2004.
- [12] Marta Kolasinska, Rumen Krastev, and Piotr Warszynski. *Characteristics of polyelectrolyte multilayers: effect of PEI anchoring layer and posttreatment after deposition*. *J. Colloid Interface Sci.*, 305(1):46–56, January 2007.
- [13] G Ladam, P Schaad, J C Voegel, P Schaaf, G Decher, and F Cuisinier. *In Situ Determination of the Structural Properties of Initially Deposited Polyelectrolyte Multilayers*. *Langmuir*, 31(6):1249–1255, 2000.
- [14] Wing Cheung Mak, Kwan Yee Cheung, and Dieter Trau. *Influence of Different Polyelectrolytes on Layer-by-Layer Microcapsule Properties: Encapsulation Efficiency and Colloidal and Temperature Stability*. *Chem. Mater.*, 20(17):5475–5484, September 2008.
- [15] R Reiter, H Motschmann, H Orendi, A Nemetz, and W Knoll. *Ellipsometric Microscopy . Imaging Monomolecular Surfactant Layers at the Air-Water Interface*. *Langmuir*, (8):1784–1788, 1992.
- [16] J Ruths, F Essler, G Decher, and H Riegler. *Polyelectrolytes I : Polyanion / Polycation Multilayers at the Air / Monolayer / Water Interface as Elements for Quantitative Polymer Adsorption Studies and Preparation of Hetero-superlattices on Solid Surfaces .* *Langmuir*, 37(4):8871–8878, 2000.
- [17] N Sultanova, S Kasarova, and I Nikolov. *Dispersion Properties of Optical Polymers*. *Acta Phys. Pol., A*, 116(4):585–587, 2009.
- [18] Sara B Habib, Eleazar Gonzalez Ii, and Robert F Hicks. *Atmospheric oxygen plasma activation of silicon (100) surfaces*. *Journal of Vacuum Science & Technology A*, 28(100), 2013.
- [19] Eva Melnik, Paul Muellner, Ole Bethge, Emmerich Bertagnolli, Rainer Hainberger, and Michael Laemmerhofer. *Streptavidin binding as a model to characterize thiol-ene chemistry-based polyamine surfaces for reversible photonic protein biosensing*. *Chem. Commun. (Cambridge, U. K.)*, 50(19):2424–2427, March 2014.

- [20] Richard A Mcaloney, Mark Sinyor, Vyacheslav Dudnik, and M Cynthia Goh. *Atomic Force Microscopy Studies of Salt Effects on Polyelectrolyte Multilayer Film Morphology*. *Langmuir*, (21):6655–6663, 2001.

7

Conclusion

The dual polarization microring resonator has a set of characteristics which makes it an excellent and unique candidate to analyze the conformations of molecular-size systems in the field of life science and drug development. Molecular binding events can be analyzed in their native wet environment with a resolution on thickness smaller than 0.1 nm and on refractive index of 1 mRIU. Furthermore, layers with a reasonable mass concentration leading to a refractive index of 1.416 can be analyzed down to a thickness of 0.75 nm. Considering that the size of an average protein is a few nanometers, this sensing system is well-adjusted to research the biophysics of a binding event between a protein and small drug ligand. This maneuvers this technology exactly in the gap which was defined by the FDA critical initiative as one of the main shortcomings of the current critical state of pharma. Since the SOI platform can be easily integrated with microfluidics, the total sensing device can be considered a consumable, which further lowers the threshold for uptake in drug development programs. The size of the microring paves the way for a highly multiplexed device, ensuring a high throughput. Using standard chemical functionalization protocols, a wide selection of proteins or nucleotides can be attached to the surface. These characteristics are not combined in any other sensing tool to our knowledge.

To highlight the various domains of applications of this novel sensor we have applied it to three different aspects of research in life science: conformational analysis of proteins, DNA detection assays and fabrication of drug capsules via multilayer polyelectrolyte systems.

By studying the conformations of BSA proteins first, we could verify the system, as the behavior and dimensions of BSA molecules are fairly well-known. The conformational changes due to a change in pH-value of a buffer were observed and related to literature. In a second step, we applied this tool to the optimization of a DNA detection assay. This work was done in close collaboration with the polymer chemistry and biomaterials group of UGent and especially the work of Anabelle van Eeghem, Sam Werquin, Arne Goes and Prof. Dubruel was crucial in this development. With their help, the hybridization of single-stranded DNA was achieved on the microring surface. However, these DNA assays have proven to be very sensitive to the orientation of the DNA probes. Almost no hybridization is possible when the probes are e.g. oriented flat on the substrate. These orientations can usually only be qualified in an indirect way: through the binding with a complementary strand. By using a dual polarization microring we could clearly observe the orientation of these DNA strands and the influence of backfilling with a small HEG polymer proved to push the DNA probes in a more upright position. This increased the hybridization efficiency by a factor of 3-4. Long-running experience in our research group showed that we understand and control the physics of the optical transducers that make up these detection assays quite well. The domain of chemical functionalization however, which is extremely decisive on the quality of these assays, has proven to be another story. We often lack the techniques to study these biochemical functionalization protocols. To be able to analyze these directly on top of the ring itself, and not via e.g. fluorescence on a blank substrate, is a unique feature and proves to be very powerful to better understand and improve these assays.

In a third series of experiments we have applied the sensor to polyelectrolyte bilayer systems which are used as a novel material for drug vessels. These experiments show that we can very clearly detect even the first adhesive PEI layer on top of the chip surface, which is only 1 nm in size. We offered an experimental verification of the resolving power of the system, obtained in chapter 3. The context of this experiment was challenging for the dual polarization ring resonator: the interface layers of a bilayer polyelectrolyte system which deposit from deionized water are known to produce stacks with minimum thickness. A literature study shows that no technique has been able to generate signals that are above the noise of the system for these first few layers. By quantifying these layers with a microring resonator, we show the resolving power of the presented technique. By conclusion, the dual polarization technique will be very useful in the study of thin layer adsorption mechanics.

7.1 Perspectives

The theoretical work of chapter 3 has shown that this technique is at its limits. Changing the waveguide design, or using different modes to interrogate the layer instead of the TE and the TM mode will to our knowledge only give marginal improvements. The resolutions we obtained are on the one hand decided by the light-matter interaction at a waveguide and the differential behavior towards thickness and refractive index. These relations are very elemental, which is shown in the tight coupling of these in waveguide equations. Major advances here seem unlikely. On the other hand however, reducing the noise via system improvements *can* be made. It was hinted at that a big improvement in temporal resolution can improve the detection limit by a large factor. However a more detailed noise analysis and more importantly, bio-experiments should be conducted in order to explore these limits.

In this thesis, the functionalities of a single mode resonator and those of a dual mode resonator have been approached in a separate, discriminating manner. It is however evident that whatever a single mode microring resonator can offer in terms of affinity analysis and determination of concentration, can also be achieved by a microring resonator which is excited with two polarizations. Combining both would offer a very powerful analysis tool for many biological assays. For instance, single microring resonators applied in a real clinical detection environment can be crippled by non-specific binding. The omnipresence of molecular entities in any human body matrix, such as serum, urine, or sputum, besides the one which needs to be detected, poses problems. It might require a long development of the platform to prevent these false positives via highly advanced surface chemistry and high affinity receptor molecules. That this is achievable, can be seen in the recent developments of Genalyte, working towards a point-of-care tool based on single polarization microring resonators. However, besides the fact that a dual polarization microring will most probably allow for a faster optimization of the surface chemistry due to the inherent in-situ analysis of these probes, as shown from the DNA assay in chapter 5, the non-specific binding in a clinical context can be tackled as well. Replacing the single mode resonators with dual polarization resonators immediately offers an analytical toolkit to verify whether or not the bound antigen is the one which is sought after. A false positive can e.g. be filtered out by relying on the specific thickness this antigen should inherently have. Unfortunately, the current state of the dual polarization system would not allow such a fast determination, as opposed to the generated binding curve based solely on the resonant wavelength shifts (as is used in a single polarization microring). As of now, the determination of t and n is quite a labor-intensive matter, mainly due to the long simulations that need to be done before the signals can be solved to a viable thick-

ness and density profile, but also due to the non-trivial extraction of TE and TM modes from a compound spectrum. Furthermore, the low yield of microrings exhibiting dual polarization functionality is also troublesome. These issues are far from unsurmountable however, but require a degree of product optimization which was beyond the scope and goal of this thesis. It can be arguably stated that the current state of the microring detection platform is a mature one, and that many further improvements towards any clinical or real-life detection product lie in the realm of product development and out of the scope of research.